Title
Differential-Geometric-Control Formulation of Unconventional Flight Dynamics

Author
Hassan, Ahmed

Publication Date
2018

UNIVERSITY OF CALIFORNIA,
IRVINE

Differential-Geometric-Control Formulation of Unconventional Flight Dynamics

DISSERTATION

submitted in partial satisfaction of the requirements
for the degree of

DOCTOR OF PHILOSOPHY

in Mechanical and Aerospace Engineering

by

Ahmed Mamdouh Hassan

Dissertation Committee:
Professor Haithem E. Taha, Chair
Professor Kenneth D. Mease
Professor Anton Gorodetski

2018

DEDICATION

وَيَسْأَلُونَكَ عَنِ الرُّوحِ ۖ قُلِ الرُّوحُ مِنْ أَمْرِ رَبِّي وَمَا أُوتِيتُم مِّنَ الْعِلْمِ إِلَّا قَلِيلًا ﴿٨٥﴾

القرآن الكريم (سورة الإسراء، آية ٨٥)

And they will ask thee about [the nature of] divine inspiration. Say: “This inspiration [comes] at my Sustainer’s behest; and [you cannot understand its nature, O men, since] you have been granted very little of [real] knowledge.”

The Holy Qur’an (surah Al-Israa, verse 85)

TABLE OF CONTENTS

LIST OF FIGURES

LIST OF TABLES

Page

ACKNOWLEDGMENTS

I would like to deeply thank my advisor, Professor Haithem Taha, for his utmost patience, support, and encouragement throughout my PhD journey. He has always been a source of inspiration to me. I am indebted to him for forging my research and analytical thinking skills. I would also like to thank Professor Kenneth D. Mease and Professor Anton Gorodetski for accepting to be in my defense committee. I greatly appreciate their time and feedback.

I am very grateful to my wife, Ala'a, whom I met midway through my PhD. Thank you for your unconditional love, support, and sacrifice. Without you, this work would not have been possible. I am also very grateful to my parents: Mamdouh and Amal. Thank you for believing in me and for your tremendous support, care, and patience over the years. No words can express my gratitude to you. My brother, Mohamed and my sister, Sara. Thank you for your help, support, and encouragement over the years. I would also like to thank my extended family here in the US and overseas for their support and encouragement. Certainly, I would not have survived this journey without all of them.

I would like to thank my colleagues and lab-mates at UCI for the fruitful discussions and good times, especially Amir Rezaei, Sameh Eisa, Marco Maggia, and Matthieu Robart. Also, I would like to thank all my friends in Irvine and the members of the Egyptian community in Orange County for the good times we had together over those years. Finally, I would like to thank my friends in the US and overseas for their support, encouragement, and good times, especially: Ahmed Elsadek, Ahmed Ismail, Mohamed Abdelghani, Ahmed Khattab, Mostafa Moharam, Elsayed Ezzat, Kamel Elsayed, Mahmoud Hisham, Mohamed Mohie-Eldeen, and many others.

Finally, I would like to acknowledge the support of the National Science Foundation grant CMMI-1709746.

CURRICULUM VITAE

Ahmed Mamdouh Hassan

EDUCATION

Doctor of Philosophy in Mechanical and Aerospace Engineering **2018**
University of California, Irvine *Irvine, CA*

Master of Science in Mechanical and Aerospace Engineering **2015**
University of California, Irvine *Irvine, CA*

Bachelor of Science in Aerospace Engineering **2011**
Cairo University *Cairo, Egypt*

RESEARCH EXPERIENCE

Graduate Research Assistant **2015–2018**

Aeronautics, Dynamics, and Control Laboratory
University of California, Irvine *Irvine, CA*

TEACHING EXPERIENCE

Teaching Assistant **2016–2018**

Dynamics and Control of Aerospace Vehicles (MAE 175)
University of California, Irvine *Irvine, CA*

REFEREED JOURNAL PUBLICATIONS

- Hassan, A. M., Taha, H. E. (2018). Differential-Geometric-Control Formulation of Flapping Flight Multi-Body Dynamics. *Journal of Nonlinear Science*, Dec 2018.

- Hassan, A. M., Taha, H. E. (2017). Combined AveragingShooting Approach for the Analysis of Flapping Flight Dynamics. *Journal of Guidance, Control, and Dynamics*, 41(2), 542-549.

- Hassan, A. M., Taha, H. E. (2017). Geometric control formulation and nonlinear controllability of airplane flight dynamics. *Nonlinear Dynamics*, 88(4), 2651-2669.

- Hassan, A. M., Taha, H. E. (2016). Airplane loss of control problem: Linear controllability analysis. *Aerospace Science and Technology*, 55, 264-271.

REFEREED CONFERENCE PUBLICATIONS

- Hassan, A. M., Taha, H. E. (2017). A combined Averaging-Shooting Approach for the Trim Analysis of Hovering Insects/Flapping-Wing Micro-Air-Vehicles. In *AIAA Guidance, Navigation, and Control Conference* (p. 1734).

- Hassan, A. M., Taha, H. E. (2017). Aerodynamic-Dynamic Interactions and Multi-Body Formulation of Flapping Wing Dynamics: Part I Modeling. In *AIAA Guidance, Navigation, and Control Conference* (p. 1274).

- Hassan, A. M., Taha, H. E. (2017). Aerodynamic-Dynamic Interactions and Multi-Body Formulation of Flapping Wing Dynamics: Part II Trim and Stability Analysis. In *AIAA Guidance, Navigation, and Control Conference* (p. 1275).

- Hassan, A. M., Taha, H. E. (2016, December). Higher-order averaging analysis of the nonlinear time-periodic dynamics of hovering insects/flapping-wing micro-air-vehicles. In Decision and Control (CDC), 2016 IEEE 55th Conference on (pp. 7477-7482). IEEE.

- Hassan, A. M., Taha, H. E. (2016). Geometric nonlinear controllability analysis for airplane flight dynamics. In AIAA Guidance, Navigation, and Control Conference (p. 0079).

HONORS AND AWARDS

- Holmes Fellowship at UC Irvine for the academic year 2017/2018.

- Finalist in the 2017 AIAA Guidance, Navigation, and Control Conference student paper competition with a paper titled A Combined Averaging-Shooting Approach for the Trim Analysis of Hovering Insects/Flapping-Wing Micro-Air-Vehicles.

- Best Presentation in Session award, the 2017 AIAA Guidance, Navigation, and Control Conference.

- UCI Associated Graduate Students travel grant, 2016.

ABSTRACT OF THE DISSERTATION

Differential-Geometric-Control Formulation of Unconventional Flight Dynamics

By

Ahmed Mamdouh Hassan

Doctor of Philosophy in Mechanical and Aerospace Engineering

University of California, Irvine, 2018

Professor Haithem E. Taha, Chair

Differential-geometric control theory exploits *differential geometry* in the analysis of dynamical control systems. Differential geometry is a mathematical discipline that is concerned with studying calculus on curved (non-Euclidean) spaces. The main focus of this Dissertation is to formulate modern aeronautical engineering applications in a differential-geometric control framework.

Nonlinear controllability analysis is one of the most important aspects of differential-geometric control theory. Its importance emanates from the fact that linear controllability conditions for linearized systems are not necessary. That is, there exists a class of nonlinear systems that are linearly uncontrollable but nonlinearly controllable. In particular, it allows for identification of the ability to generate motions along unactuated (nonintuitive) directions through specific interactions between the system dynamics and control inputs.

In this Dissertation, differential-geometric control theory is utilized to analyze the nonlinear controllability of airplane flight dynamics. This study lead to several discoveries. First, it is found that an airplane in an upset situation where all control surfaces are blocked (inoperative) and linear controllability is lost, nonlinear controllability can be recovered using engine control only. More importantly, the study reveals unconventional mechanisms to generate motion along different directions in the state space. In particular, a novel roll mechanism that relies on nonlinear interactions between the elevator and aileron control surfaces is discovered. This novel roll mechanism is found to be superior in comparison to the conventional one (using ailerons only) near stall. Using differential-geometric control tools (e.g., non-holonomic motion planning and Fliess functional expansion), it is shown that the discovered roll mechanism can provide four times rolling motion near stall in comparison to the conventional roll control using ailerons. This result suggests that the discovered roll mechanism will provide a significant solution to the loss of control problem near stall, which is the leading cause of fatal accidents in general aviation airplanes.

Combined with *chronological calculus*, differential-geometric control theory provides rigorous analysis tools for time-varying vector fields, such as higher-order averaging of time-periodic systems and decomposition of multi-scale time-varying vector fields. These tools are applied, in this Dissertation, to the multi-body, time-periodic, flapping-wing flight dynamics. The rigorous analysis using these combined geometric-control-averaging techniques revealed unconventional balance and stability characteristics in the rich flapping flight dynamics of insects/birds. In particular, in contrast to the prevailing belief in the flapping flight dynamics community that insects are unstable at hover due to the lack of pitch stiffness, the current analysis revealed that flapping species enjoy a vibrational stabilization mechanism. That is, the natural wing periodic forcing induces a passive stabilization mechanism in the form of pitch stiffness, similar to the Kapitza pendulum.

Chapter 1

Introduction

In this chapter, a brief introductory tour to differential-geometric control theory and its aerospace-related applications is given. Section 1.1 covers the definition of the theory and some historical remarks. Section 1.2 outlines the main control-theoretic gains and flight-dynamics applications of differential-geometric control theory.

1.1 Differential-Geometric Control Theory

Differential-geometric control theory exploits *differential geometry* in the analysis of dynamical control systems. Differential geometry is a mathematical discipline that is concerned with studying calculus on curved (non-Euclidean) spaces. The main focus of this Dissertation is to formulate modern aeronautical engineering applications in a differential-geometric control framework.

Frequency-response methods (classical control theory) had been the prevalent tool in control systems analysis and design over the first half of the twentieth century. Frequency-response methods, however, are mostly limited to single-input-single-output (SISO), linear time-invariant (LTI) control systems. The space race in the 1950s was one of the most important factors necessitating the development of more sophisticated control theories that are able to deal with multi-input-multi-output (MIMO), nonlinear, possibly time-varying, control systems. Consequently, control theoreticians started to revert back to the original and natural way of studying such systems; i.e., time domain. Analyzing dynamical control systems through time-domain methods allowed more intrinsic and global representation of the rich behavior of nonlinear dynamical control systems. These efforts led to the development of state-space representation (modern control theory) and optimal control theory. The development of state-space methods and Kalman filtering, primarily by Rudolf E. Kalman [3, 4, 5, 6], was a major turning point in the history of control theory.

As the modern control theory became mature enough, control theoreticians pursued the extension of all the developed linear systems notions (stability, controllability, etc.) to nonlinear systems [7, 8, 9]. However, the non-Euclidean state-space manifold nature of some of these nonlinear systems was a major roadblock in the way to achieve this endeavor. This dilemma necessitated the incorporation of differential geometry into control theory, which led to what we call now differential-geometric control theory or geometric nonlinear control theory.

The vast majority of the development and breakthroughs in differential-geometric control theory took place over the 1970's and 1980's. The main focus of the theoreticians was to account for the underlying state-space manifold while formulating and analyzing such nonlinear dynamical control systems. As such, all the well-developed notions and properties of linear systems (e.g, controllability) can be redefined in a geometric-nonlinear fashion. Moreover, global results that represent the intrinsic behavior of the system rather than its local-coordinate representation could be obtained. The next section outlines the major aspects of differential-geometric control theory and their intersections with aircraft flight dynamics and control.

1.2 Engineering Payoffs from Differential-Geometric Control Theory

Control theory can benefit from differential geometry in the following three major aspects [10]: (i) global intrinsic assessment of the system behavior; (ii) motion generation along unactuated directions and nonlinear motion planning; and (iii) analysis of time-periodic systems and vibrational stabilization. The last two aspects are, in fact, the core motives of this effort. In the rest of this section, we will explore each one of these aspects individually and briefly allude to their flight-dynamics applications that are investigated in this dissertation.

1.2.1 Global Intrinsic Assessment of Dynamical System Behavior

A manifold is defined to be everywhere locally *diffeomorphic* to a Euclidean space; i.e., there is a smooth mapping (with a smooth inverse) between the manifold and the Euclidean space locally at each point [11]. As such, the common approach to analyze such systems is to locally parameterize the state-space manifold by a set of Euclidean coordinates (e.g., positions and velocities), then study the local behavior of the system in Euclidean space. However, this approach is essentially local and may lead to false conclusions about the global behavior of the system.

A typical example in the literature is a dynamical system having a rotational degree of freedom with one equilibrium. Consider the following system

$$\begin{array}{rcl} \dot{\theta} & = & \omega \\ \dot{\omega} & = & u \end{array}, \tag{1.1}$$

where $\theta \in S^1, \omega \in \mathbb{R}$. One approach to stabilize this system is to design a continuous feedback control law aiming for a globally asymptoticly stable equilibrium point. Deceptively, the closed-loop system, represented in local coordinates (i.e., considering $\theta \in \mathbb{R}$), indeed, has a globally asymptotically stable equilibrium. However, Bhat and Bernstein [12] proved in the year 2000, using differential-geometric control tools, that the true system evolving on the non-Euclidean space (due to the rotational degree of freedom) cannot have such a global property using continuous feedback. This result was naturally obtained once the system dynamics was represented in its intrinsic, non-Euclidean, manifold and the appropriate differential-geometric control tools were employed. This finding, indeed, warrants a re-visit to many problems in the area of rigid body attitude dynamics and stabilization.

1.2.2 Nonlinear Controllability and Motion Generation along Unactuated Directions

Controllability is the ability to steer the system from a given initial point $\boldsymbol{x}_0$ to a given final point $\boldsymbol{x}_1$ in finite time. Consider a linear system

$$\dot{\boldsymbol{x}}(t) = \boldsymbol{A}\boldsymbol{x}(t) + \boldsymbol{B}\boldsymbol{u}(t),\ \boldsymbol{x} \in \mathbb{R}^n. \tag{1.2}$$

Analyzing the controllability of such a system is quite simple. If rank of the controllability matrix, $\boldsymbol{C} = \begin{bmatrix}\boldsymbol{B} & \boldsymbol{A}\boldsymbol{B} & \boldsymbol{A}^2\boldsymbol{B} & .... & \boldsymbol{A}^{n-1}\boldsymbol{B}\end{bmatrix}$, equals n, then the system is controllable (Kalman rank condition [13]). Moreover, for linear systems, the controllability is global (i.e., if the condition is satisfied, then the system can be steered from any arbitrary $\boldsymbol{x}_0$ to another point $\boldsymbol{x}_1$). Nonlinear systems, however, do not abide by this rule. That is, the controllability should be checked locally at each point $\boldsymbol{x}_0$. Consider a nonlinear system

$$\dot{\boldsymbol{x}}(t) = \boldsymbol{f}(\boldsymbol{x}(t)) + \sum_{i=1}^{m} \boldsymbol{g}_i(\boldsymbol{x}(t))u_i(t),\ \boldsymbol{x} \in \mathbb{M}^n, \tag{1.3}$$

where $\mathbb{M}^n$ is the state-space manifold. A sufficient condition for local controllability at $\boldsymbol{x}_0 \in \mathbb{M}^n$ is to satisfy controllability of the linearization around that point. As such, after linearization, one obtains the following system

$$\dot{\boldsymbol{y}}(t) = \boldsymbol{A}\boldsymbol{y}(t) + \boldsymbol{B}\boldsymbol{u}(t), \ \boldsymbol{y} \in \mathbb{R}^n, \tag{1.4}$$

where $\boldsymbol{y} = \boldsymbol{x} - \boldsymbol{x}_0$, $\boldsymbol{A} = \left[\frac{\partial \boldsymbol{f}}{\partial \boldsymbol{x}}\right]\Big|_{\boldsymbol{x}_0}$, $\boldsymbol{B} = [\boldsymbol{b}_1, ..., \boldsymbol{b}_m]$, and $\boldsymbol{b}_i = \boldsymbol{g}_i(\boldsymbol{x}_0)$. The controllability of the linearized system (1.4) can then be easily checked using the controllability rank condition for linear systems. We emphasize that the previous condition is only sufficient (i.e., not necessary). That is, if the linearized system is controllable, then the nonlinear system is locally controllable at $\boldsymbol{x}_0$; the vice versa is not true.

In light of the previous discussion, since the controllability of the linearization is only a sufficient condition for the controllability of the nonlinear system, there exists a class of systems that are not linearly controllable, yet nonlinearly controllable. This is, indeed, the main motive behind studying nonlinear controllability. These situations are very often associated with the ability to generate motions along unactuated directions (directions over which direct control authority is missed). A simple typical example in the literature that illustrates this situation is the planar car kinematics problem. Consider a car with three degrees of freedom (as shown in Fig. 1.1): forward/backward motion, sideways motion, and rotation around its body-fixed origin. Two controls are available: u_1 is the forward/backward speed and u_2 is the steering

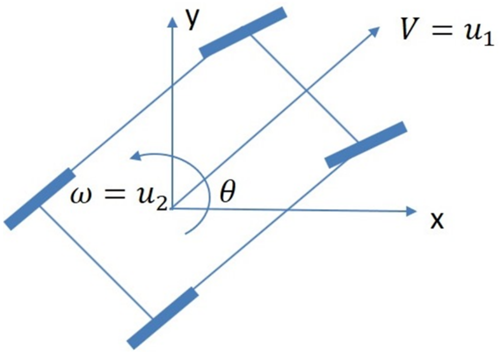

Figure 1.1: A three degrees-of-freedom car with two inputs.

angular velocity. As such, the dynamic equations are written as

$$\frac{d}{dt}\begin{pmatrix} x(t) \\ y(t) \\ \theta(t) \end{pmatrix} = \begin{pmatrix} \cos\theta(t) \\ \sin\theta(t) \\ 0 \end{pmatrix} u_1(t) + \begin{pmatrix} 0 \\ 0 \\ 1 \end{pmatrix} u_2(t), \tag{1.5}$$

which can be abstractly written as $\dot{\boldsymbol{x}}(t) = \boldsymbol{g}_1(\boldsymbol{x}(t))u_1(t) + \boldsymbol{g}_2(\boldsymbol{x}(t))u_2(t)$. It should be noted that since there is no drift vector field $\boldsymbol{f}(\boldsymbol{x}(t))$, the linearized dynamics has a zero $\boldsymbol{A}$ matrix. Hence, the controllability matrix is constructed using the $\boldsymbol{B}$ matrix only, and can be written as

$$\boldsymbol{C} = \begin{bmatrix} \cos\theta_0 & 0 \\ \sin\theta_0 & 0 \\ 0 & 1 \end{bmatrix}. \tag{1.6}$$

It is readily observed that the rank of the controllability matrix above is *two* $\forall\theta_0$. That is, the system at hand (1.5) is linearly uncontrollable. This result is physically intuitive because the systems lacks a direct actuation over the sideways motion direction. However, nonlinear controllability analysis investigates both direct and indirect actuation mechanisms. Therefore, exploiting differential-geometric control tools, nonlinear controllability analysis yields the system (1.5) nonlinearly controllable. In particular, the inability to directly actuate the sideways motion is compensated for by exploiting a nonlinear interaction between the two available controls: forward/backward motion and steering. This nonlinear interaction is called a *Lie bracket*. The Lie bracket between the two available control vector fields is written as $[\boldsymbol{g}_1,\ \boldsymbol{g}_2]$, and is computed as $[\boldsymbol{g}_1,\ \boldsymbol{g}_2] = \frac{\partial \boldsymbol{g}_2}{\partial \boldsymbol{x}}\boldsymbol{g}_1 - \frac{\partial \boldsymbol{g}_1}{\partial \boldsymbol{x}}\boldsymbol{g}_2$. One way to realize the motion along the direction of the Lie bracket $[\boldsymbol{g}_1,\ \boldsymbol{g}_2]$ is to command a piecewise constant variations of the associated control inputs to achieve the following sequence: flow along $\boldsymbol{g}_1$, then along $\boldsymbol{g}_2$, then backward along $\boldsymbol{g}_1$, and finally backward along $\boldsymbol{g}_2$. The net outcome of the previous input sequence is a pure motion along the direction of the Lie bracket $[\boldsymbol{g}_1,\ \boldsymbol{g}_2]$, which aligns with the sideways motion direction. It is worth mentioning that the realization of the sideways motion Lie bracket is quite similar to what we do in parallel parking.

This concept can be generalized to many nonlinear dynamical control systems, where the question is "Will the system remain controllable, if one or more actuators are lost?" One example is the attitude dynamics of a spacecraft (rigid body) where it has been shown that the system remains controllable even if one or two pairs of gas jets are removed [14], in spite of the system being linearly uncontrollable. As such, applying this tool to aircraft flight dynamics is one of the main focus areas of this dissertation and is the underpinning concept of Chapter 3. In particular, we apply nonlinear controllability analysis to fixed-wing airplane flight dynamics at full hydraulic failure (complete loss of all control surfaces) to prove that the airplane can be (under some conditions) fully nonlinearly controllable using thrust-only flight control. Moreover, through nonlinear controllability analysis, we discover a new rolling mechanism that can compensate for the loss of aileron roll sensitivity near stall.

Upon discovering a new direction of motion that is associated with a Lie bracket, one asks the next question: "How can we precisely realize motion along that direction?" Such question is intimately connected to *motion planning*. The motion planning problem (MPP) is the problem of finding a control input $\boldsymbol{u}(t)$ that steers a control system between two arbitrarily given points. MPP has been solved a long time ago for linear systems provided that the Kalman rank condition is satisfied. In fact, an analytical formula is available for a steering control input between any two points in case of unbounded controls and no obstacles. That is, if the controllability matrix $\boldsymbol{C}$ is of full rank, then the following relation provides a control input history that steers the linear system (1.2) from $\boldsymbol{x}_0$ at t_0 to $\boldsymbol{x}_1$ at t_1 [15, PP. 74–77]

$$\begin{aligned} \boldsymbol{u}(t) &= -\boldsymbol{B}^\intercal\ \boldsymbol{\Phi}^\intercal(t_0,t)\ \boldsymbol{W}^{-1}(t_0,t_1)\ \big(\boldsymbol{x}_0 - \boldsymbol{\Phi}(t_0,t_1)\ \boldsymbol{x}_1\big) \\ \boldsymbol{W}(t_0,t_1) &= \int_{t_0}^{t_1} \boldsymbol{\Phi}(t_0,t)\ \boldsymbol{B}\ \boldsymbol{B}^\intercal\ \boldsymbol{\Phi}^\intercal(t_0,t)\ dt \end{aligned} \tag{1.7}$$

where $\intercal$ denotes transpose, $\boldsymbol{\Phi}$ is the state transition matrix which is defined as $\boldsymbol{\Phi}(t_0, t) = e^{-\boldsymbol{A}t}$. It should be noted that the control law (1.7) minimizes the integral $\int_{t_0}^{t_1} ||\boldsymbol{u}(t)||^2 dt$ of control energy needed for steering.

Such a closed-form solution for the minimum energy steering control input for nonlinear system does not exist. Solving the MPP for nonlinear systems that rely on Lie brackets to achieve controllability naturally invokes differential-geometric control tools in order to realize motion along the directions of those Lie brackets. Several algorithms have been developed for the motion planning of nonlinear driftless ($\boldsymbol{f}(\boldsymbol{x}) = 0$) systems over the 1990's using differential-geometric control tools [16, 17, 18, 19, 20, 21, 22]. Nevertheless, nonlinear systems with drift have been almost left unexplored. In Chapter 3 of this dissertation, we extend the nonlinear motion planning algorithm provided by Liu [21] to a special class of nonlinear systems with drift in order to implement the newly-discovered nonlinear roll mechanism that proved to be more effective than the conventional one near stall.

1.2.3 Time-Periodic Systems and Vibrational Stabilization

Differential geometric control theory provides quite powerful tools to analyze time-varying vector fields. In particular, combined with *chronological calculus* [23], differential geometric control theory provides rigorous higher-order averaging tools for the analysis of time-periodic systems. One very useful application is the analysis of *vibrational control* systems. Vibrational control is a time-varying control technique that exploits oscillatory control inputs to provide new directions of motion or stabilize the system around a certain equilibrium point [24, 25, 26, 27]. *Vibrational stabilization* is a vibrational-control phenomenon that exploits a sufficiently high-amplitude, high-frequency, periodic forcing to convert an unstable equilibrium point into an asymptoticly stable one. A well-known manifestation of this phenomenon is the Stephenson-Kapitza pendulum [28, 29, 30]: the application an oscillatory control input to the pendulum pivot provides an artificial torsional spring action that may convert the unstable inverted pendulum equilibrium point into an asymptoticly stable one.

The application of these tools to the flapping-wing flight dynamics is another main focus area of this dissertation and is the underpinning idea of Chapter 4. In particular, by formulating the multi-body dynamics of flapping-wing micro-air-vehicles in a differential-geometric-control framework, a vibrational stabilization mechanism that greatly contributes to the body pitch stabilization is revealed. The discovered vibrational stabilization mechanism is induced by the interaction between the fast oscillatory aerodynamic loads on the wings and the relatively-slow body motion. This stabilization mechanism provides an artificial stiffness (i.e., spring action) to the body rotation around its pitch axis, and is similar to that of Kapitza pendulum.

Chapter 2

Differential-Geometric Mathematical Tools for Dynamics and Control Applications

In order to make this dissertation self-contained, all the mathematical and control-theoretic tools used throughout this dissertation are outlined in this chapter. In particular, various tools from differential-geometric control theory are outlined. These tools include: (i) nonlinear controllability analysis and how it differs from the linear one; (ii) nonlinear motion planning and the realization of motion along unactuated directions; and (iii) analysis of time-varying vector fields. Moreover, the most relevant tools from averaging theory are summarized.

2.1 Nonlinear Controllability and Motion Planning

2.1.1 Linear Controllability

A linear, time-invariant, system is typically written as

$$\dot{\boldsymbol{x}}(t) = \boldsymbol{A}\boldsymbol{x}(t) + \boldsymbol{B}\boldsymbol{u}(t), \tag{2.1}$$

where $\boldsymbol{x}$ is the state vector $(n \times 1)$, $\boldsymbol{u}$ is the control input vector $(m \times 1)$, $\boldsymbol{A}$ is the state matrix $(n \times n)$, and $\boldsymbol{B}$ is the input matrix $(n \times m)$. A necessary and sufficient condition for the controllability of the system (2.1) is that the $(n \times nm)$ controllability matrix, $\boldsymbol{C} = \begin{bmatrix}\boldsymbol{B} & \boldsymbol{A}\boldsymbol{B} & \boldsymbol{A}^2\boldsymbol{B} & .... & \boldsymbol{A}^{n-1}\boldsymbol{B}\end{bmatrix}$, has to be of full row rank (i.e. rank($\boldsymbol{C}$)=n) [13].

Consider the nonlinear, control-affine system defined by

$$\dot{\boldsymbol{x}}(t) = \boldsymbol{f}(\boldsymbol{x}(t)) + \sum_{i=1}^{m} \boldsymbol{g}_i(\boldsymbol{x}(t))u_i(t), \tag{2.2}$$

where $\boldsymbol{f}(\boldsymbol{x}(t))$ is the drift vector field (uncontrolled dynamics) and $\boldsymbol{g}_i(\boldsymbol{x}(t))$ is the control input vector field associated with the control input $u_i(t)$. Assume, without loss of generality, that $\boldsymbol{x}_0$ is an equilibrium point (i.e. $\boldsymbol{f}(\boldsymbol{x}_0) = 0$). A sufficient condition for the local controllability of the system (2.2) at $\boldsymbol{x}_0$ is that the linearization about $\boldsymbol{x}_0$

$$\Delta\dot{\boldsymbol{x}}(t) = \left[\frac{\partial \boldsymbol{f}}{\partial \boldsymbol{x}}\right]\Bigg|_{\boldsymbol{x}_0} \Delta\boldsymbol{x}(t) + \sum_{i=1}^{m} \boldsymbol{g}_i(\boldsymbol{x}_0)u_i(t)$$

to be controllable. That is, the controllability matrix

$$\begin{aligned}\boldsymbol{C} = \Bigg[&\boldsymbol{g}_1, ..., \boldsymbol{g}_m, \left[\frac{\partial \boldsymbol{f}}{\partial \boldsymbol{x}}\right]\Bigg|_{\boldsymbol{x}_0} \boldsymbol{g}_1, ..., \left[\frac{\partial \boldsymbol{f}}{\partial \boldsymbol{x}}\right]\Bigg|_{\boldsymbol{x}_0} \boldsymbol{g}_m, ..., \left[\frac{\partial \boldsymbol{f}}{\partial \boldsymbol{x}}\right]^{n-1}\Bigg|_{\boldsymbol{x}_0} \boldsymbol{g}_1, \cdots \\ &..., \left[\frac{\partial \boldsymbol{f}}{\partial \boldsymbol{x}}\right]^{n-1}\Bigg|_{\boldsymbol{x}_0} \boldsymbol{g}_m\Bigg]\end{aligned}$$

to be of full row rank [31].

2.1.2 Nonlinear Controllability

As stated before, controllability of the linearization of a nonlinear system about a given $\boldsymbol{x_0}$ is not necessary. Determination of weaker conditions for local controllability of nonlinear, control-affine systems has been thoroughly investigated using differential geometric analysis tools [32, 33, 34, 35, 36, 37]. These studies concluded that the system (2.2) is locally *accessible* at $\boldsymbol{x}_0$ if and only if the accessibility distribution

$$\boldsymbol{C} = [\boldsymbol{g}_1, \boldsymbol{g}_2, ..., \boldsymbol{g}_m, [\boldsymbol{g}_i, \boldsymbol{g}_j], ..., ad^k_{\boldsymbol{g}_i}\boldsymbol{g}_j, ..., [\boldsymbol{f}, \boldsymbol{g}_i], ..., ad^k_{\boldsymbol{f}}\boldsymbol{g}_i] \tag{2.3}$$

has rank n, where the bracket $[.,.]$ is called the *Lie bracket*, and for two vector fields $\boldsymbol{V}_1(\boldsymbol{x})$ and $\boldsymbol{V}_2(\boldsymbol{x})$ is defined as

$$[\boldsymbol{V}_1, \boldsymbol{V}_2] = \frac{\partial \boldsymbol{V}_2}{\partial \boldsymbol{x}}\boldsymbol{V}_1 - \frac{\partial \boldsymbol{V}_1}{\partial \boldsymbol{x}}\boldsymbol{V}_2.$$

Also, $ad^k_{\boldsymbol{f}}\boldsymbol{g} = [\boldsymbol{f}, ad^{k-1}_{\boldsymbol{f}}\boldsymbol{g}]$ and $ad^1_{\boldsymbol{f}}\boldsymbol{g} = [\boldsymbol{f}, \boldsymbol{g}]$. This condition is called the *Lie Algebraic Rank Condition* (LARC).

The accessibility property at $\boldsymbol{x}_0$ implies that the set $\mathcal{R}$ of reachable points from $\boldsymbol{x}_0$ has a non-empty interior. In general, accessibility is weaker than controllability. In fact, the accessibility property implies the ability to move in all directions around $\boldsymbol{x}_0$ (i.e., controllability), however, there might be uni-directional motion along one or more axes. That is, the main difference between accessibility and controllability is that we may be able to generate motion along some direction, but cannot reverse motion along that direction. For driftless systems ($\boldsymbol{f}(\boldsymbol{x}) = 0$), accessibility and controllability are equivalent.

It is interesting to note that the linear controllability condition of the system (2.2) can be written in the language of differential geometry as

$$\boldsymbol{C} = \left[\boldsymbol{g}_1, ..., \boldsymbol{g}_m, [\boldsymbol{f}, \boldsymbol{g}_1], ..., [\boldsymbol{f}, \boldsymbol{g}_m], ..., ad_{\boldsymbol{f}}^{n-1}\boldsymbol{g}_1, ..., ad_{\boldsymbol{f}}^{n-1}\boldsymbol{g}_m\right].$$

From the above discussion, it is seen that the Lie brackets between control vector fields $[\boldsymbol{g}_i, \boldsymbol{g}_j]$ and the higher order Lie brackets (e.g., $[[\boldsymbol{f}, \boldsymbol{g}_i], \boldsymbol{g}_j]$) are not included in the linear analysis, and hence, may provide unconventional mechanisms to generate motion or change the controllability characteristics of a given system. As such, these terms will be the main focus of this effort.

2.1.3 Nonlinear Motion Planning

As we explained in the previous subsection, the Lie brackets of the form $\mathrm{ad}_{\boldsymbol{f}}^k \boldsymbol{g}_i$ represent direct control action (i.e., captured by linear controllability analysis), and are analogous to the matrix products required for linear controllability (e.g., AB, A^2B). However, the Lie brackets generated by control vector fields only (e.g., $[\boldsymbol{g}_i, \boldsymbol{g}_j]$) are not included in linear controllability analysis and represent indirect/nonlinear control action. Hence, we call them *nonlinear Lie brackets*. If only Lie brackets of the form $\mathrm{ad}_{\boldsymbol{f}}^k \boldsymbol{g}_i$ are used to satisfy the LARC, then that implies the controllability of the linearization. This is not the case if nonlinear Lie brackets are used to satisfy the LARC. In such a case, there are some directions of motion that are not directly actuated. Therefore, a means to indirectly generate motions along those directions is sought, hence the need for nonlinear motion planning techniques.

In this section, we consider a nonlinearly controllable system that relies on some nonlinear Lie brackets to satisfy its LARC. This implies that such a system has some directions of motion that are not directly actuated. Therefore, we appeal to the nonlinear motion planning techniques to devise a way to indirectly generate motions along those directions. In other words, we seek a method/algorithm to realize motion along the directions of nonlinear Lie bracket vector fields. Liu [21] provided such an algorithm for nonlinear driftless systems. He considered systems of the form

$$\dot{\boldsymbol{x}}(t) = \sum_{i=1}^{m} \boldsymbol{g}_i(\boldsymbol{x}(t))\; u_i(t). \tag{2.4}$$

He studied the relation between the trajectories of the system (2.4) and those of the extended system

$$\dot{\boldsymbol{x}}(t) = \sum_{k=1}^{r} \boldsymbol{g}_k(\boldsymbol{x}(t))\; v_k(t),\;\; r > m, \tag{2.5}$$

where the first m vector fields are the control vector fields in (2.4), and the vector fields $\boldsymbol{g}_k,\ k = m + 1, ..., r$ are the Lie brackets of the control vector fields. In other words, he solved the following problem: given a certain extended input $\boldsymbol{v}(t)$, what is the ordinary input $\boldsymbol{u}(t)$ that would generate the same trajectory as $\boldsymbol{v}(t)$. Liu published a companion paper [38] in which he used averaging techniques to show sufficient conditions under which the trajectories of (2.4) generated by sequences of ordinary inputs $\boldsymbol{u}^j$ converge to trajectories of the extended system (2.5). It should be noted that Haynes and Hermes [39] previously had proved that if system (2.4) satisfies the LARC condition, then every trajectory of (2.5) can be uniformly approximated by trajectories of (2.4). However, they did not provide a constructive procedure for producing such a sequence. Liu [21] indicated that his algorithm could be extended to a class of nonlinear systems with drift where only Lie brackets between control vector fields are to be realized. Such a class encompasses a nonlinear motion generation problem considered in Sec. 3.5. Hence, in the following subsection, we outline a framework for motion planning of a class of nonlinear systems with drift using Liu's algorithm specialized for Lie brackets that involve only two control vector fields.

2.1.4 Framework for Approximate Tracking of a Class of Nonlinear Systems with Drift

We consider a nonlinear systems with drift on the same form as system (2.2). The extended version of this class of systems can be written as

$$\dot{\boldsymbol{x}}(t) = \boldsymbol{f}(\boldsymbol{x}(t)) + \sum_{k=1}^{r} \boldsymbol{g}_k(\boldsymbol{x}(t))\ v_k(t),\ r > m, \tag{2.6}$$

where the vector fields $\boldsymbol{g}_k$, $k = m+1, ..., r$ are the Lie brackets of the control vector fields that are needed to complement the accessibility distribution used to satisfy the LARC. That is, the accessibility distribution that is used to satisfy the LARC for this class of systems can be written as

$$\boldsymbol{C} = \left[\boldsymbol{g}_1, \boldsymbol{g}_2, ..., \boldsymbol{g}_m, [\boldsymbol{f}, \boldsymbol{g}_1], ..., [\boldsymbol{f}, \boldsymbol{g}_m], ..., ad_{\boldsymbol{f}}^{n-1}\boldsymbol{g}_1, ..., ad_{\boldsymbol{f}}^{n-1}\boldsymbol{g}_m, \boldsymbol{g}_{m+1}, \boldsymbol{g}_{m+2}, ..., \boldsymbol{g}_r\right],$$

where the vector fields $\boldsymbol{g}_{m+1}, ..., \boldsymbol{g}_r$ are Lie brackets of control vector fields only (i.e., nonlinear Lie brackets) and are treated as direct inputs in the extended system. The framework we present here consists of two steps. The first step is to obtain the extended inputs needed to (i) steer the system from an initial point $\boldsymbol{x}_0$ to a final point $\boldsymbol{x}_f$; or (ii) track a desired trajectory $\boldsymbol{x}_d(t)$. The second step is to employ Liu's algorithm [21] to transform the extended inputs into ordinary inputs.

Step 1: The Extended Inputs

We denote the matrix constructed by stacking the extended control input vector fields ($\boldsymbol{g}'_k s$) together after evaluation at certain point $\boldsymbol{x} \in M$ by $G(\boldsymbol{x})$. As such, the extended inputs needed to track some prescribed trajectory can be obtained as

$$\boldsymbol{v}(t) = G(\boldsymbol{x}_d(t))^{\dagger}\Big(\dot{\boldsymbol{x}}_d(t) - \boldsymbol{f}(\boldsymbol{x}_d(t))\Big), \tag{2.7}$$

where $G(\boldsymbol{x}_d) = [\boldsymbol{g}_1(\boldsymbol{x}_d), ..., \boldsymbol{g}_r(\boldsymbol{x}_d)]$, † denotes pseudo inverse, and $\boldsymbol{x}_d$ is a desired trajectory in case of trajectory tracking or a suggested path that connects the initial point to the final point in case of motion planning. Note that this is not the only way to obtain the extended inputs. For example, the extended inputs could be obtained through solving an optimal control problem that minimizes certain cost function (e.g., minimum time problem).

Step 2: From Extended to Ordinary Inputs

Now, we move to the next step which is transforming the obtained extended inputs into ordinary inputs u_k, for $k \in \{1, ..., m\}$. We are particularly interested in realizing Lie brackets that involve only two vector fields (first order Lie brackets). Consider an extended input vector field $\boldsymbol{g}_{k_3} = [\boldsymbol{g}_{k_1}, \boldsymbol{g}_{k_2}]$ where $k_1, k_2 \in \{1, ..., m\}$. Denote the extended input associated with $\boldsymbol{g}_{k_3}$ by v_{k_3}. Assume that $v_{k_3}(t)$ needed to track a specific trajectory over $t \in [0, T]$ has been obtained. Then, according to Liu [21], the motion along the Lie bracket vector field $\boldsymbol{g}_{k_3}$ can be realized through the following sequence of ordinary control inputs $u_{k_1}(t)$ and $u_{k_2}(t)$

$$\begin{aligned} u^j_{k_1}(t) &= -\sqrt{j}\ \omega\ v_{k_3}(t)\sin(j\omega t) \\ u^j_{k_2}(t) &= 2\sqrt{j}\ \cos(j\omega t) \end{aligned}, \tag{2.8}$$

where $\omega \in \mathbb{R} - \{0\}$, and j is a positive integer. This sequence (2.8), when applied to the ordinary system (2.2), generates a trajectory that converges to that of the extended system (2.6) as $j \to \infty$.

2.2 Combined Geometric-Control-Averaging Analysis Tools

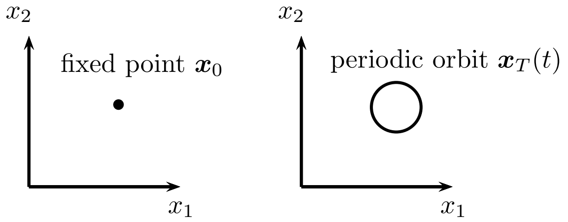

Figure 2.1: An illustration of the difference between fixed point and periodic orbit.

Analysis of nonlinear time-periodic (NLTP) systems requires a different set of tools than those used for nonlinear time-invariant (NLTI) systems. The essential difference between NLTP and NLTI systems emanates from the fact that an equilibrium state of NLTP systems is generally represented by a *periodic orbit* (PO), as opposed to a fixed point for NLTI systems. That is, at equilibrium, every state of the NLTP system takes a periodic sequence of values with some time period T. Figure 2.1 shows a simple illustration of difference between fixed point and periodic orbit equilibrium in a two-dimensional state space.

Stability analysis of NLTP flapping-wing dynamics could be performed on the original time-periodic system by numerically capturing a periodic orbit associated with a certain equilibrium condition and analyzing its linear stability through *Floquet theorem* [40, 41, 42]. However, very little insights into stabilizing/destabilizing mechanisms could be obtained through this purely-numerical approach. On the other hand, a time-invariant version of the NLTP flapping-wing dynamics could be obtained through averaging techniques (reviewed next). As such, the periodic orbit representing equilibrium is converted into a fixed point, around which the system could be linearized. Stability analysis is then easily performed for the linear time-invariant (LTI) system via eigenvalue analysis. Furthermore, utilizing the simple and tractable form of LTI systems, the stability of linearized, time-invariant, flapping-wing dynamics could be analytically scrutinized. Hence, insights into different stabilizing/destabilizing mechanisms (e.g., stiffness or damping) could be gained.

2.2.1 Averaging Theorem

The averaging theorem is a simple tool that could be used to convert a NLTP system into a NLTI one. However, it possesses several limitations, which will be discussed in the following subsections. Theorem 1 provides the formal statement of the standard averaging theorem.

Theorem 1. Consider the NLTP system

$$\dot{\boldsymbol{x}}(t) = \epsilon \boldsymbol{X}(\boldsymbol{x}(t), t), \tag{2.9}$$

where $0 < \epsilon \ll 1$ is a small perturbation scale, e.g., ϵ could be seen as the reciprocal of the frequency when the system is subject to high-frequency forcing. Assuming that $\boldsymbol{X}$ is a T-periodic vector field in t, the averaged dynamical system corresponding to (2.9) is written as

$$\dot{\overline{\boldsymbol{x}}}(t) = \epsilon \overline{\boldsymbol{X}}(\overline{\boldsymbol{x}}(t)), \tag{2.10}$$

where $\overline{\boldsymbol{X}}(\overline{\boldsymbol{x}}(t)) = \frac{1}{T}\int_0^T \boldsymbol{X}(\boldsymbol{x}(t), \tau)\, d\tau$. According to the averaging theorem [43, 44, 45]:

- If $\boldsymbol{x}(0) - \overline{\boldsymbol{x}}(0) = O(\epsilon)$, then there exist $b > 0$ and $\epsilon^* > 0$ such that $\boldsymbol{x}(t) - \overline{\boldsymbol{x}}(t) = O(\epsilon)$ $\forall t \in [0, b/\epsilon]$ and $\forall \epsilon \in [0,\epsilon^*]$.
- If $\boldsymbol{x}^*$ is an exponentially stable equilibrium point of (2.10) and if $\|\boldsymbol{x}(0) - \boldsymbol{x}^*\| < \rho$ for some $\rho > 0$, then $\boldsymbol{x}(t) - \overline{\boldsymbol{x}}(t) = O(\epsilon)$ $\forall t > 0$ and $\forall \epsilon \in [0,\epsilon^*]$. Moreover, The system (2.9) has a unique, exponentially stable, T-periodic solution $\boldsymbol{x}_T(t)$ with the property $\|\boldsymbol{x}_T(t) - \boldsymbol{x}^*\| \leq k\epsilon$ for some k.

Thus, the averaging approach allows converting a non-autonomous system into an autonomous system. As such, if the equilibrium state of the NLTP system is represented by a periodic orbit $\boldsymbol{x}_T(t)$, it reduces to a fixed point of the averaged dynamics. The problem of ensuring a specific periodic orbit corresponding to a desired equilibrium configuration is significantly simplified using the averaging approach, hence allowing for analytical results.

2.2.2 Nonlinear Variation of Constants Formula (VOC)

The nonlinear variation of constants formula is a differential-geometric tool that is used to split the flow along two vector fields. Consider a nonlinear system subjected to a high-frequency, high-amplitude, periodic forcing in the form

$$\dot{\boldsymbol{x}}(t) = \boldsymbol{f}(\boldsymbol{x}(t)) + \frac{1}{\epsilon}\,\boldsymbol{g}\left(\boldsymbol{x}(t), \frac{t}{\epsilon}\right), \qquad \boldsymbol{x}(0) = \boldsymbol{x}_0, \tag{2.11}$$

where $0 < \epsilon \ll 1$. The time-varying vector field $(1/\epsilon)\boldsymbol{g}(\boldsymbol{x}(t), t/\epsilon)$ is assumed to be periodic in its second argument with period T. The system (2.11) is not amenable to direct averaging, i.e., is not in the form of (2.9), because $\boldsymbol{f}$ and $\boldsymbol{g}$ are not of the same order. The VOC resolves this issue by approximating the flow $\phi_{0,T}^{\boldsymbol{f}+\boldsymbol{g}}(\boldsymbol{x}_0)$ (i.e., flow along $\boldsymbol{f}+\boldsymbol{g}$ for a period T starting at initial point $\boldsymbol{x}_0$) by a flow along the vector field $\boldsymbol{g}$ staring at a different initial condition $\delta\boldsymbol{x}_0$. That is, $\phi_{0,T}^{\boldsymbol{f}+\boldsymbol{g}}(\boldsymbol{x}_0) = \phi_{0,T}^{\boldsymbol{g}}(\delta\boldsymbol{x}_0)$, where the new initial point $\delta\boldsymbol{x}_0$ is obtained through the flow along a new vector field $\boldsymbol{F}$ that is introduced by the VOC formula. Figure 2.2 shows a simple explanatory sketch for the application of the VOC formula to the system (2.11). As such, the VOC formula allows separation of the system (2.11) into two companion systems as follows [23], [46]

$$\begin{array}{rcll} \dot{\boldsymbol{z}}(t) & = & \boldsymbol{F}(\boldsymbol{z}(t), t), & \boldsymbol{z}(0) = \boldsymbol{x}_0 \\ \dot{\boldsymbol{x}}(t) & = & \boldsymbol{g}(\boldsymbol{x}(t), t), & \boldsymbol{x}(0) = \delta\boldsymbol{x}_0 = \boldsymbol{z}(t) \end{array}, \tag{2.12}$$

where $\boldsymbol{F}$ is the *pullback* of the vector field $\boldsymbol{f}$ along the flow $\phi_t^{\boldsymbol{g}}$ of the time-varying vector field $\boldsymbol{g}$. Using the chronological calculus formulation of Agrachev and Gamkrelidze [23], Bullo [47] showed that, for a time-invariant $\boldsymbol{f}$ and time-varying $\boldsymbol{g}$, the pullback vector field $\boldsymbol{F}(\boldsymbol{x}(t), t)$

can be written as

$$\boldsymbol{F}(\boldsymbol{x}(t),t) \quad = \quad \boldsymbol{f}(\boldsymbol{x}(t)) + \sum_{k=1}^{\infty} \int\limits_{0}^{t} \dots \int\limits_{0}^{s_{k-1}} \left(ad_{\boldsymbol{g}(\boldsymbol{x}(t),\ s_k)} \dots ad_{\boldsymbol{g}(\boldsymbol{x}(t),\ s_1)} \boldsymbol{f}(\boldsymbol{x}) \right) ds_k \dots ds_1, \qquad (2.13)$$

where $ad_{\boldsymbol{g}}\boldsymbol{f} = [\boldsymbol{g}, \boldsymbol{f}]$ is the *Lie bracket* between the two vector fields $\boldsymbol{g}$ and $\boldsymbol{f}$, and is computed as $[\boldsymbol{g}, \boldsymbol{f}] = \frac{\partial \boldsymbol{f}}{\partial \boldsymbol{x}} \boldsymbol{g} - \frac{\partial \boldsymbol{g}}{\partial \boldsymbol{x}} \boldsymbol{f}$ [31, PP. 23–72].

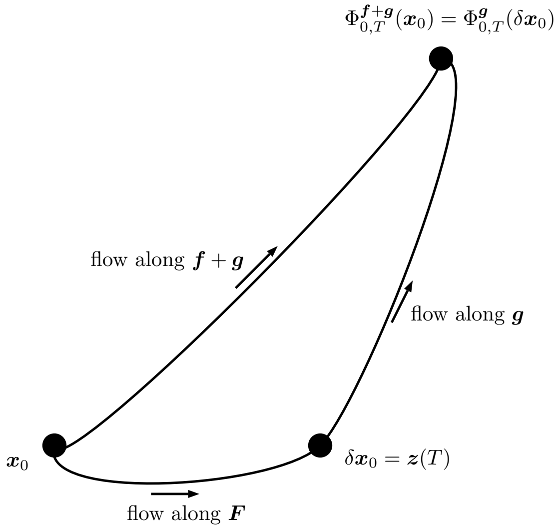

Figure 2.2: An illustration of the application of the VOC formula to system (2.11).

2.2.3 Averaging of of High-Amplitude Periodic Forcing

Since FWMAVs/insects experience high-amplitude, high-frequency, periodic forcing (i.e., in the form (2.11)). Applying the VOC formula before averaging is necessary to obtain an averaged system that accounts for the multi-body and multi-time-scale effects. The benefit of the VOC formula is that each of the systems in (2.12) is individually amenable to the averaging theorem. That is,

$$\begin{array}{rcll} \dot{\bar{\boldsymbol{z}}}(t) & = & \frac{1}{T}\int_0^T \boldsymbol{F}(\boldsymbol{z}(t),t)\ dt, & \bar{\boldsymbol{z}}(0) = \boldsymbol{x}_0 \\ \dot{\bar{\boldsymbol{x}}}(t) & = & \frac{1}{T}\int_0^T \boldsymbol{g}(\boldsymbol{x}(t),t)\ dt, & \bar{\boldsymbol{x}}(0) = \bar{\boldsymbol{z}}(t) \end{array}. \qquad (2.14)$$

It should be noted that for the considered FWMAV system (4.15) or (4.8), the time-periodic forcing vector field $\boldsymbol{Y}(\boldsymbol{x})\ \tau_{\varphi}(t)$ is of zero mean. Hence, averaging after applying the VOC implies

$$\bar{\boldsymbol{x}}(t) = \bar{\boldsymbol{z}}(t), \quad \dot{\bar{\boldsymbol{z}}} = \bar{\boldsymbol{F}}(\bar{\boldsymbol{z}}). \tag{2.15}$$

Therefore, the averaged dynamics of the original system (2.11) can be obtained just by averaging the pullback vector field $\boldsymbol{F}(\boldsymbol{x}(t), t)$. Therefore, Theorem 1 is extended next to high-frequency, high-amplitude, periodically-forced systems in the form of Eq. (2.11).

Theorem 2. Consider a NLTP system subject to a high-frequency, high amplitude, periodic forcing (2.11). Assuming that $\boldsymbol{g}$ is a T-periodic in t, zero-mean vector field and both $\boldsymbol{f}$, $\boldsymbol{g}$ are continuously differentiable, the averaged dynamical system corresponding to (2.11) is written as

$$\dot{\overline{\boldsymbol{x}}}(t) = \epsilon \overline{\boldsymbol{F}}(\overline{\boldsymbol{x}}(t)), \tag{2.16}$$

where $\overline{\boldsymbol{F}}(\overline{\boldsymbol{x}}(t)) = \frac{1}{T}\int_0^T \boldsymbol{F}(\boldsymbol{x}(t), \tau)\, d\tau$, and $\boldsymbol{F}$ is the pullback of $\boldsymbol{f}$ along the flow $\phi_t^{\boldsymbol{g}}$ of the time-varying vector field $\boldsymbol{g}$ as explained in Eq. (2.13). Moreover

- If $\overline{\boldsymbol{x}}(0) = \boldsymbol{x}(0)$, then there exist $b > 0$ and $\epsilon^* > 0$ such that $\boldsymbol{x}(t) - \overline{\boldsymbol{x}}(t) = O(\epsilon)$ $\forall t \in [0, b/\epsilon]$ and $\forall \epsilon \in [0,\epsilon^*]$.
- If $\boldsymbol{x}^*$ is an exponentially stable equilibrium point of (2.16) and if $\|\boldsymbol{x}(0) - \boldsymbol{x}^*\| < \rho$ for some $\rho > 0$, then $\boldsymbol{x}(t) - \overline{\boldsymbol{x}}(t) = O(1)$ $\forall t > 0$ and $\forall \epsilon \in [0,\epsilon^*]$. Moreover, there exists an $\epsilon_1 > 0$ such that $\forall \epsilon \in [0,\epsilon_1]$, the system (2.11) has a unique, T-periodic, locally asymptotically stable trajectory that takes values in an open ball of radius $O(1)$ centered at $\boldsymbol{x}^*$.

The main difference between Theorem 1 (direct averaging) and Theorem 2 (VOC and averaging) is that the former guarantees a periodic orbit that is $O(\epsilon)$ from the corresponding fixed point of the averaged dynamics, while the latter allows for larger variations $O(1)$ from the fixed point. This relatively large amplitude admitted by Theorem 2 is particularly useful in analyzing flapping flight while including wing dynamics where the flapping angle φ becomes a state; the amplitude of the flapping angle is typically around 60 degrees. Therefore, the application of the VOC formula is essential in analyzing flapping flight, multi-body dynamics. We are emphasizing that Theorem 1 is not a viable option in this case as direct averaging would yield trivial results when applied to the FWMAV multi-body system (4.15) or (4.8); i.e., it would neglect the entire effects of the flapping input vector field.

2.2.4 Generalized Averaging Theory

A main issue with the averaging approach is that it is valid for small enough ϵ (i.e., for high enough frequency). Moreover, this frequency limit (determined by ϵ^*) is not known; only its existence is guaranteed. The generalized averaging theory (GAT) presents a remedy for this issue by providing an arbitrarily higher-order approximation to the flow along a time-periodic vector field. Agrachev and Gamkrelidze laid the foundation for the GAT in their seminal work [23]. Later, Sarychev [48] and Vela [49] used the concepts introduced by Agrachev and Gamkrelidze to develop a generalization for the classical averaging theorem. Only the final results of the GAT are stated here, and the reader is referred to Section 4 in Ref. [50] for a detailed presentation of the GAT. Sarychev [48] introduced the notion of complete averaging to denote the following averaged dynamics of system (2.9)

$$\dot{\bar{\boldsymbol{x}}}(t) = \epsilon \bar{\boldsymbol{X}}(t) = \epsilon \boldsymbol{\Lambda}_1(\bar{\boldsymbol{x}}(t)) + \epsilon^2 \boldsymbol{\Lambda}_2(\bar{\boldsymbol{x}}(t)) + \epsilon^3 \boldsymbol{\Lambda}_3(\bar{\boldsymbol{x}}(t)) + ..., \tag{2.17}$$

where

$$
\begin{aligned}
\boldsymbol{\Lambda}_1(\bar{\boldsymbol{x}}(t)) &= \tfrac{1}{T}\int_0^T \boldsymbol{X}(\boldsymbol{x}(t),\tau)d\tau \\
\boldsymbol{\Lambda}_2(\bar{\boldsymbol{x}}(t)) &= \tfrac{1}{2T}\int_0^T \left[\int_0^t \boldsymbol{X}(\boldsymbol{x}(t),\sigma)d\sigma,\ \boldsymbol{X}(\boldsymbol{x}(t),t)\right] dt \\
\boldsymbol{\Lambda}_3(\bar{\boldsymbol{x}}(t)) &= \tfrac{T}{2}\left[\boldsymbol{\Lambda}_1(\bar{\boldsymbol{x}}(t)),\ \boldsymbol{\Lambda}_2(\bar{\boldsymbol{x}}(t))\right] + \tfrac{1}{3T}\int_0^T \left[\int_0^t \boldsymbol{X}(\boldsymbol{x}(t),\sigma)d\sigma, \left[\int_0^t \boldsymbol{X}(\boldsymbol{x}(t),\sigma)d\sigma,\ \boldsymbol{X}(\boldsymbol{x}(t),t)\right]\right] dt,
\end{aligned}
\tag{2.18}
$$

where the Lie bracket between two vector fields is defined as $[\boldsymbol{V}_1(\boldsymbol{x}), \boldsymbol{V}_2(\boldsymbol{x})] = \frac{\partial \boldsymbol{V}_2}{\partial \boldsymbol{x}}\boldsymbol{V}_1 - \frac{\partial \boldsymbol{V}_1}{\partial \boldsymbol{x}}\boldsymbol{V}_2$. Sarychev and Vela showed that if the series (2.17) converges, its limit will be the logarithm of the Monodromy map (i.e., the nonlinear vector-valued function that maps an initial condition to the solution after the period T). That is, if the complete averaged dynamics (2.17) has an exponentially stable fixed point, then the NLTP system (2.9) will have an exponentially stable periodic orbit, irrespective of the value of ϵ.

Based on the above discussion, it is implied that if ϵ is small enough to truncate the series after the first term, $\boldsymbol{\Lambda}_1$, the first-order averaging theorem is recovered. If not, then one should use higher-order averaging until the desired accuracy is met. However, only convergence of the series (2.17) representing the complete averaged dynamics is guaranteed under some conditions [23]. Therefore, since the series (2.17) is typically not asymptotic, practical computation may be an issue as one may need to perform infeasibly high-order averaging to truncate the convergent series with a good accuracy, as shown by Nayfeh [51].

Chapter 3

Differential-Geometric-Control Formulation, Nonlinear Controllability, and Motion Planning of Airplane Flight Dynamics

Linear controllability conditions for linearized systems are not necessary. That is, there exists a class of nonlinear systems that are linearly uncontrollable but nonlinearly controllable. Differential-geometric control theory provides useful tools for analyzing nonlinear controllability of dynamical systems. In particular, it allows for identification of the ability to generate motions along unactuated (nonintuitive) directions through specific interactions between the system dynamics and control inputs. Thus, nonlinear controllability analysis of airplane flight dynamics reveals many unconventional methods to generate motion along different directions in the state space. These unconventional methods rely on the concept of *Lie bracket* control action, which is manipulating two (or more) different control inputs to steer the system along a direction that is not directly actuated by any of these inputs. Implementing these unconventional motion generation mechanisms requires tools from nonlinear motion planning literature.

In this effort, the six degrees-of-freedom, rigid-airplane, nonlinear equations of motion are considered and cast in a differential-geometric-control framework, where different interconnections between the airplane configuration and controllability are assessed. Consequently, new unconventional rolling/yawing and pitching mechanisms that could be exploited near stall are identified. An investigation of the new roll mechanism proves it to be superior to the conventional one (direct aileron input) near stall, where the aileron sensitivity degrades. Finally, a thrust-only flight control system is analyzed in this framework.

3.1 Introduction

One of the indispensable problems of a control engineer is the controllability question. Controllability is a question about the ability to steer the system from a given initial point to a given final point in finite time (i.e., it is an existence question; existence of a steering control input history). For linear systems, this question has been answered from almost half a century by Kalman, Ho, and Narendra [13]. The Kalman controllability rank condition is instrumental in the modern control theory. It is necessary, sufficient, and very simple to use. Moreover, for a nonlinear system, linearization about a given initial point may be used to study *local* controllability about that point. That is, if the linearized system is controllable from $\boldsymbol{x}_0$, the nonlinear system is locally controllable from $\boldsymbol{x}_0$ as well. However, controllability of the linearized system is not necessary. That is, there exists a class of systems that are linearly uncontrollable, yet nonlinearly controllable.

The situations where nonlinear controllability is invoked are usually associated with the ability to generate motions along unactuated directions (directions over which direct control authority is missed). An interesting typical example that illustrates this situation is the kinematic car. A car with two controls (forward/backward and steering) is obviously not linearly controllable because of the inability to generate pure side motions. However, nonlinear geometric analysis shows that the system is nonlinearly controllable and through some manipulation of the available two controls, one can generate side motions. This idea can be generalized to many nonlinear dynamical control systems, where the question is "Will the system remain controllable, if one or more actuators are lost?" One example is the attitude dynamics of a spacecraft (rigid body) where it has been shown that the system remains controllable even if one or two pairs of gas jets are removed [14], in spite of the system being linearly uncontrollable. Also, this question has been addressed previously by the authors for airplane flight dynamics using a linear controllability analysis [52]. Therefore, the focus of this chapter is to address this question from a geometric-nonlinear-analysis approach.

Although the theory of geometric nonlinear controllability has been well developed [36], very little has been done to apply it to airplane flight dynamics. This may be attributed to the fact that airplane flight dynamics is, indeed, controllable and the linear analysis is quite sufficient. It is interesting to know that, even if a multi-engine airplane lost all of its control surfaces due to a failure in the hydraulic system for example, linear analysis would still be sufficient to prove controllability of the dynamic states (i.e., 9×9 system excluding the navigation states) [52]. That is, conventional airplanes are equipped with so redundant control authority that nonlinear controllability analysis may not be needed. However, for unmanned air vehicles (with their numerous potential applications), this redundancy in control authority will be questioned and may be sacrificed for better performance and cheaper operation. In addition, the aeronautical engineering community is steadily seeking unconventional more efficient configurations for airplanes. Obviously, relaxing controllability requirements will broaden the design space for future airplane configuration. On the other hand, while the flight dynamics of conventional airplanes suffer no controllability issues during normal operation, it may do when the airplane encounters undesirable flight conditions (e.g., near stall). It is well known that the aerodynamic control effectiveness reduces considerably near stall and also near the control reversal boundary at high flight speeds. The above reasons invoke a nonlinear controllability analysis for airplane flight dynamics.

Utilizing the quite rich airplane nonlinear flight dynamics reveals unconventional ways to control/steer the airplane. As such, the nonlinear controllability analysis performed in this chapter unveils an unconventional roll/yaw mechanism that relies on the interaction between elevator and aileron control inputs. The unconventional roll/yaw mechanism is shown to have the potential of higher roll control authority over the conventional one (direct aileron input) at near-stall operating points. It is well-known that aileron sensitivity degrades at high angles of attack (i.e., near stall), hence a degradation in the conventional roll mechanism, which may lead to loss of roll control. According to [53], stall accounts for about 46% of loss of control events in commercial aircraft. A new roll/yaw mechanism that has a higher control authority than the conventional one at such a critical operating point could potentially help mitigate some loss of control incidents. In order to further investigate this new roll/yaw mechanism, two important questions should be answered: (i) how strong/weak is that mechanism?; and (ii) how to execute it? The first question relates to the degree of nonlinear controllability, whereas the second one is essentially a nonlinear motion planning question. In this effort, we focus on answering the second question, yet we discuss some aspects related to the first one.

It should be noted that the analysis in this effort assumes unbounded control inputs. Had the control inputs been bounded, the yes/no answer to the controllability question would not have changed, yet the optimal steering control that makes a certain cost function extremum would change. For more details about feedback control design of linear systems with control constraints, the reader is refereed to the article by Sontag and Sussmann [54] and the references therein. Also, for formulating the dynamic equations of a nonlinear system with control constraints, the reader is refereed to the articles by Blajer et al. [55], [56], Fumagalli et al. [57], and Masarati et al. [58].

In this chapter, the six degrees-of-freedom (DOF) equations of motion governing the rigid-airplane nonlinear flight dynamics are considered. The constructed nonlinear model is validated against simulation results from open literature. This model is then represented in a differential-geometric-control framework, where nonlinear controllability is assessed. The analysis is used to determine the aerodynamic characteristics that are responsible for nonlinear controllability of airplanes. Consequently, new unconventional rolling/yawing and pitching mechanisms are identified. A detailed investigation of the new roll mechanism is performed as it shows a potential advantage over the conventional one (direct aileron input) near stall. The new roll mechanism is found to be superior to the conventional one at near-stall operating points, as the aileron sensitivity degrades. Tools from nonlinear motion planning literature are then employed to execute near-stall roll maneuvers through the new roll mechanism. Finally, a thrust-only flight control system, that lacks linear controllability, is analyzed in this framework and shown to be nonlinearly controllable.

3.2 Rigid Airplane Nonlinear, Six DOF Flight Dynamics Model

3.2.1 Equations of Motion

The six DOF equations of motion governing flight dynamics of rigid airplanes can be written as follows [59]

Force Equations

$$
\begin{aligned}
\dot{U} &= RV - QW - g\sin\theta + \tfrac{F_X}{m} \\
\dot{V} &= -RU + PW + g\sin\phi\cos\theta + \tfrac{F_Y}{m} \\
\dot{W} &= QU - PV + g\cos\phi\cos\theta + \tfrac{F_Z}{m}
\end{aligned}
\tag{3.1}
$$

where U, V, and W are the velocity components in the body frame, P, Q, and R are the angular velocity components in the body frame, ϕ, θ, and ψ are the Euler angles defining body frame with respect to an inertial frame, g is the gravitational acceleration, m is the aircraft mass, and F_X, F_Y, and F_Z are the components of the aerodynamic force vector in the body frame.

Moment Equations

$$
\begin{aligned}
\dot{P} &= (C_1R + C_2P)Q + C_3\mathcal{L} + C_4N \\
\dot{Q} &= C_5PR - C_6(P^2 - R^2) + C_7M \\
\dot{R} &= (C_8P - C_2R)Q + C_4\mathcal{L} + C_9N
\end{aligned}
\tag{3.2}
$$

where $C_1 = \frac{(J_Y - J_Z)J_Z - J_{XZ}^2}{\Gamma}$, $C_2 = \frac{(J_X - J_Y + J_Z)J_{XZ}}{\Gamma}$, $C_3 = \frac{J_Z}{\Gamma}$, $C_4 = \frac{J_{XZ}}{\Gamma}$, $C_5 = \frac{J_Z - J_X}{J_Y}$, $C_6 = \frac{J_{Xz}}{J_Y}$, $C_7 = \frac{1}{J_Y}$, $C_8 = \frac{(J_X - J_Y)J_X + J_{XZ}^2}{\Gamma}$, $C_9 = \frac{J_X}{\Gamma}$, $\Gamma = J_XJ_Z - J_{XZ}^2$, and J_X, J_Y, J_Z, and J_{XZ} are the components of the inertia matrix in the body frame. Also, $\mathcal{L}, M$, and N are the components of the aerodynamic moment vector in the body frame.

Kinematic Equations

$$
\begin{aligned}
\dot{\phi} &= P + \tan\theta(Q\sin\phi + R\cos\phi) \\
\dot{\theta} &= Q\cos\phi - R\sin\phi \\
\dot{\psi} &= \tfrac{Q\sin\phi + R\cos\phi}{\cos\theta}
\end{aligned}
\tag{3.3}
$$

Navigation Equations

$$\begin{aligned}
\dot{P}_N &= U\cos\theta\cos\psi + V(-\cos\phi\sin\psi + \sin\phi\sin\theta\cos\psi) \\
&+ W(\sin\phi\sin\psi + \cos\phi\sin\theta\cos\psi) \\
\dot{P}_E &= U\cos\theta\sin\psi + V(\cos\phi\cos\psi + \sin\phi\sin\theta\sin\psi) \\
&+ W(-\sin\phi\cos\psi + \cos\phi\sin\theta\sin\psi) \\
\dot{h} &= U\sin\theta - V\sin\phi\cos\theta - W\cos\phi\cos\theta
\end{aligned} \tag{3.4}$$

where P_E and P_N are the position coordinates in the east and north directions, respectively, in the inertial frame of reference, and h is the altitude.

The applied forces and moments can be classified into aerodynamic and thrust contributions. That is, a generalized force G can be written as $G = G_A + G_T$, where the subscript A denotes aerodynamic contributions, and the subscript T denotes thrust contributions. The thrust contributions are written as $G_T = G_{T_0} + G_{\delta_t}\delta_t$, where G_{T_0} represents the trim value and G_{δ_t} represents the sensitivity of the generalized force G with respect to the throttle deflection δ_t. The aerodynamic forces and moments are related to the aerodynamic coefficients through: $F_i = qSC_i$, $\mathcal{L} = qSbC_{\mathcal{L}}$, $M = qS\bar{c}C_M$, and $N = qSbC_N$, where q is the dynamic pressure, S is the wing area, $\bar{c}$ is the mean aerodynamic chord, and b is the wing span.

3.2.2 Representation of Aerodynamic Loads

In order to exploit the powerful tools of geometric nonlinear control, we need to make room for aerodynamic nonlinearities . As such, we followed Stevens and Lewis [59] and wrote

$$
\begin{aligned}
C_X &= C_X(\alpha) + (\tfrac{\bar{c}}{2V_T})C_{X_Q}(\alpha)Q + C_{X_{\delta_e}}(\alpha)\delta_e \\
C_Y &= C_Y(\beta) + \left(\tfrac{b}{2V_T}\right)(C_{Y_R}(\alpha)R + C_{Y_P}(\alpha)P) + C_{Y_{\delta_a}}(\beta)\delta_a + C_{Y_{\delta_r}}(\beta)\delta_r \\
C_Z &= C_Z(\alpha) + \left(\tfrac{\bar{c}}{2V_T}\right)C_{Z_Q}(\alpha)Q + C_{Z_{\delta_e}}(\alpha)\delta_e \\
C_{\mathcal{L}} &= C_{\mathcal{L}}(\alpha,\beta) + \left(\tfrac{b}{2V_T}\right)(C_{\mathcal{L}_R}(\alpha)R + C_{\mathcal{L}_P}(\alpha)P) + C_{\mathcal{L}_{\delta_a}}(\alpha,\beta)\delta_a + \\
&+ C_{\mathcal{L}_{\delta_r}}(\alpha,\beta)\delta_r \\
C_M &= C_M(\alpha) + \left(\tfrac{\bar{c}}{2V_T}\right)C_{M_Q}(\alpha)Q + C_{M_{\delta_e}}(\alpha)\delta_e \\
C_N &= C_N(\alpha,\beta) + \left(\tfrac{b}{2V_T}\right)(C_{N_R}(\alpha)R + C_{N_P}(\alpha)P) + C_{N_{\delta_a}}(\alpha,\beta)\delta_a + \\
&+ C_{N_{\delta_r}}(\alpha,\beta)\delta_r
\end{aligned}
\tag{3.5}
$$

where V_T is the true airspeed, i.e., $V_T = \sqrt{U^2 + V^2 + W^2}$, α is the angle of attack, β is the side slip angle, and $\delta_e, \delta_a, \delta_r$, and δ_t are the elevator, aileron, rudder, and throttle deflections respectively.

3.3 Nonlinear Model Validation

To validate the 6 DOF nonlinear flight dynamic model described in Sec. 3.2, we simulate the same flight conditions considered by Taha [1] and compare with his results. Taha considered the DELTA (a paradigm model for a very large, four-engined, cargo jet aircraft) and the FOXTROT (a paradigm model for a twin- engined, jet fighter/bomber aircraft) airplane models whose stability derivatives are obtained from McLean [60]. It should be noted that for the sake of comparison with Taha's results, the aerodynamic forces and moments are represented linearly in this section through the listed stability derivatives in McLean [60].

Figure 3.1 shows the obtained response due to $-10°$ elevator step input for the DELTA model at the flight condition (Mach no.=0.875, altitude=$12,200\ m$, U_0=$260\ m/s$, α_0=$4.9°$) compared with the results of Taha [1]. Figure 3.2 shows the obtained response due to $1°$ aileron step input for the FOXTROT model at the flight condition (Mach no.=2.15, altitude=$13,700\ m$, U_0=$650\ m/s$, α_0=$1.4°$) compared with Taha's results [1]. The comparison shown in Figs. 3.1 and 3.2 validates our implementation of the model described in Sec. 3.2.

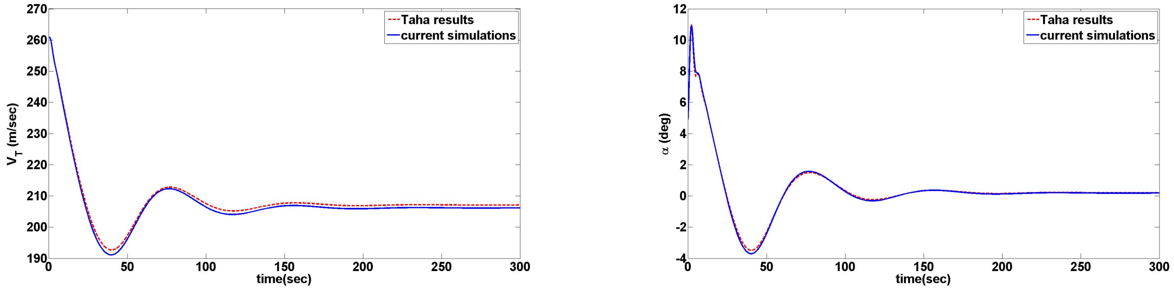

(a) Airplane speed (b) Angle of attack

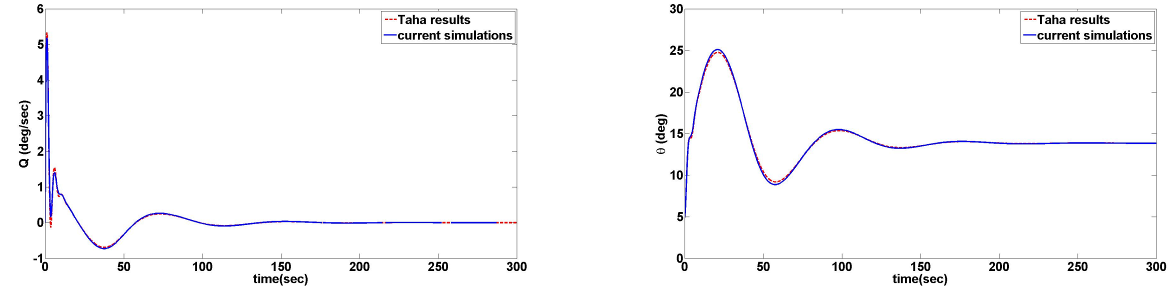

(c) Pitch rate (d) pitch angle

Figure 3.1: Airplane response due to $-10°$ elevator step input from the current simulations and Taha's results [1].

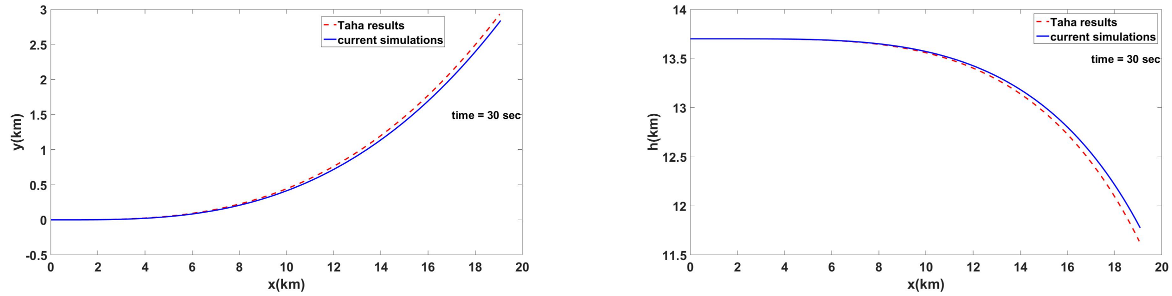

(a) Horizontal-plane trajectory (b) Vertical-plane trajectory

Figure 3.2: Airplane response due to 1° aileron step input from the current simulations and Taha's results [1].

3.4 Geometric Control Formulation of Airplane Flight Dynamics

The nonlinear model describing rigid-airplane flight dynamics, discussed in Sec. 3.2, can be written in the form (2.2) with $\boldsymbol{x} = [U \quad V \quad W \quad P \quad Q \quad R \quad \phi \quad \theta \quad \psi]^\mathsf{T}$ and $\boldsymbol{u} = [\delta_e \quad \delta_a \quad \delta_r \quad \delta_t]^\mathsf{T}$, where the superscript T denotes transpose. Here, we omit the navigation states, as they do not affect stability and control (i.e., ignorable coordinates). After rearranging the equations of motion, we obtain the drift vector field $\boldsymbol{f}(\boldsymbol{x})$, which includes the uncontrolled aerodynamic loads, and the control input vector fields $\boldsymbol{g}_i$'s associated with the four control inputs

$\delta_e, \delta_a, \delta_r,$ and δ_t.

$$
\boldsymbol{f}(\boldsymbol{x}) = \begin{bmatrix}
RV - QW - g\sin\theta + \frac{qS\bar{c}QC_{X_Q}(\alpha)}{2mV_T} + \frac{qSC_X(\alpha)}{m} + \frac{X_{T_0}}{m} \\[2ex]
-RU + PW + g\sin\phi\cos\theta + \frac{qS}{m}C_Y(\beta) + \frac{qSbP}{2mV_T}C_{Y_p}(\alpha) + \frac{qSbR}{2mV_T}C_{Y_r}(\alpha) \\[2ex]
QU - PV + g\cos\phi\cos\theta + \frac{qS\bar{c}QC_{Z_Q}(\alpha)}{2mV_T} + \frac{qSC_Z(\alpha)}{m} + + \frac{Z_{T_0}}{m} \\[2ex]
Q(C_1R + C_2P) + C_3\left(qSbC_{\mathcal{L}}(\alpha,\beta) + \frac{qSbP}{2V_T}C_{\mathcal{L}_P}(\alpha) + \frac{qSbR}{2V_T}C_{\mathcal{L}_R}(\alpha)\right) \\
+C_4\left(qSbC_N(\alpha,\beta) + \frac{qSbP}{2V_T}C_{N_P}(\alpha) + \frac{qSbR}{2V_T}C_{N_R}(\alpha)\right) \\[2ex]
C_5PR - C_6\left(P^2 - R^2\right) + C_7\left(qS\bar{c}C_M(\alpha) + \frac{qS\bar{c}Q}{2V_T}C_{M_Q}(\alpha) + M_{T_0}\right) \\[2ex]
Q(C_8P - C_2R) + C_4\left(qSbC_{\mathcal{L}}(\alpha,\beta) + \frac{qSbPC_{\mathcal{L}_P}(\alpha)}{2V_T} + \frac{qSbRC_{\mathcal{L}_R}(\alpha)}{2V_T}\right) \\
+C_9\left(qSbC_N(\alpha,\beta) + \frac{qSbPC_{N_P}(\alpha)}{2V_T} + \frac{qSbRC_{N_R}(\alpha)}{2V_T}\right) \\[2ex]
P + \tan\theta(Q\sin\phi + R\cos\phi) \\[2ex]
Q\cos\phi - R\sin\phi \\[2ex]
\sec\theta(Q\sin\phi + R\cos\phi)
\end{bmatrix} \tag{3.6}
$$

$$\boldsymbol{g}_{\delta_e} = \begin{bmatrix} \frac{qSC_{X_{\delta_e}}(\alpha)}{m} \\ 0 \\ \frac{qSC_{Z_{\delta_e}}(\alpha)}{m} \\ 0 \\ C_7 qS\bar{c}C_{M_{\delta_e}}(\alpha) \\ 0 \\ 0 \\ 0 \\ 0 \end{bmatrix} \quad (3.7) \qquad \boldsymbol{g}_{\delta_a} = \begin{bmatrix} 0 \\ \frac{qSC_{Y_{\delta_a}}(\beta)}{m} \\ 0 \\ qSb\left(C_3 C_{\mathcal{L}_{\delta_a}}(\alpha,\beta) + C_4 C_{N_{\delta_a}}(\alpha,\beta)\right) \\ 0 \\ qSb\left(C_4 C_{\mathcal{L}_{\delta_a}}(\alpha,\beta) + C_9 C_{N_{\delta_a}}(\alpha,\beta)\right) \\ 0 \\ 0 \\ 0 \end{bmatrix} \quad (3.8)$$

$$\boldsymbol{g}_{\delta_r} = \begin{bmatrix} 0 \\ \frac{qSC_{Y_{\delta_r}}(\beta)}{m} \\ 0 \\ qSb\left(C_3 C_{\mathcal{L}_{\delta_r}}(\alpha,\beta) + C_4 C_{N_{\delta_r}}(\alpha,\beta)\right) \\ 0 \\ qSb\left(C_4 C_{\mathcal{L}_{\delta_r}}(\alpha,\beta) + C_9 C_{N_{\delta_r}}(\alpha,\beta)\right) \\ 0 \\ 0 \\ 0 \end{bmatrix} \quad (3.9) \qquad \boldsymbol{g}_{\delta_t} = \begin{bmatrix} \frac{X_{\delta_t}}{m} \\ 0 \\ \frac{Z_{\delta_t}}{m} \\ 0 \\ C_7 M_{\delta_t} \\ 0 \\ 0 \\ 0 \\ 0 \end{bmatrix} \quad (3.10)$$

Since the controllability analysis (linear and nonlinear) for nonlinear systems is essentially local, we perform such an analysis at a point of interest. In this work, nonlinear controllability analysis only at the cruise flight condition will be performed.

3.4.1 Trim (Balance)

For steady level cruising flight, the airplane is flying with constant speed and certain angle of attack. To ensure equilibrium at such a flight condition, we set

$$\dot{U} = \dot{V} = \dot{W} = \dot{P} = \dot{Q} = \dot{R} = \dot{\phi} = \dot{\theta} = \dot{\psi} = 0 \tag{3.11}$$

and

$$U = U_0, \quad V = 0, \quad W = W_0, \quad P = 0, \quad Q = 0, \quad R = 0, \quad \phi = 0, \quad \theta = \alpha_o, \quad \psi = 0 \tag{3.12}$$

substituting Eqs. (3.11) and (3.12) in the equations of motion (3.1)–(3.3) we obtain

$$\begin{aligned} \tfrac{X_{T_0}}{m} + \tfrac{qSC_X(\alpha_o)}{m} - g\sin\alpha_o &= 0 \\ C_Y(\beta_o) &= 0 \\ \tfrac{Z_{T_0}}{m} + \tfrac{qSC_Z(\alpha_o)}{m} + g\cos\alpha_o &= 0 \\ C_{\mathcal{L}}(\alpha_o, \beta_o) &= 0 \\ qS\bar{c}C_M(\alpha_o) - M_{T_0} &= 0 \\ C_N(\alpha_o, \beta_o) &= 0 \end{aligned} \tag{3.13}$$

which represent the trim condition at cruise.

3.4.2 Unconventional Motion Generation Mechanisms

The first-order Lie brackets between the vector fields $\boldsymbol{f}$ and $\boldsymbol{g}_i$'s at the cruise flight condition are calculated and shown in Appendix A. In this subsection, we discuss some of the interesting results based on studying those Lie brackets.

Airplane Configuration and Controllability

It should be noted that the obtained Lie brackets provide feasible directions for motion generation. For example, the Lie bracket vector field $[\boldsymbol{f}, \boldsymbol{g}_{\delta_e}]$, shown in Eq. (3.14), represents the possible motions due to the interaction between system dynamics and the elevator deflection. Inspecting the Lie bracket vector field $[\boldsymbol{f}, \boldsymbol{g}_{\delta_e}]$, we find non-zero components in the fourth and sixth elements, which correspond to rolling and yawing accelerations, respectively. Although, this result may be found using linear analysis, it is not commonly known that elevator can produce rolling and yawing from a symmetric cruise flight condition if the airplane configuration leads to non-zero values for $\frac{\partial C_{\mathcal{L}}(\alpha,\beta)}{\partial \alpha}$ or $\frac{\partial C_{N}(\alpha,\beta)}{\partial \alpha}$. It should be noted that the former is non-zero for the F-4B aircraft, though of a small magnitude [59, P. 90]. Moreover, for fighter airplanes doing maneuvers at transonic speeds, the asymmetry in the shock wave development over the two wings will induce non-zero values for these aerodynamic derivatives even at symmetric flight conditions. The wing drop phenomenon in the

F/A-18 is a typical example [61].

$$\left[\boldsymbol{f},\boldsymbol{g}_{\delta_e}\right]=\begin{bmatrix}
\begin{gathered}\frac{q^2S^2W_0C_{X_{\delta_e}}(\alpha)C_X{}'(\alpha)}{m^2U_0^2\left(\frac{W_0^2}{U_0^2}+1\right)}-\frac{q^2S^2C_{Z_{\delta_e}}(\alpha)C_X{}'(\alpha)}{m^2U_0\left(\frac{W_0^2}{U_0^2}+1\right)}+\\
-C_7qS\bar{c}C_{M_{\delta_e}}(\alpha)\left(\frac{qS\bar{c}C_{X_Q}(\alpha)}{2m\sqrt{U_0^2+W_0^2}}-W_0\right)\end{gathered}\\[2em]
0\\[2em]
\begin{gathered}\frac{q^2S^2W_0C_{X_{\delta_e}}(\alpha)C_Z{}'(\alpha)}{m^2U_0^2\left(\frac{W_0^2}{U_0^2}+1\right)}-\frac{q^2S^2C_{Z_{\delta_e}}(\alpha)C_Z{}'(\alpha)}{m^2U_0\left(\frac{W_0^2}{U_0^2}+1\right)}+\\
-C_7\bar{c}qSC_{M_{\delta_e}}(\alpha)\left(U_0+\frac{qS\bar{c}C_{Z_Q}(\alpha)}{2m\sqrt{U_0^2+W_0^2}}\right)\end{gathered}\\[2em]
\begin{gathered}-\frac{qSC_{Z_{\delta_e}}(\alpha)}{m}\left(\frac{C_3qSb\frac{\partial C_{\mathcal{L}}(\alpha,\beta)}{\partial\alpha}}{U_0\left(\frac{W_0^2}{U_0^2}+1\right)}+\frac{C_4qSb\frac{\partial C_N(\alpha,\beta)}{\partial\alpha}}{U_0\left(\frac{W_0^2}{U_0^2}+1\right)}\right)+\\
-\frac{qSC_{X_{\delta_e}}(\alpha)}{m}\left(-\frac{C_3qSbW_0\frac{\partial C_{\mathcal{L}}(\alpha,\beta)}{\partial\alpha}}{U_0^2\left(\frac{W_0^2}{U_0^2}+1\right)}-\frac{C_4qSbW_0\frac{\partial C_N(\alpha,\beta)}{\partial\alpha}}{U_0^2\left(\frac{W_0^2}{U_0^2}+1\right)}\right)\end{gathered}\\[2em]
\begin{gathered}\frac{C_7q^2S^2\bar{c}W_0C_{X_{\delta_e}}(\alpha)C_M'(\alpha)}{mU_0^2\left(\frac{W_0^2}{U_0^2}+1\right)}-\frac{C_7^2q^2S^2\bar{c}^2C_{M_{\delta_e}}(\alpha)C_{M_Q}(\alpha)}{2\sqrt{U_0^2+W_0^2}}+\\
-\frac{C_7q^2S^2\bar{c}C_{Z_{\delta_e}}(\alpha)C_M'(\alpha)}{mU_0\left(\frac{W_0^2}{U_0^2}+1\right)}\end{gathered}\\[2em]
\begin{gathered}-\frac{qSC_{Z_{\delta_e}}(\alpha)}{m}\left(\frac{C_4qSb\frac{\partial C_{\mathcal{L}}(\alpha,\beta)}{\partial\alpha}}{U_0\left(\frac{W_0^2}{U_0^2}+1\right)}+\frac{C_9qSb\frac{\partial C_N(\alpha,\beta)}{\partial\alpha}}{U_0\left(\frac{W_0^2}{U_0^2}+1\right)}\right)+\\
-\frac{qSC_{X_{\delta_e}}(\alpha)}{m}\left(-\frac{C_4qSbW_0\frac{\partial C_{\mathcal{L}}(\alpha,\beta)}{\partial\alpha}}{U_0^2\left(\frac{W_0^2}{U_0^2}+1\right)}-\frac{C_9qSbW_0\frac{\partial C_N(\alpha,\beta)}{\partial\alpha}}{U_0^2\left(\frac{W_0^2}{U_0^2}+1\right)}\right)\end{gathered}\\[2em]
0\\[2em]
-C_7qS\bar{c}C_{M_{\delta_e}}(\alpha)\\[2em]
0
\end{bmatrix}\tag{3.14}$$

A similar observation is found in the Lie bracket vector field $[\boldsymbol{f}, \boldsymbol{g}_{\delta_t}]$ (Eq. (A.4) in Appendix A) which represents interaction between throttle input and airplane flight dynamics. Non-zero contributions for roll and yaw can be obtained if $\frac{\partial C_{\mathcal{L}}(\alpha,\beta)}{\partial \alpha}$ or $\frac{\partial C_N(\alpha,\beta)}{\partial \alpha}$ is non-zero at cruise. It should be noted that differential thrust is not introduced here. That is, the above observation is for a symmetric thrust configuration (e.g., single-engine). Along with the fact that throttle input naturally creates pitching, the above observation may lead to design of a thrust-only flight control system (TFCS) to be used in emergency cases such as failure in the hydraulic system. Yamasaki et al. [62] exploited the engine layout of the Boeing 747-400 to design a thrust-only flight control system relying on differential thrust and multi elevations for the engines. Also, the same system has been investigated in the 1990s by Burcham et al. [63, 64] and Tucker [65] at NASA Dryden Flight Research Center, they called it propulsion controlled aircraft (PCA). They developed a computer-assisted engine control system, implemented and tested it on the F-15 fighter aircraft and the MD-11 transport aircraft.

New Rolling/Yawing and Pitching Mechanisms

Inspecting the Lie bracket vector $[\boldsymbol{g}_{\delta_e}, \boldsymbol{g}_{\delta_a}]$ (interaction between elevator and aileron), shown in Eq. (3.15), new rolling and yawing mechanism is observed. That is, steady state rolling can be obtained by *zero-mean* oscillating aileron and elevator deflections, provided that $\frac{\partial C_{\mathcal{L}_{\delta_a}}}{\partial \alpha}$ or $\frac{\partial C_{N_{\delta_a}}}{\partial \alpha}$ is nonzero. It should be noted that a Lie bracket vector field $[\boldsymbol{g}_{\delta_i}, \boldsymbol{g}_{\delta_j}]$ between two input vector fields $\boldsymbol{g}_{\delta_i}$ and $\boldsymbol{g}_{\delta_j}$ can be realized by an out-of-phase square waves or sinusoids for the associated control inputs [31]. Therefore, if $\frac{\partial C_{\mathcal{L}_{\delta_a}}}{\partial \alpha} \neq 0$ or $\frac{\partial C_{N_{\delta_a}}}{\partial \alpha} \neq 0$, steady-state rolling can be obtained by out-of-phase oscillation of aileron and elevator [66]. Similarly, inspecting the Lie bracket vector field $[\boldsymbol{g}_{\delta_e}, \boldsymbol{g}_{\delta_t}]$ (interaction between elevator and throttle), Eq. (A.7) in Appendix A, a new pitching mechanism is observed. That is, a steady state pitching can be obtained by zero-mean oscillating elevator and throttle deflections provided that there is a non-zero value for the derivative $C'_{M_{\delta_e}}$.

$$\left[\boldsymbol{g}_{\delta_e}, \boldsymbol{g}_{\delta_a}\right] = \begin{bmatrix} 0 \\ 0 \\ 0 \\ \begin{gathered} \frac{q^2 S^2 b\ C_{X_{\delta_e}}(\alpha)}{m}\left(-\frac{C_3 W_0 \frac{\partial C_{\mathcal{L}_{\delta_a}}(\alpha,\beta)}{\partial \alpha}}{U_0^2\left(\frac{W_0^2}{U_0^2}+1\right)} - \frac{C_4 W_0 \frac{\partial C_{N_{\delta_a}}(\alpha,\beta)}{\partial \alpha}}{U_0^2\left(\frac{W_0^2}{U_0^2}+1\right)}\right)+ \\ +\frac{q^2 S^2 b\ C_{Z_{\delta_e}}(\alpha)}{m}\left(\frac{C_3 \frac{\partial C_{\mathcal{L}_{\delta_a}}(\alpha,\beta)}{\partial \alpha}}{U_0\left(\frac{W_0^2}{U_0^2}+1\right)} + \frac{C_4 \frac{\partial C_{N_{\delta_a}}(\alpha,\beta)}{\partial \alpha}}{U_0\left(\frac{W_0^2}{U_0^2}+1\right)}\right) \end{gathered} \\ 0 \\ \begin{gathered} \frac{q^2 S^2 b\ C_{X_{\delta_e}}(\alpha)}{m}\left(-\frac{C_4 W_0 \frac{\partial C_{\mathcal{L}_{\delta_a}}(\alpha,\beta)}{\partial \alpha}}{U_0^2\left(\frac{W_0^2}{U_0^2}+1\right)} - \frac{C_9 W_0 \frac{\partial C_{N_{\delta_a}}(\alpha,\beta)}{\partial \alpha}}{U_0^2\left(\frac{W_0^2}{U_0^2}+1\right)}\right)+ \\ +\frac{q^2 S^2 b\ C_{Z_{\delta_e}}(\alpha)}{m}\left(\frac{C_4 \frac{\partial C_{\mathcal{L}_{\delta_a}}(\alpha,\beta)}{\partial \alpha}}{U_0\left(\frac{W_0^2}{U_0^2}+1\right)} + \frac{C_9 \frac{\partial C_{N_{\delta_a}}(\alpha,\beta)}{\partial \alpha}}{U_0\left(\frac{W_0^2}{U_0^2}+1\right)}\right) \end{gathered} \\ 0 \\ 0 \\ 0 \end{bmatrix} \tag{3.15}$$

To inspect the efficacy of the observed new rolling and pitching mechanisms, we write the potential flow lift without leading edge suction as

$$C_L = C_{L_\alpha} \sin\alpha \cos^2\alpha$$

where C_{L_α} is the lift curve slope in the linear range [67, 68, 69]. As such, we have

$$\frac{dC_L}{d\alpha} = C_{L_\alpha} \cos\alpha(\cos^2\alpha - 2\sin^2\alpha)$$

Therefore, since $C_{\mathcal{L}_{\delta_a}}(\alpha)$ and $C_{M_{\delta_e}}(\alpha)$ are linearly dependent on $\frac{dC_L}{d\alpha}$, we can represent $C_{\mathcal{L}_{\delta_a}}(\alpha)$ and $C_{M_{\delta_e}}(\alpha)$ as follows

$$\begin{aligned} C_{\mathcal{L}_{\delta_a}}(\alpha) &= C_{\mathcal{L}_{\delta_{a0}}} \cos\alpha(\cos^2\alpha - 2\sin^2\alpha) \\ C_{M_{\delta_e}}(\alpha) &= C_{M_{\delta_{e0}}} \cos\alpha(\cos^2\alpha - 2\sin^2\alpha) \end{aligned} \tag{3.16}$$

where $C_{\mathcal{L}_{\delta_{a0}}}$ and $C_{M_{\delta_{e0}}}$ are the aileron and elevator sensitivities, respectively, in the linear range. Figure 3.3 shows the variation of the aileron and elevator sensitivities with angle of attack. As may be expected, they both decrease as the angle of attack increases towards stall. However, the derivatives $\frac{\partial \mathcal{L}_{\delta_a}(\alpha)}{\partial \alpha}$ and $\frac{dC_{M_{\delta_e}}}{d\alpha}$, which represent the sensitivities of the new rolling and pitching mechanisms, respectively, have considerable values. As such, the new rolling and pitching mechanisms may be suitable in high angle of attack situations (e.g., stall recovery). It should be noted that this is a novel nonlinear mechanism that is not related to Crouch's theorem [14]; the latter is concerned with single input.

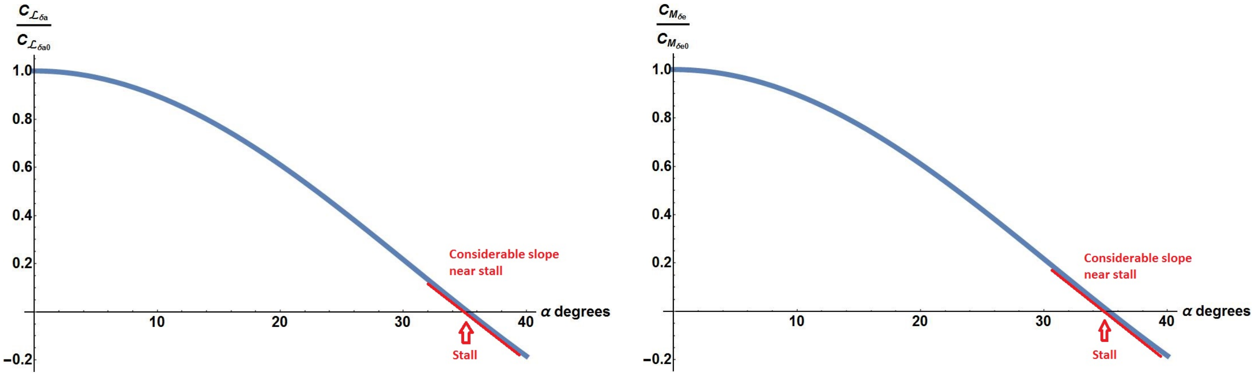

(a) Normalized $C_{\mathcal{L}_{\delta_a}}$

(b) Normalized $C_{M_{\delta_e}}$

Figure 3.3: Variation of $C_{\mathcal{L}_{\delta_a}}$ and $C_{M_{\delta_e}}$ with α.

3.5 Investigation of the Novel Roll Mechanism

In this section, the newly discovered roll mechanism (3.15), hereafter denoted by Lie roll mechanism (LRM), is thoroughly investigated near stall; where it has a potential to be more effective than the conventional one (direct aileron input). As explained earlier in Sec. 3.4.2, the conventional roll mechanism's sensitivity, $C_{\mathcal{L}_{\delta_a}}$, degrades near stall. However, the Lie roll mechanism's sensitivity is characterized by the rate of change of the aileron sensitivity with the angle of attack, i.e., $\frac{\partial \mathcal{L}_{\delta_a}(\alpha)}{\partial \alpha}$, which possesses a considerable value near stall. Figure 3.4 elaborates on this point by showing the variation of the normalized aileron sensitivity (i.e., $\frac{C_{\mathcal{L}_{\delta_a}}}{C_{\mathcal{L}_{\delta_{a0}}}}$) with angle of attack, adapted to the NASA generic transport model (GTM) [70, 71].

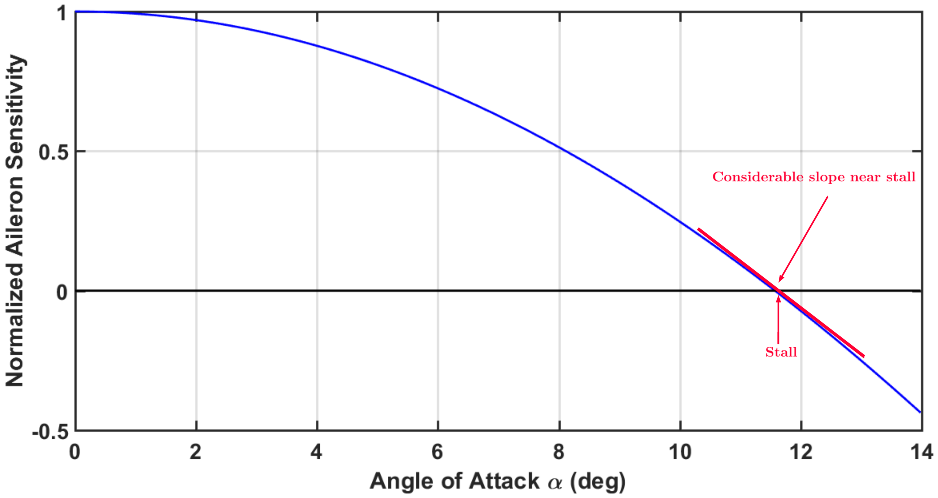

Figure 3.4: Variation of the normalized $C_{\mathcal{L}_{\delta_a}}$ with α.

Since the LRM is essentially a nonlinear motion generation mechanism, the nonlinear motion planning tools, reviewed in Sec. 2.1 are employed. A reduced-order three DOF flight dynamics model is then developed to examine roll control power of the LRM versus the conventional one. Afterwards, Fliess functional expansion for the roll output is performed to investigate the different contributing factors to this output. A comparison through Fliess functional expansion and numerical simulation is then held to examine the maximum capabilities of both the LRM and conventional roll mechanisms near stall, where the aileron sensitivity degrades. An agreement is found between both Fliess functional expansion and numerical simulation that the LRM mechanism is superior to the conventional one near stall. Moreover, the approximate tracking framework, discussed in Sec. 2.1.4, is employed to track a desired roll maneuver near stall using the LRM mechanism.

3.5.1 Reduced-order three DOF Model

In this effort, we focus on the rolling capability of the new roll/yaw mechanism. As such, in order to accurately assess the efficacy of new roll mechanism, we develop a reduced-order three DOF flight dynamics model that possesses the minimal degrees of freedom needed to demonstrate its rolling capability. We then perform all the analyses in the rest of this section on the three DOF model . This model resembles a wind tunnel experiment (explained in detail later) that will be developed to verify the results. The three degrees of freedom included in this model are: heaving motion (z, W) constrained by a spring force, roll (ϕ, P), and pitch (θ, Q). The three DOF flight dynamics model can be written in a standard nonlinear system form as

$$\frac{d}{dt}\begin{bmatrix} z(t) \\ \phi(t) \\ \theta(t) \\ W(t) \\ P(t) \\ Q(t) \end{bmatrix} = \begin{bmatrix} W \\ P + Q\tan\theta\sin\phi \\ Q\cos\phi \\ -g - \frac{qS}{m}C_Z(\alpha) - \frac{qS}{2m}\frac{\bar{c}}{2V_T}\frac{C_{Z_Q}(\alpha)}{\cos\alpha}Q - \frac{k_s}{m}z \\ C_2PQ + C_3qSb\left(C_{\mathcal{L}}(\alpha) + \frac{b}{2V_T}C_{\mathcal{L}_P}(\alpha)P\right) \\ -C_6P^2 + C_7qS\bar{c}\left(C_M(\alpha) + \frac{\bar{c}}{2V_T}C_{M_Q}(\alpha)Q\right) \end{bmatrix} + \begin{bmatrix} 0 \\ 0 \\ 0 \\ \frac{qS}{m\cos\alpha}C_{Z_{\delta_e}}(\alpha) \\ 0 \\ C_7qS\bar{c}C_{M_{\delta_e}}(\alpha) \end{bmatrix}\delta_e + \begin{bmatrix} 0 \\ 0 \\ 0 \\ 0 \\ C_3qSbC_{\mathcal{L}_{\delta_a}}(\alpha) \\ 0 \end{bmatrix}\delta_a \tag{3.17}$$

where k_s is the spring stiffness. The system (3.17) can alternatively be written in an abstract form as

$$\dot{\boldsymbol{x}} = \boldsymbol{f}(\boldsymbol{x}) + \boldsymbol{g}_{\delta_e}(\boldsymbol{x})\delta_e + \boldsymbol{g}_{\delta_a}(\boldsymbol{x})\delta_a, \tag{3.18}$$

where the state vector $\boldsymbol{x} = [z \quad \phi \quad \theta \quad W \quad P \quad Q]^{\intercal}$.

3.5.2 Fliess Functional Expansion of the Roll Rate Output

In order to understand the various nonlinear effects induced by the aileron and elevator inputs on the roll rate, we develop an input-output representation for the three DOF system developed in the previous subsection. Such a representation could be developed using the Fliess functional expansion [72, PP. 105–135]. An output $y_j(t) = h_j(\boldsymbol{x}(t))$ of the nonlinear system (**??**) can be written as

$$y_j(t) = h_j(\boldsymbol{x}_0) + \sum_{k=0}^{\infty} \sum_{i_0,\ldots,i_k=0}^{m} L_{\boldsymbol{g}_{i_0}} \ldots L_{\boldsymbol{g}_{i_k}} h_j(\boldsymbol{x}_0) \int_0^t d\xi_{i_k} \ldots d\xi_{i_0}, \tag{3.19}$$

where $\boldsymbol{g}_0 = \boldsymbol{f}$, $L_{\boldsymbol{g}} h$ is the Lie derivative of h along $\boldsymbol{g}$, and $i_0, \ldots, i_k$ is a multiindex of length k (see Isidori [72, PP. 105–135] for more details). Writing the Fliess series expansion (3.19) of the roll rate output $P(t)$ of system (3.17), or alternatively (3.18), and truncating after two terms, we obtain the following non-zero terms

$$\begin{aligned} P(t) = P_0 + L_{\boldsymbol{g}_{\delta_a}} P\ (\boldsymbol{x}_0) \int_0^t \delta_a(\tau) d\tau + L_{\boldsymbol{g}_{\delta_a}} L_{\boldsymbol{f}} P\ (\boldsymbol{x}_0) \int_0^t \int_0^\tau \delta_a(s) ds d\tau + \\ + L_{\boldsymbol{f}} L_{\boldsymbol{g}_{\delta_a}} P\ (\boldsymbol{x}_0) \int_0^t \delta_a(\tau) \tau d\tau + L_{\boldsymbol{g}_{\delta_e}} L_{\boldsymbol{g}_{\delta_a}} P\ (\boldsymbol{x}_0) \int_0^t \delta_a(\tau) \int_0^\tau \delta_e(s) ds d\tau \end{aligned}. \tag{3.20}$$

It should be noted that the Lie bracket responsible for the new roll mechanism ($[\boldsymbol{g}_{\delta_e}, \boldsymbol{g}_{\delta_a}]$) can be written in terms of Lie derivatives as

$$[\boldsymbol{g}_{\delta_e}, \boldsymbol{g}_{\delta_a}] = L_{\boldsymbol{g}_{\delta_e}} L_{\boldsymbol{g}_{\delta_a}} - L_{\boldsymbol{g}_{\delta_a}} L_{\boldsymbol{g}_{\delta_e}}.$$

However, since $L_{\boldsymbol{g}_{\delta_a}} L_{\boldsymbol{g}_{\delta_e}} P = 0$, the effect of the Lie bracket $[\boldsymbol{g}_{\delta_e}, \boldsymbol{g}_{\delta_a}]$ is solely represented in the term $L_{\boldsymbol{g}_{\delta_e}} L_{\boldsymbol{g}_{\delta_a}} P$. Hence, the Fliess functional expansion truncation in Eq. (3.20) signifies the roles of both the direct aileron action (i.e., commanding only δ_a input) and the $[\boldsymbol{g}_{\delta_e}, \boldsymbol{g}_{\delta_a}]$ Lie bracket action in executing a roll maneuver.

For the rest of this section, we use the NASA GTM [70, 71] for analysis. NASA GTM is 5.5% dynamically scaled commercial transport model along with a nonlinear aerodynamic model that represents the aerodynamic coefficients and stability derivatives as polynomials in the angle of attack α and sideslip angle β. We consider a near-stall trim point, $\boldsymbol{x}_0 = [0 \quad 0 \quad \alpha_0 \quad 0 \quad 0 \quad 0]^\intercal$, where $\alpha_0 = 11.46°$. As such, the parameters included in the Fliess functional expansion truncation (3.20) are estimated as follows

$$\begin{aligned} L_{\boldsymbol{g}_{\delta_a}} P \ (\boldsymbol{x}_0) &= -0.131 \\ L_{\boldsymbol{g}_{\delta_a}} L_{\boldsymbol{f}} P \ (\boldsymbol{x}_0) &= 0.017 \\ L_{\boldsymbol{f}} L_{\boldsymbol{g}_{\delta_a}} P \ (\boldsymbol{x}_0) &= 4.33 * 10^{-15} \\ L_{\boldsymbol{g}_{\delta_e}} L_{\boldsymbol{g}_{\delta_a}} P \ (\boldsymbol{x}_0) &= -12.074 \end{aligned} \tag{3.21}$$

It is observed that the Lie-bracket-action-related coefficient, $L_{\boldsymbol{g}_{\delta_e}} L_{\boldsymbol{g}_{\delta_a}} P \ (\boldsymbol{x}_0)$, has a significantly higher value than the direct-aileron-action-related ones at the considered trim point. However, the total effect on the roll rate could be different when the iterated integrals are evaluated and taken into account. Such a comparison is considered in the next section.

3.5.3 Comparison between the Lie Roll and Conventional Roll Mechanisms

In this subsection, we consider two different methods to execute a roll maneuver at the considered near-stall trim point and conduct a comparative study between them while using NASA GTM's parameters. The first method is to command a fixed aileron deflection for a specific amount of time (i.e., the conventional roll mechanism). Whereas in the second method, we command the appropriate sinusoid signals (guided by the framework explained in Sec. 2.1.3) for both aileron and elevator that would realize motion along the direction of the Lie bracket vector field $[\boldsymbol{g}_{\delta_e}, \boldsymbol{g}_{\delta_a}]$ (i.e., the new discovered roll mechanism). For both methods we consider the aileron and elevator deflections to be bounded between $-30°$ and $30°$. We first compare between the two methods through investigating the Fliess functional expansion of the roll output shown in Eq. (3.20). Numerical simulations are then performed for both methods.

To examine the maximum capability of the conventional roll mechanism, we consider the following control input signals

$$\begin{aligned} &\delta_e(t) = 0 \\ &\delta_a(t) = -30° \end{aligned} . \tag{3.22}$$

Since the input-output representation in Eq. (3.20) is valid only for small time, we consider an excursion time $T = 0.5$ *sec*. It should be noted that by commanding only δ_a input, the effect of the last term in Eq. (3.20) would vanish. As such, evaluating the first three terms, we obtain $P(0.5) = 1.898\ deg/s$. Now, we examine the maximum capability of the LRM mechanism. Inspired by the control input sequence shown in Eq. (2.8), we use the following input signals for aileron and elevator inputs to realize the motion along the direction of the

Lie bracket vector field $[\boldsymbol{g}_{\delta_e}, \boldsymbol{g}_{\delta_a}]$

$$\begin{aligned} \delta_e(t) &= 2k_e\sqrt{j}\ \cos(j\omega t) \\ \delta_a(t) &= -k_a\sqrt{j}\ \omega\sin(j\omega t) \end{aligned}, \tag{3.23}$$

where j is chosen to be equal to 19 and $\omega = 1$, which renders an oscillation frequency of 3 hz. k_e and k_a are chosen so that the input signals do not exceed the bounds (i.e., $\delta_e, \delta_a \in [-30°, 30°]$). Hence, we set $k_e = 0.0595$ and $k_a = 0.119$. As such, evaluating the roll output after the excursion time, we obtain $P(0.5) = 2.825\ deg/s$. Hence 50% more roll rate is achieved using the LRM's control inputs, given in Eq. (3.23).

Next, we perform numerical simulations for both cases using the three DOF model (3.17). We start the simulations at the same initial condition $\boldsymbol{x}_0$ used to examine the Fliess functional expansion of the roll output. Figures 3.5 and 3.6 show the control input history along with the roll output over one second using the conventional roll mechanism and the LRM, respectively. Inspecting the simulation results, we observe that the roll angle reached 8° at the end of the one-second maneuver when using the LRM, as opposed to only 1.9° roll angle for the conventional roll mechanism (constant aileron deflection). That is, the LRM mechanism is able to generate more than four times as much roll as the conventional one is capable of at this operating point. This result complies with what was noted earlier from the Fliess functional expansion of the roll output. Hence, it is concluded that the discovered new Lie-bracket roll mechanism is superior to the conventional one at near-stall operating conditions.

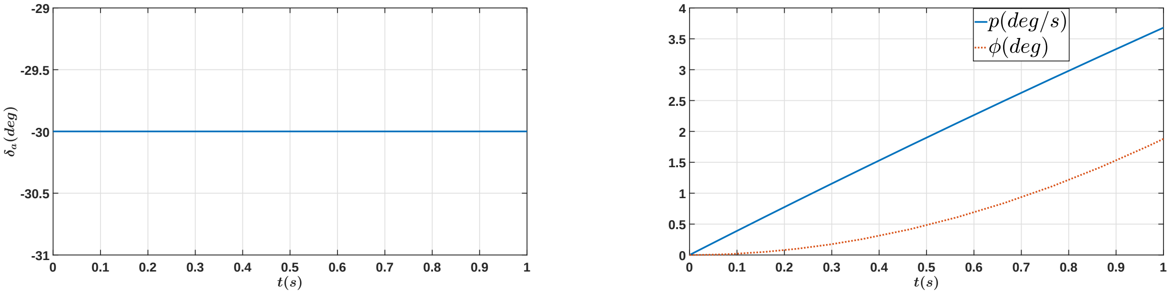

(a) Control input history.

(b) Roll output.

Figure 3.5: Numerical simulation of the three DOF model (3.17) under the control input signals given in Eq. (3.22) to examine the maximum capability of the conventional roll mechanism.

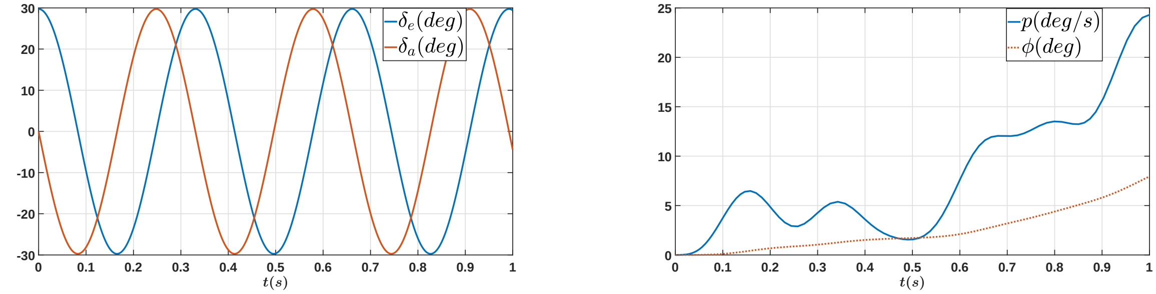

(a) Control input history.

(b) Roll output.

Figure 3.6: Numerical simulation of the three DOF model (3.17) under the control input signals given in Eq. (3.23) to examine the maximum capability of the Lie roll mechanism.

3.5.4 Implementation of the Lie Roll Mechanism as a Nonlinear Motion Planning Problem

Now, that the LRM mechanism has been proved superior to the conventional one (direct aileron action) at near-stall operating points, it is of interest to investigate trajectory tracking capability of this new roll mechanism. Consider the following desired trajectory

$$\boldsymbol{x}_d = \begin{bmatrix} 0 & c\,\dfrac{t^2}{2} & 0 & 0 & c\,t & 0 \end{bmatrix}^\intercal, \tag{3.24}$$

where $k = 0.01$, to be performed at the same near-stall operating point considered in the previous subsection. That is, a pure roll maneuver with constant roll acceleration equals to c

needs to be performed. As such, we utilize the framework explained in Sec. 2.1.3 to perform approximate trajectory tracking relying on the LRM to generate the desired roll motion.

As explained in Sec. 2.1.3, the first step is to cast the system in the extended form, i.e., add the Lie bracket inputs as physical inputs to the system. As such, we write the following extended version of the three DOF system (3.17) or equivalently (3.18)

$$\dot{\boldsymbol{x}} = \boldsymbol{f}(\boldsymbol{x}) + \boldsymbol{g}_{\delta_e}(\boldsymbol{x})v_{\delta_e} + [\boldsymbol{g}_{\delta_e}, \boldsymbol{g}_{\delta_a}](\boldsymbol{x})v_{[\delta_e,\delta_a]}. \tag{3.25}$$

It should be noted that the direct aileron input is not included in the extended system as it is considered to be inefficient at this near-stall operating point. Through employing Eq. (2.7), the extended inputs needed to track the desired trajectory can be obtained, which are shown in Fig. 3.7.

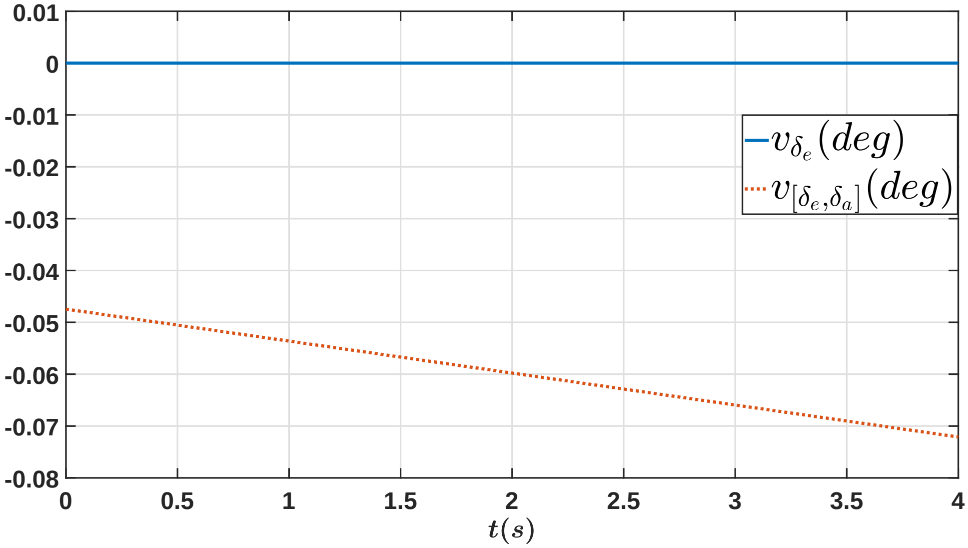

Figure 3.7: The extended controls needed to track the desired trajectory (3.24).

The next step is to transform those extended inputs into ordinary inputs via employing the first-order Lie brackets realization algorithm outlined in Sec. 2.1.3. One caveat we should mention is that the algorithm given in Eq. (2.8) often produces very high amplitude control inputs. The reason is that tracking a trajectory through this algorithm requires high control input oscillation frequencies, and since the input signal's amplitude is scaled by the oscillation frequency, the yielded amplitudes are also quite high. In our specific example, however, we observed that only one input signal (u_{k_2} in Eq. (2.8)) was exceeding the bounds and the other one (u_{k_1} in Eq. (2.8)) has quite low amplitude. To overcome this hurdle and make both signals abide by the bounds, we introduced the following modification to Liu's algorithm (2.8)

$$\begin{aligned} u^j_{k_1}(t) &= -k_c\sqrt{j}\ \omega\ v_{k_3}(t)\sin(j\omega t) \\ u^j_{k_2}(t) &= \frac{2}{k_c}\sqrt{j}\ \cos(j\omega t) \end{aligned}, \tag{3.26}$$

where k_c is chosen so that the high amplitude signal (u_{k_2}) could be scaled down to the control bounds. The introduced modification does not affect the tracking accuracy because the modified algorithm in Eq. (3.26) realizes motion along the same Lie bracket vector field as that of original one (2.8). To explain this point, we have to appeal to the Lie bracket computation. Consider the Lie bracket between two vector fields $\boldsymbol{g}_1(\boldsymbol{x})$ and $\boldsymbol{g}_2(\boldsymbol{x})$

$$[\boldsymbol{g}_1, \boldsymbol{g}_2] = \frac{\partial \boldsymbol{g}_2}{\partial \boldsymbol{x}}\boldsymbol{g}_1 - \frac{\partial \boldsymbol{g}_1}{\partial \boldsymbol{x}}\boldsymbol{g}_2.$$

Now, consider the Lie bracket between $k_c\ \boldsymbol{g}_1(\boldsymbol{x})$ and $\frac{1}{k_c}\ \boldsymbol{g}_2(\boldsymbol{x})$

$$[k_c\ \boldsymbol{g}_1, \frac{1}{k_c}\ \boldsymbol{g}_2] = \frac{1}{k_c}\frac{\partial \boldsymbol{g}_2}{\partial \boldsymbol{x}}\boldsymbol{g}_1 k_c - k_c\frac{\partial \boldsymbol{g}_1}{\partial \boldsymbol{x}}\boldsymbol{g}_2\frac{1}{k_c} = \frac{\partial \boldsymbol{g}_2}{\partial \boldsymbol{x}}\boldsymbol{g}_1 - \frac{\partial \boldsymbol{g}_1}{\partial \boldsymbol{x}}\boldsymbol{g}_2 = [\boldsymbol{g}_1, \boldsymbol{g}_2].$$

Hence, the scaling modification does not alter the vector field being realized.

As such, we use the modified algorithm (3.26) to obtain the ordinary control input signals as follows

$$\begin{aligned} \delta_e(t) &= v_{\delta_e}(t) + \frac{2}{k_c}\sqrt{j}\ \cos(j\omega t) \\ \delta_a(t) &= -k_c\sqrt{j}\ \omega\ v_{[\delta_e,\delta_a]}(t)\sin(j\omega t) \end{aligned}. \tag{3.27}$$

Figures 3.8 and 3.9 show the actual versus desired response and the ordinary control inputs, respectively, for $\omega = 1$ and $j = 100$ (i.e., oscillation frequency $\approxeq 16hz$). It is noted from Fig. 3.8 that the actual and desired trajectories are not in exact agreement. The reason is that, as we referred to earlier, accurate tracking using this algorithm requires quite high input frequencies which might not be feasible in real systems. To further explain this point, we performed the same tracking at higher frequency (48 hz), which is shown in Figs. 3.10 and 3.11. It is noted from Fig. 3.10 that both desired and actual are in perfect agreement, yet the control inputs exceeded the bounds ($[-30°, 30°]$) as shown in Fig. 3.11. That is, tracking accuracy could be partially sacrificed in return of bounds-abiding control inputs and a feasible range of input frequencies.

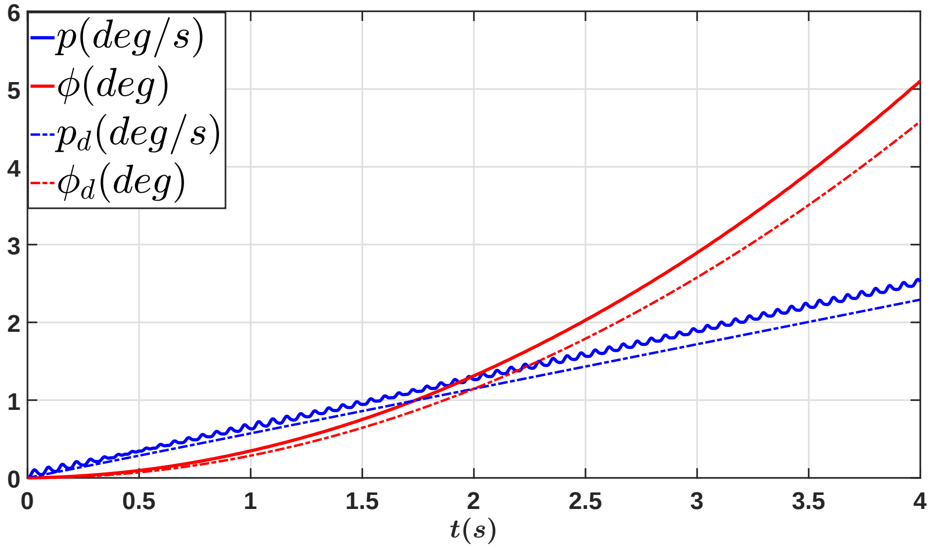

Figure 3.8: Actual versus desired response of the three DOF model (3.17) under the control inputs given by Eq. (3.27) and using input frequency of 16 hz.

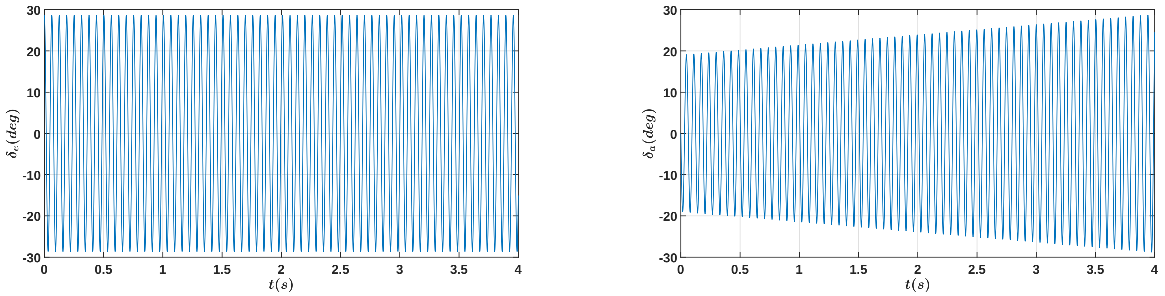

(a) Elevator input.

(b) Aileron input.

Figure 3.9: Ordinary control inputs obtained through Eq. (3.27) with input frequency of 16 hz, used to track the desired trajectory (3.24) of the three DOF system (3.17).

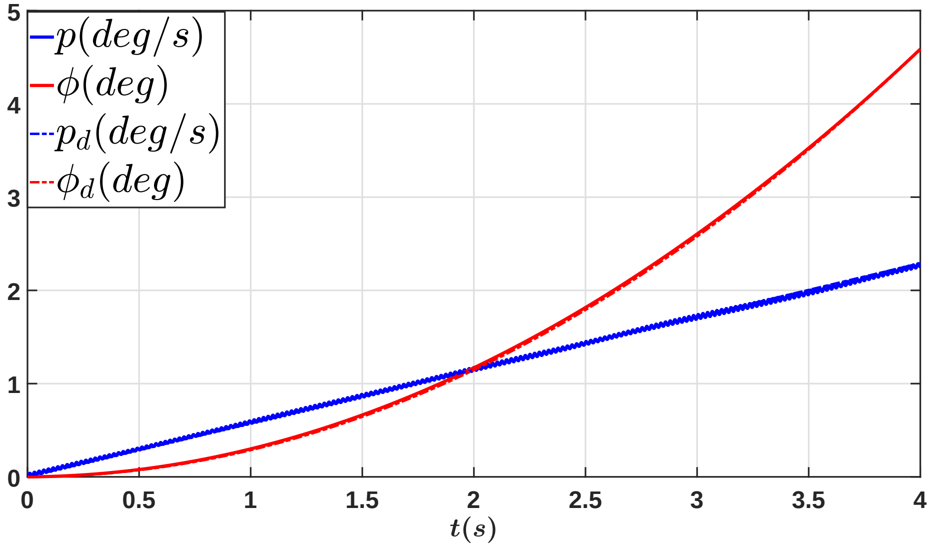

Figure 3.10: Actual versus desired response of the three DOF model (3.17) under the control inputs given by Eq. (3.27) and using input frequency of 48 hz.

3.6 Nonlinear Controllability Analysis at a Loss of Control Situation (Hydraulic Failure)

One of the most interesting airplane upset situations is a hydraulic failure, leading to control surfaces jamming. There is a detailed study by Lemaignan on the DHL A300-B4 airplane incident when it was hit by a ground-to-air missile during the initial climb after taking off from Baghdad airport in 2003. Because of that, within few seconds, all hydraulics were lost

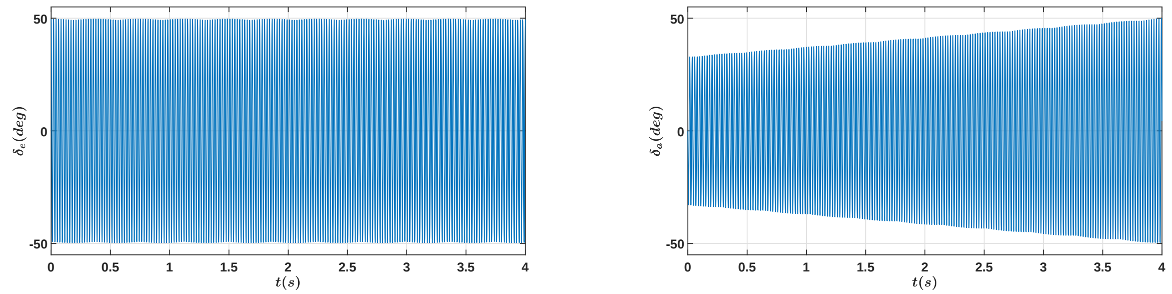

(a) Elevator input.

(b) Aileron input.

Figure 3.11: Ordinary control inputs obtained through Eq. (3.27) with input frequency of 48 hz, used to track the desired trajectory (3.24) of the three DOF system (3.17).

[73]. The crew managed to land the airplane safely using only the thrust controls. Also, as we referred earlier in this work, thrust-only flight control systems (TFCSs) have been investigated by Burcham et al. [63, 64] and Tucker [65] at NASA Dryden Flight Research Center over the 1990s, and by Yamasaki et al. [62] in 2011.

In this section, we analyze the thrust-only flight control systems from the controllability point of view. We consider the full flight dynamics model (twelve states) and the controllability of this system using TFCS (symmetric and asymmetric thrust inputs) is analyzed using linear and nonlinear control analysis tools. The model considered in this section is Convair 880 aircraft model [74, PP.414–415] while the aerodynamic coefficients are represented using NASA general transport model (NASA GTM) [71] which is a nonlinear aerodynamic model that represents the aerodynamic coefficients as polynomials in the angle of attack α and side-slip angle β. The nonlinear flight dynamics model using TFCS can be written as

$$\dot{\boldsymbol{x}} = \boldsymbol{f}(\boldsymbol{x}) + \boldsymbol{g}_s(\boldsymbol{x})\delta_{t_s} + \boldsymbol{g}_a(\boldsymbol{x})\delta_{t_a} \tag{3.28}$$

where δ_{t_s} denotes the symmetric thrust input and δ_{t_a} denotes the asymmetric thrust input.

$\boldsymbol{f}(\boldsymbol{x})$, $\boldsymbol{g}_s(\boldsymbol{x})$, and $\boldsymbol{g}_a(\boldsymbol{x})$ can be written as

$$\boldsymbol{f}(\boldsymbol{x}) = \begin{bmatrix} RV - QW - g\sin\theta + \frac{F_X}{m} \\ PW - RU + g\cos\theta\sin\phi + \frac{F_Y}{m} \\ QU - PV + g\cos\theta\cos\phi + \frac{F_Z}{m} \\ Q(C_1R + C_2P) + C_3\mathcal{L} + C_4N \\ C_5PR - C_6\left(P^2 - R^2\right) + C_7M \\ C_4\mathcal{L} + C_9N + Q(C_8P - C_2R) \\ P + \tan\theta(Q\sin\phi + R\cos\phi) \\ Q\cos\phi - R\sin\phi \\ \sec\theta(Q\sin\phi + R\cos\phi) \\ U\cos\theta\cos\psi + V(\sin\theta\cos\psi\sin\phi - \sin\psi\cos\phi) \\ +W(\sin\theta\cos\psi\cos\phi + \sin\psi\sin\phi) - U_0\cos\theta_0 - W_0\sin\theta_0 \\ U\cos\theta\sin\psi + V(\sin\theta\sin\psi\sin\phi + \cos\psi\cos\phi) \\ +W(\sin\theta\sin\psi\cos\phi - \cos\psi\sin\phi) \\ U\sin\theta - V\cos\theta\sin\phi - W\cos\theta\cos\phi \end{bmatrix}$$

$$\boldsymbol{g}_s = \begin{bmatrix} X_{\delta_{t_s}} & 0 & 0 & 0 & M_{\delta_{t_s}} & 0 & 0 & 0 & 0 & 0 & 0 & 0 \end{bmatrix}^\intercal$$

$$\boldsymbol{g}_a = \begin{bmatrix} 0 & 0 & 0 & \mathcal{L}_{\delta_{t_a}} & 0 & N_{\delta_{t_a}} & 0 & 0 & 0 & 0 & 0 & 0 \end{bmatrix}^\intercal$$

where the state vector $\boldsymbol{x} = [U \quad V \quad W \quad P \quad Q \quad R \quad \phi \quad \theta \quad \psi \quad P_N \quad P_E \quad h]^{\intercal}$, and the the aerodynamic loads $F_X, F_Y, F_Z, \mathcal{L}, M$, and N are calculated using NASA GTM at the flight condition (sea level cruise, M=0.25). It should be noted that for zero-cross-coupling moment of inertia airplanes the control derivative $\mathcal{L}_{\delta_{t_a}}$ is zero.

Now, we consider the linearized system at the cruise point $\boldsymbol{x}_0$

$$\dot{\boldsymbol{x}} = \boldsymbol{A}\ \boldsymbol{x} + \boldsymbol{B}_1\ \delta_{t_s} + \boldsymbol{B}_2\ \delta_{t_a}$$

where $\boldsymbol{A} = \left[\frac{\partial \boldsymbol{f}}{\partial \boldsymbol{x}}\right]$ evaluated at $\boldsymbol{x}_0$, $\boldsymbol{B}_1 = \boldsymbol{g}_s(\boldsymbol{x}_0)$, and $\boldsymbol{B}_2 = \boldsymbol{g}_a(\boldsymbol{x}_0)$. Kalman rank condition can be checked for this system by constructing the controllability matrix

$$\boldsymbol{C} = \begin{bmatrix}\boldsymbol{B}_1 & \boldsymbol{B}_2 & \boldsymbol{A}\boldsymbol{B}_1 & \boldsymbol{A}^2\boldsymbol{B}_1 & .... & \boldsymbol{A}^{11}\boldsymbol{B}_1 & \boldsymbol{A}\boldsymbol{B}_2 & \boldsymbol{A}^2\boldsymbol{B}_2 & .... & \boldsymbol{A}^{11}\boldsymbol{B}_2\end{bmatrix}$$

The rank of this matrix is found to be *eleven* which means that the linearized system is *uncontrollable*.

As stated before, we can assess the accessibility of this system at an equilibrium point $\boldsymbol{x_0}$ by calculating the rank of the accessibility distribution, Eq. (2.3). The accessibility distribution can be seen as the infinite Lie-bracket iterations between the drift, $\boldsymbol{f}(\boldsymbol{x})$, and control inputs, $\boldsymbol{g}_s(\boldsymbol{x})$ and $\boldsymbol{g}_a(\boldsymbol{x})$, vector fields. This invokes the definition of the *P. Hall basis*. We can loosely say that the P. Hall basis of order k represents all the independent Lie brackets resulting from Lie-bracket iterations of the system vector fields up to k brackets' length. Here we consider the P. Hall basis of order four for the system's vector fields $\boldsymbol{f}, \boldsymbol{g}_s$, and $\boldsymbol{g}_a$ along with some of the Lie brackets of length five. Following Munthe-Kaas et al., [75] the P. Hall basis for the three vector fields $\boldsymbol{f}, \boldsymbol{g}_s$, and $\boldsymbol{g}_a$ of order four can be summarized in Table 3.1.

The first step in the nonlinear analysis would be to calculate the rank of the accessibility

bracket length	Lie brackets
one	$\boldsymbol{f}$, $\boldsymbol{g}_s$, and $\boldsymbol{g}_a$
two	$[\boldsymbol{f},\boldsymbol{g}_s]$, $[\boldsymbol{f},\boldsymbol{g}_a]$, and $[\boldsymbol{g}_s,\boldsymbol{g}_a]$
three	$[\boldsymbol{f},[\boldsymbol{f},\boldsymbol{g}_s]]$, $[\boldsymbol{f},[\boldsymbol{f},\boldsymbol{g}_a]]$, $[\boldsymbol{g}_s,[\boldsymbol{f},\boldsymbol{g}_s]]$ $[\boldsymbol{g}_s,[\boldsymbol{f},\boldsymbol{g}_a]]$, $[\boldsymbol{g}_s,[\boldsymbol{g}_s,\boldsymbol{g}_a]]$, $[\boldsymbol{g}_a,[\boldsymbol{f},\boldsymbol{g}_s]]$, $[\boldsymbol{g}_a,[\boldsymbol{f},\boldsymbol{g}_a]]$, and $[\boldsymbol{g}_a,[\boldsymbol{g}_s,\boldsymbol{g}_a]]$
four	$[\boldsymbol{f},[\boldsymbol{f},[\boldsymbol{f},\boldsymbol{g}_s]]]$, $[\boldsymbol{g}_s,[\boldsymbol{f},[\boldsymbol{f},\boldsymbol{g}_a]]]$, $[\boldsymbol{g}_s,[\boldsymbol{g}_s,[\boldsymbol{g}_s,\boldsymbol{g}_a]]]$, $[\boldsymbol{g}_a,[\boldsymbol{g}_s,[\boldsymbol{f},\boldsymbol{g}_s]]]$, $[\boldsymbol{g}_a,[\boldsymbol{g}_a,[\boldsymbol{f},\boldsymbol{g}_s]]]$, $[[\boldsymbol{f},\boldsymbol{g}_s],[\boldsymbol{f},\boldsymbol{g}_a]]$, $[\boldsymbol{f},[\boldsymbol{f},[\boldsymbol{f},\boldsymbol{g}_a]]]$, $[\boldsymbol{g}_s,[\boldsymbol{g}_s,[\boldsymbol{f},\boldsymbol{g}_s]]]$, $[\boldsymbol{g}_a,[\boldsymbol{f},[\boldsymbol{f},\boldsymbol{g}_s]]]$, $[\boldsymbol{g}_a,[\boldsymbol{g}_s,[\boldsymbol{f},\boldsymbol{g}_a]]]$, $[\boldsymbol{g}_a,[\boldsymbol{g}_a,[\boldsymbol{f},\boldsymbol{g}_a]]]$, $[[\boldsymbol{f},\boldsymbol{g}_s],[\boldsymbol{g}_s,\boldsymbol{g}_a]]$, $[\boldsymbol{g}_s,[\boldsymbol{f},[\boldsymbol{f},\boldsymbol{g}_s]]]$, $[\boldsymbol{g}_s,[\boldsymbol{g}_s,[\boldsymbol{f},\boldsymbol{g}_a]]]$, $[\boldsymbol{g}_a,[\boldsymbol{f},[\boldsymbol{f},\boldsymbol{g}_a]]]$, $[\boldsymbol{g}_a,[\boldsymbol{g}_s,[\boldsymbol{g}_s,\boldsymbol{g}_a]]]$, $[\boldsymbol{g}_a,[\boldsymbol{g}_a,[\boldsymbol{g}_s,\boldsymbol{g}_a]]]$, and $[[\boldsymbol{f},\boldsymbol{g}_a],[\boldsymbol{g}_s,\boldsymbol{g}_a]]$

Table 3.1: P. Hall basis of order four for the three vector fields $\boldsymbol{f}, \boldsymbol{g}_s$, and $\boldsymbol{g}_a$.

distribution while including only the linear-analysis-related Lie brackets, ($\boldsymbol{g}_s$, $\boldsymbol{g}_a$, $[\boldsymbol{f},\boldsymbol{g}_s]$ up to $ad^{11}_{\boldsymbol{f}}\boldsymbol{g}_s$, and $[\boldsymbol{f},\boldsymbol{g}_a]$ up to $ad^{11}_{\boldsymbol{f}}\boldsymbol{g}_a$). The rank of the accessibility distribution in this case is found to be *eleven*, as expected, which means that the system is linearly uncontrollable. The second step would be to add all the new Lie brackets included in the P. Hall basis to the accessibility distribution, one at a time, to check if a given Lie bracket could provide motion along the missed direction, i.e., it completes the rank of the accessibility distribution. Using those Lie brackets included in the P. Hall basis shown above along with some Lie brackets of length five, we obtain the Lie brackets that can satisfy the LARC in four different configuration cases as summarized in Table 3.2.

It is noted from the results in Table 3.2 that the existence of either cross-coupling moment of inertia (non-zero I_{XZ}) or an offset between the thrust line and center of mass line (non-zero $M_{\delta_{ts}}$) suffices to achieve full accessibility distribution rank [76, 66]. However, the LARC cannot be realized in the absence of the cross-coupling moment of inertia and $M_{\delta_{ts}}$ together. Having said that, we can conclude that the system in this case is *accessible*. To conclude that the system is controllable or *small time locally controllable* (STLC), further nonlinear analysis would be required to check if any of the new Lie brackets represents an *obstruction* to controllability. More details on this point can be found in the work of Sussmann [36].

Non-zero I_{XZ}	Non-zero $M_{\delta_{ts}}$	Lie brackets that complete the full rank for *accessibility*
✓	✗	$[\boldsymbol{g}_a,[\boldsymbol{f},\boldsymbol{g}_a]]$ $[[[\boldsymbol{f},[\boldsymbol{f},\boldsymbol{g}_s]],\boldsymbol{g}_a],\boldsymbol{g}_a]$ $[[[\boldsymbol{f},[\boldsymbol{f},\boldsymbol{g}_s]],\boldsymbol{g}_s],\boldsymbol{g}_s]$
✓	✓	$[\boldsymbol{g}_s,[\boldsymbol{f},\boldsymbol{g}_s]]$ $[\boldsymbol{g}_a,[\boldsymbol{f},\boldsymbol{g}_a]]$ $[\boldsymbol{g}_s,[\boldsymbol{g}_s,[\boldsymbol{f},\boldsymbol{g}_s]]]$ $[\boldsymbol{g}_s,[\boldsymbol{f},[\boldsymbol{f},[\boldsymbol{f},\boldsymbol{g}_s]]]]$ $[\boldsymbol{g}_a,[\boldsymbol{f},[\boldsymbol{f},[\boldsymbol{f},\boldsymbol{g}_a]]]]$ $[[[\boldsymbol{f},[\boldsymbol{f},\boldsymbol{g}_s]],\boldsymbol{g}_s],\boldsymbol{g}_s]$ $[[[\boldsymbol{g}_s,[\boldsymbol{f},\boldsymbol{g}_s]],\boldsymbol{g}_s],\boldsymbol{g}_s]$
✗	✗	–
✗	✓	$[\boldsymbol{g}_s,[\boldsymbol{f},\boldsymbol{g}_s]]$ $[\boldsymbol{g}_s,[\boldsymbol{g}_s,[\boldsymbol{f},\boldsymbol{g}_s]]]$ $[\boldsymbol{g}_s,[\boldsymbol{f},[\boldsymbol{f},[\boldsymbol{f},\boldsymbol{g}_s]]]]$ $[\boldsymbol{g}_a,[\boldsymbol{f},[\boldsymbol{f},[\boldsymbol{f},\boldsymbol{g}_a]]]]$ $[[[\boldsymbol{f},[\boldsymbol{f},\boldsymbol{g}_s]],\boldsymbol{g}_s],\boldsymbol{g}_s]$ $[[[\boldsymbol{g}_s,[\boldsymbol{f},\boldsymbol{g}_s]],\boldsymbol{g}_s],\boldsymbol{g}_s]$

Table 3.2: Nonlinear controllability analysis results for the 12 × 12 flight dynamics system.

It should be noted the results summarized in Table 3.2 are congruent with Crouch's theorem [14]; that is, the attitude of a rigid body can be completely controlled via a single moment about a non-principal axis. Thus, if $I_{XZ} = 0$ (all axes are principal), the differential thrust yaw capability is not enough and pitching capability is essential (i.e., $M_{\delta_{ts}} \neq 0$). On the other hand, if $I_{XZ} \neq 0$, the single yaw moment control is about a non-principal axis, which suffices according to Crouch's theorem.

3.7 Conclusions

In this chapter, the fixed-wing airplane flight dynamics is formulated in a geometric-nonlinear-control framework. The six DOF flight dynamics model is presented in a full nonlinear sense; i.e., nonlinear in dynamics as well as aerodynamics. As such, all the effects emanating from the nonlinearity of the dynamics and aerodynamics could be revealed. In particular, new rolling/yawing and pitching mechanisms are introduced. The new rolling/yawing mechanism shows a potential advantage over the conventional one if used near stall.

In order to thoroughly investigate the new rolling/yawing mechanism, a reduced-order, three DOF flight dynamics model is developed to perform a comprehensive investigation of the Lie roll mechanism. The LRM is executed through realizing the Lie bracket between elevator and aileron control vector fields. Realizing the motion along the direction of a Lie bracket vector field in a nonlinear system with drift invokes motion planning tools from differential-geometric control theory. Hence, the approximate trajectory tracking framework, outlined in Sec. 2.1.3, is invoked. Employing this framework, and using the NASA GTM for analysis and simulation, the maximum capability of the LRM near stall is examined and compared to that of the conventional one. The simulation results indicate a superiority of the new roll mechanism over the conventional one at near-stall operating points, in compliance with the results of Fliess functional expansion analysis of the roll rate output. In particular, the LRM is able to generate more than four times as much roll as the conventional one is capable of at that operating point. Hence, the LRM may provide a more efficient way to recover from stall/spin situations in commercial and general aviation aircraft. Moreover, the developed framework in Sec. 2.1.3 is employed in order to track a desired roll trajectory near stall. Trajectory tracking simulation results indicate the need for high input frequency if high tracking accuracy is sought. However, high input frequency may not be feasible for real systems due to the actuator and structural limitations. Hence, the provided framework is considered as an approximate trajectory tracking method for such systems.

Moreover, we introduce a methodology for analyzing the nonlinear controllability of the airplane utilizing the differential-geometric control tools. As such, the controllability assessment of some upset situations could be revisited. Nonlinear controllability analysis in case of complete hydraulic failure, i.e., using thrust controls only, is performed. The system is shown to be nonlinearly controllable if either I_{XZ} or $M_{\delta_{t_s}}$ is non-zero., despite being linearly uncontrollable.

Chapter 4

Differential-Geometric-Control Formulation and Stability Analysis of Flapping Flight Multi-Body Dynamics

Flapping flight dynamics is quite an intricate problem that is typically represented by a multi-body, multi-scale, nonlinear, time-varying dynamical system. The unduly simple modeling and analysis of such dynamics in the literature has long obstructed the discovery of some of the fascinating mechanisms that these flapping-wing creatures possess. Neglecting the wing inertial effects and directly averaging the dynamics over the flapping cycle are two major simplifying assumptions that have been extensively used in the literature of flapping flight balance and stability analysis. By relaxing these assumptions and formulating the multi-body dynamics of flapping-wing micro-air-vehicles in a differential-geometric-control framework, a *vibrational stabilization* mechanism that greatly contributes to the body pitch stabilization is revealed. The discovered vibrational stabilization mechanism is induced by the interaction between the fast oscillatory aerodynamic loads on the wings and the relatively-slow body motion. This stabilization mechanism provides an artificial stiffness (i.e., spring action) to the body rotation around its pitch axis. Such a spring action is similar to that of *Kapitza pendulum* where the unstable inverted pendulum is stabilized through applying fast-enough periodic forcing. Such a phenomenon cannot be captured using the overly simplified modeling and analysis of flapping flight dynamics.

4.1 Introduction

Biological flyers represent a gold mine of scientifically-rich problems and a well-spring of knowledge and inspiration for engineers and scientists. For example, some insects can thrust up to five times their weights [77], while others have been observed to perform turning maneuvers of greater than 3000 deg/s, with less than a 30 ms delay [78], in situations that demand agility, such as chasing a potential mate. In normal everyday flight, birds may experience up to 14 g accelerations in super-maneuverable tasks [79], while the maneuverability of the most advanced fighter airplanes cannot exceed $8-9$ g. Moreover, birds and insects outperform jet airplanes more than five times from a normalized power consumption perspective [79]. This huge potential inspired engineers to design flapping-wing micro-air-vehicles (FWMAVs) [80], mainly for reconnaissance and surveillance applications.

Indeed, flapping flight invokes and pushes the frontiers of mechanical and aerospace engineering disciplines. From an aerodynamic point of view, flapping flight creates an unsteady, nonlinear flow field exploiting unconventional mechanisms to generate lift. In fact, using classical aerodynamics, insect flight was deemed impossible for decades (e.g., [81, 82, 83, 84]), as the required lift coefficients for balance are $2-3$ times the maximum lift coefficients achieved by conventional aerodynamics. Later, biologists and engineers unraveled some of the unconventional lift mechanisms exploited by insect and bird flight. A stabilized leading edge vortex, first introduced by Ellington and his coworkers [85], forms the main unconventional lift mechanism that makes insect flight possible. Computational fluid dynamic simulations show that the leading edge vortex contributes 40% of the total lift for insects [86]. Recently, many studies accounted for the unsteady and viscous aerodynamics of flapping-flight and similar flight behaviors [68, 87, 88, 89, 90, 91, 92, 93, 94, 95, 96, 97, 98, 99, 100, 101, 102, 103, 104, 105].

As the aerodynamics of flapping flight became mature, the flight dynamic analysis followed promptly. To our knowledge, the first article on flapping flight dynamics is that of Thomas and Taylor [106]. Flapping flight dynamics represents a multi-body, nonlinear time-periodic (NLTP) dynamical system. Moreover, it is a multi-scale dynamical system because of the concomitant two time scales: the fast time scale of the flapping motion and the associated aerodynamic loads, and the relatively-slow time scale of the body motion. All these challenges make flapping flight dynamics an intricate problem that necessitates a rigorous mathematical analysis.

Two major assumptions have been typically adopted in the flight dynamic analysis of FW-MAVs [107]: neglecting the wing inertial effects and directly averaging the dynamics over the flapping cycle. The first assumption might be justifiable because the mass of the wing is quite small when compared to that of the body (less than 5% [108]). Moreover, adopting this assumption alleviates the problem's complexity and yields flight dynamic equations similar to those of conventional aircraft. As such, most of the analyses in the literature of flapping flight dynamics and control have neglected the wing inertial effects [106, 109, 110, 111, 112, 113, 114, 40, 115, 116, 117, 118]. For more details about the effects of the wing's inertia on the dynamics of flapping flight, the reader is referred to the review articles [107, 119], and the references therein.

The second major assumption (directly averaging the dynamics over the flapping cycle) has been refuted by Taha et al. [120, 50] for hovering insects with a relatively small flapping frequency (e.g., hawkmoth and cranefly). They showed that despite the large ratio of the forcing flapping frequency to the natural frequency of the body motion (30 for the hawkmoth and 50 for the cranefly), there is a strong interaction between the system's two time scales that considerably affects the flight balance and stability. Specifically, the intuition that an averaged lift due to flapping equal to the FWMAV's weight ensures vertical balance at hover was interestingly refuted by showing that the aerodynamic-dynamic interaction results in a negative lifting mechanism. In addition, the interaction between the system's two time scales results in a vibrational stabilization phenomenon that is quite similar to the well-known behavior of the Kapitza pendulum [30]: the unstable equilibrium of the inverted pendulum is stabilized through open-loop vertical oscillations of the pivot. These interactions are essentially neglected when direct averaging is used.

On the other hand, some efforts [121, 41, 42] aimed at capturing the periodic orbit associated with certain equilibrium configuration (e.g., hovering) using periodic shooting methods, then analyzing the stability of that orbit using Floquet theorem. However, this would only yield a yes/no answer to the stability question without any insights as to why this system has been rendered stable/unstable and what are the stabilizing/destabilizing mechanisms.

While pursuing the relaxation of those two assumptions, *differential geometric control theory* is naturally invoked as a rigorous analysis tool. It is particularly convenient for the analysis of multi-body, underactuated mechanical systems [46]. Moreover, when combined with *chronological calculus* [23], it provides constructive techniques for higher-order averaging of NLTP systems [48, 122, 49] and dealing with multi-scale vibrational control systems [47]. As such, the goal of this effort is to relax the aforementioned simplifying assumptions and hence: (i) derive the full (five degrees of freedom), multi-body, longitudinal flight dynamics of FWMAVs and cast it in a differential-geometric-control framework; (ii) combine differential geometric control and averaging tools to rigorously and analytically investigate the balance and stability of flapping flight dynamics at hover; and (iii) unravel and investigate the unconventional flight dynamic behavior of flapping flight (e.g., vibrational stabilization and negative lifting), and demonstrate the role of multi-body effects in such a behavior.

In this chapter, the five degree-of-freedom (DOF), multi-body equations of motion governing the longitudinal flight dynamics of FWMAVs near hover are derived using the principle of virtual power [123]. A relatively simple, analytical aerodynamic model that accounts for the dominant contributions (e.g., leading edge vortex and rotational effects) is adopted. Combining these two models (aerodynamic and dynamic), a nonlinear, multi-body, time-varying, longitudinal flight dynamics model is developed, which captures aerodynamic-dynamic interactions. A two DOF FWMAV model is derived from the full longitudinal model as the simplest multi-body model for balance analysis at hover. This two DOF model resembles an experimental setup of a FWMAV restrained to move along vertical rails; where balance and stability are decoupled. Additionally, an analysis framework combining averaging and periodic shooting is introduced and demonstrated on the simple two DOF model to rigorously analyze the balance problem at hover. Moreover, a three DOF model is then extracted from the full model as the simplest, yet rich enough, multi-body, flapping flight dynamics model for differential-geometric-control balance and stability analysis. This three DOF model resembles an experimental apparatus for investigating both balance and stability at hover. The geometric-control-averaging tools are then applied to the three DOF model to reveal the role of wing-body dynamical interaction in vibrational pitch stabilization for the insect/vehicle's body. The vibrational pitch stabilization mechanism is induced by the interaction between the fast, periodic, aerodynamic wing forces and the relatively-slow body motion (aerodynamic-dynamic interactions). Such a mechanism would have been entirely overlooked if direct averaging techniques are applied instead. Moreover, the obtained analytical results are verified through numerical periodic shooting and Floquet stability analysis. Finally, a comparison is made with the corresponding single-body model to provide insights into the multi-body effects.

4.2 Modeling of the Multi-Body, Time-Varying Flapping Flight Dynamics

4.2.1 Wing Kinematics

Figure 4.1 shows a schematic diagram of a FWMAV and its axis systems. Four reference frames are required to study the flight dynamics of a rigid-wing FWMAV: an inertial reference frame $\{x_\text{I}, y_\text{I}, z_\text{I}\}$, a body-fixed reference frame $\{x_\text{b}, y_\text{b}, z_\text{b}\}$, a stroke plane reference frame $\{x_\text{s}, y_\text{s}, z_\text{s}\}$, and a wing-fixed reference frame $\{x_\text{w}, y_\text{w}, z_\text{w}\}$ for each of the flight vehicle's wings. Because only longitudinal flight is considered in this work, symmetric wing motions are assumed.

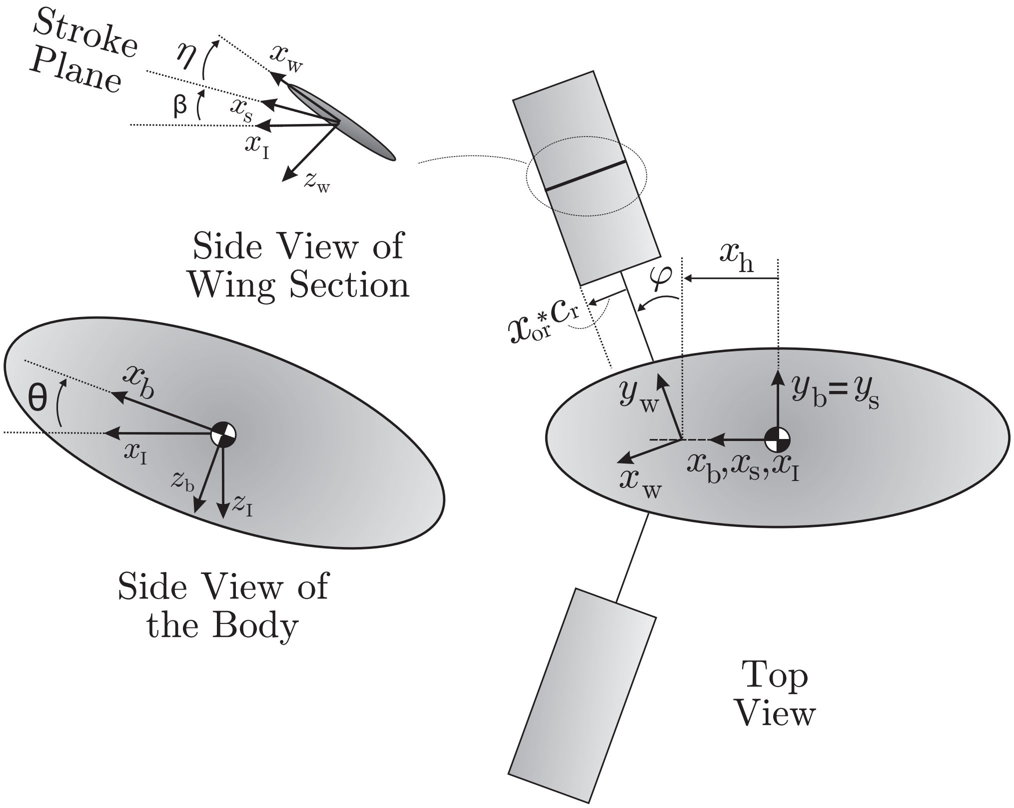

Figure 4.1: A schematic diagram of a FWMAV hovering in a general orientation.

By convention, the x_b-axis points forward defining the vehicle's longitudinal axis, the y_b-axis points to starboard, and the z_b-axis completes the right-handed frame. The conventional yaw-pitch-roll (ψ-θ-ϕ) Euler angle sequence, traditionally used with fixed-wing aircraft [74], is adopted here to describe the body's inertial orientation. Because this effort is focused on longitudinal flight dynamics, only the body's pitch angle θ is required.

The stroke-plane is inclined to the horizontal plane with a stroke plane angle β. That is, the stroke plane reference frame is obtained from the inertial frame through a rotation by an angle β about the y_I-axis. The wing-fixed frame is defined such that it is aligned with the stroke plane frame at zero wing kinematic angles. The wing motion is typically described using three Euler angles: the flapping angle φ (describing back and forth motion along the stroke plane), the plunging angle ϑ (describing out of stroke plane motion), and the pitching angle η (describing rotation of the wing about a chord line). Consistent with observations of biological flyers [124, 77], the plunging motion is neglected ($\vartheta = 0$).

4.2.2 Equations of Motion

Since the two wings move symmetrically, the equations of motion are defined in terms of five generalized coordinates: $\boldsymbol{q} = [x\ ,\ z\ ,\ \theta\ ,\ \varphi\ ,\ \eta]^\intercal$, where $\intercal$ denotes transpose, and x and z are the inertial coordinates of the body center of mass along the x_I and z_I axes, respectively. We use the principle of virtual power [123] to derive the equations of motion

$$\sum_{i=\mathrm{b,w}} [m_i(\dot{\boldsymbol{v}}_i + \ddot{\boldsymbol{\rho}}_{\boldsymbol{c}i}) - \boldsymbol{f}_i] \cdot \frac{\partial \boldsymbol{v}_i}{\partial \dot{q}_j} + [\dot{\boldsymbol{h}}_i + m_i \boldsymbol{\rho}_{\boldsymbol{c}i} \times \dot{\boldsymbol{v}}_i - \boldsymbol{M}_i] \cdot \frac{\partial \boldsymbol{\omega}_i}{\partial \dot{q}_j} = 0,\ j = \{1, ..., 5\},\ (4.1)$$

where m_i is the mass of the i^th rigid body, $\boldsymbol{v}_i$ is the inertial velocity vector of its reference point (the reference points of the body and wing frames are the body's center of gravity and the wing's hinge root, respectively), $\boldsymbol{\rho}_{\boldsymbol{c}i}$ is the vector pointing from the reference point of the i^th rigid body to its center of gravity, $\boldsymbol{\omega}_i$ and $\boldsymbol{h}_i$ are the angular velocity vector of the

i^{th} rigid body with respect to the inertial frame and the corresponding angular momentum vector, respectively, and $\boldsymbol{f}_i$ and $\boldsymbol{M}_i$ are the external force and moment vectors applied on the i^{th} rigid body at its reference point. As such, the equations of motion can be written in an abstract form as

$$\Big[\mathcal{M}(\boldsymbol{q})\Big]\begin{pmatrix}\dot{u}\\ \dot{w}\\ \ddot{\theta}\\ \ddot{\varphi}\\ \ddot{\eta}\end{pmatrix}+\Big(\mathcal{C}(\boldsymbol{q},\dot{\boldsymbol{q}})\Big)=\Big[R_{\text{aero}}\Big]\begin{pmatrix}F_x\\ F_z\\ M_x\\ M_y\\ M_z\end{pmatrix}+\begin{pmatrix}0\\ 0\\ 0\\ 1\\ 0\end{pmatrix}\tau_\varphi+\begin{pmatrix}0\\ 0\\ \cos\varphi\\ 0\\ 1\end{pmatrix}\tau_\eta, \tag{4.2}$$

where $u=\dot{x}$, $w=\dot{z}$ are the body inertial velocity components, $\mathcal{M}(\boldsymbol{q})$ is the inertia matrix, $\mathcal{C}(\boldsymbol{q},\dot{\boldsymbol{q}})$ represents Coriolis and centripetal effects, R_{aero} relates the aerodynamic loads (F_x, F_z, M_x, M_y, and M_z) in the wing frame to the generalized forces, and τ_φ and τ_η are the wing flapping and pitching control torques, respectively. The details of the derivation of Eq. (4.2) are given in Appendix B.

4.2.3 Aerodynamic Model

We extend the aerodynamic model, used in our earlier work [125, 126] which is based on Refs. [127, 128, 129], to a more general setting that is convenient for aerodynamic-dynamic interactions. This model accounts for the dominant contributions (i.e., leading edge vortex (LEV) and rotational contributions) using a quasi-steady, strip theory formulation.

Dickinson et al. [130] showed that for ultra-low Reynolds numbers, where insects operate (Re=200 − 4000), there is almost no stall; the lift has a smooth variation with the angle of attack. Berman and Wang [129] showed that the steady lift coefficient due to a stabilized

LEV can be simply written as

$$C_L = A \sin 2\alpha,$$

where α is the angle of attack. Taha et al. [128] provided a means to estimate the coefficient A in terms of the aspect ratio using the extended lifting line theory [131]. Insects wings, similar to delta wings, experience LEVs, and hence, the flow separates at the leading edge losing the leading edge suction force [67, 128]. As such, the drag is given by $C_D = C_L \tan \alpha$ [67, 128]. Therefore, the resultant aerodynamic force is almost normal to the wing surface (i.e., $C_z = -2A \sin \alpha$). That is, the shear contribution is minimal as shown in the experimental study of Dickinson et al. [130] and the computational results of Wang [132] and Ramamurti et al. [133].

As such, a two-dimensional airfoil undergoing a translational motion with velocity components V_x and V_z in the wing frame and a rotational pitching motion ω_y, as shown in Fig. 4.2, is subjected to the following forces [127, 128, 129]

$$\begin{aligned} F'_x &= \pi \rho c \Delta x V_z \omega_y \\ F'_z &= -\tfrac{1}{2}\rho a_0 c V^2 \sin\alpha - \pi \rho c \Delta x V_x \omega_y \end{aligned}, \tag{4.3}$$

where c is the chord length, Δx is the distance between the pitching axis (hinge line) and the three-quarter chord point, a_0 is the two-dimensional lift curve slope that will be replaced by the three-dimensional lift curve slope when integrating over the whole wing, $V^2 = V_x^2 + V_z^2$, and the angle of attack is given by $\alpha = \tan^{-1}\frac{V_z}{V_x}$. It should be noted that the added mass terms are neglected in Eq. (4.3) because their net effects on the flight dynamics were found to be minimal as shown in our previous effort [125].

To account for aerodynamic-dynamic interaction, the body's motion variables (u, w, and $\dot{\theta}$) and the aerodynamic inputs (V_x, V_z, and ω_y) should be interconnected as shown in Fig. 4.3. As such, the velocity of a wing section that is at a distance r from the wing root is written

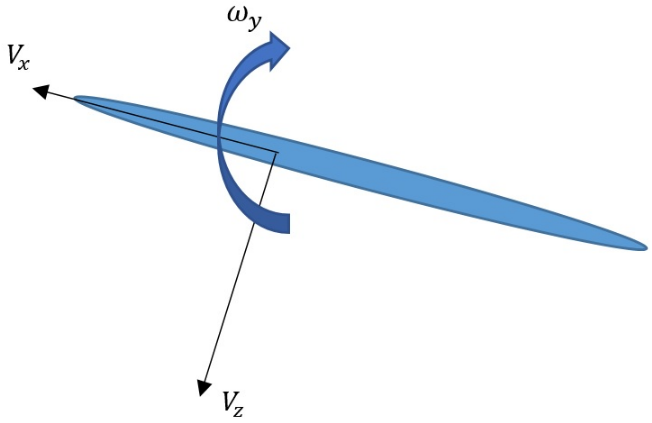

Figure 4.2: A schematic diagram of an airfoil section undergoing translational and rotational motion.

as

$$\boldsymbol{V}^{(\mathrm{w})}(r) = [\boldsymbol{R}_{\mathrm{ws}}][\boldsymbol{R}_{\beta}]\boldsymbol{V}_{\mathrm{w}}^{(\mathrm{I})} + \boldsymbol{\omega}_{\mathrm{w}}^{(\mathrm{w})} \times r\boldsymbol{j}_{\mathrm{w}}, \tag{4.4}$$

where $[\boldsymbol{R}_{\mathrm{ws}}]$ and $[\boldsymbol{R}_{\beta}]$ (given in Appendix B) are the rotation matrices from the stroke plane frame to the wing frame and from the inertial frame to the stroke plane frame, respectively. Also, $\boldsymbol{V}_{\mathrm{w}}^{(\mathrm{I})}$ is the wing velocity vector in the inertial frame, and $\boldsymbol{\omega}_{\mathrm{w}}^{(\mathrm{w})}$ is the wing angular velocity vector in the wing frame. Since the body motion (u, w, and $\dot{\theta}$) is evolving with a quite slower time scale than that of the wing, the term ($V^2 \sin\alpha$) in Eq. (4.3) could be approximated linearly with respect to the body states as follows

$$V^2 \sin\alpha = V^2 \frac{V_z}{|V|} = |V|\, V_z \simeq (|V|\, V_z)\bigg|_0 + \sum_{i=1}^{3} \frac{\partial(|V|\, V_z)}{\partial x_i}\bigg|_{x_i' s=0} \Delta x_i, \tag{4.5}$$

where $x_i's$ are the body states; u, w, and $\dot{\theta}$. Hence, we obtain

$$
\begin{aligned}
V^2 \sin\alpha \;&=\; r^2 \sin\eta \; \dot{\varphi}\,|\dot{\varphi}| + u \,\Big(2\; r \cos\beta \sin\eta \cos\varphi \,|\dot{\varphi}| + r \sin\beta \cos\eta \,|\dot{\varphi}|\Big) + \\
&+\; w \,\Big(r \cos\beta \cos\eta \,|\dot{\varphi}| - 2\; r \sin\beta \sin\eta \cos\varphi \,|\dot{\varphi}|\Big) + \\
&+\; r\; \dot{\theta}\,|\dot{\varphi}| \,\Big(-r \cos\eta \sin\varphi + 2\; x_{\mathrm{h}} \sin\beta \sin\eta \cos\theta \cos\varphi - 2\; x_{\mathrm{h}} \cos\beta \sin\eta \sin\theta \cos\varphi + \\
&-\; x_{\mathrm{h}} \cos\beta \cos\eta \cos\theta - x_{\mathrm{h}} \sin\beta \cos\eta \sin\theta\Big),
\end{aligned}
\tag{4.6}
$$

where x_{h} is the distance from the vehicle's center of mass to the root of the wing hinge line (i.e., the intersection of the hinge line with the x_{b}-axis), as shown in Fig. 4.1.

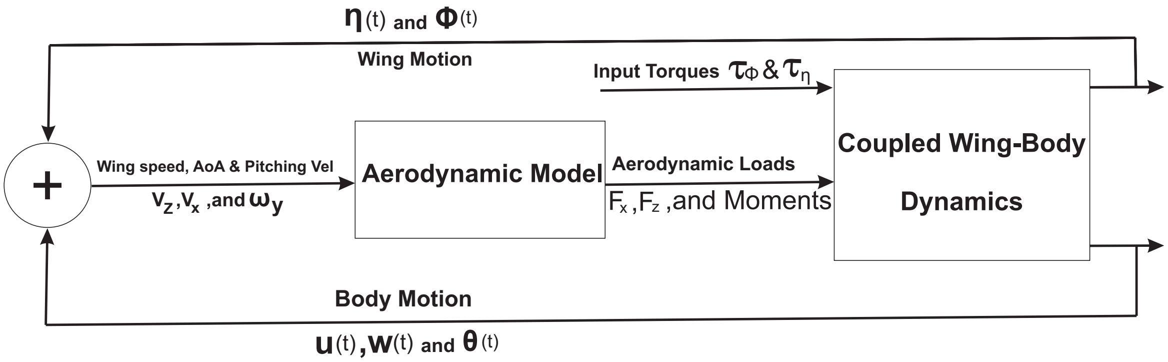

Figure 4.3: A schematic diagram of the aerodynamic-dynamic interaction in a FWMAV.

The time-varying aerodynamic loads (in the wing frame) can then be written as

$$
\begin{pmatrix} F_x(\boldsymbol{x}) \\ F_z(\boldsymbol{x}) \\ M_x(\boldsymbol{x}) \\ M_y(\boldsymbol{x}) \\ M_z(\boldsymbol{x}) \end{pmatrix}
=
\begin{pmatrix} F_{x_0} \\ F_{z_0} \\ M_{x_0} \\ M_{y_0} \\ M_{z_0} \end{pmatrix}
+
\begin{bmatrix} F_{x_u} & F_{x_w} & F_{x_q} \\ F_{z_u} & F_{z_w} & F_{z_q} \\ M_{x_u} & M_{x_w} & M_{x_q} \\ M_{y_u} & M_{y_w} & M_{y_q} \\ M_{z_u} & M_{z_w} & M_{z_q} \end{bmatrix}
\begin{pmatrix} u \\ w \\ \dot{\theta} \end{pmatrix}
+
\begin{pmatrix} F_{x_{nl}} \\ F_{z_{nl}} \\ M_{x_{nl}} \\ M_{y_{nl}} \\ M_{z_{nl}} \end{pmatrix},
\tag{4.7}
$$

where the terms (aerodynamic derivatives) in Eq. (4.7) are given in Appendix C. It should be noted that the aerodynamic derivatives here are not normalized by masses and inertias, in contrast to the conventional aerodynamic derivatives commonly used in flight dynamics literature [74, 134].

As explained above, the aerodynamic loads generated by the wing oscillatory motion are represented as functions of the wing states (φ, η, $\dot{\varphi}$, and $\dot{\eta}$) as well as body states (u, w, θ, and $\dot{\theta}$), in addition to the stroke plane angle β. As such, the interaction between the body motion and the generated aerodynamic loads by the wing can be accounted for, which is explained in Fig. 4.3. For given input torques and aerodynamic loads, the dynamic equations of motion (4.2), or equivalently (B.1–B.5), can be integrated to update the body motion variables (u, w, and θ) and the wing flapping variables (η and φ). Together, they dictate the motion of each airfoil section with respect to the surrounding quiescent air, represented by V_x, V_z, and ω_y. These air speeds, in turn, completely determine the aerodynamic loads according to Eq. (4.3) or (4.7). Accounting for such an interaction between the aerodynamic loads and the body motion allows for a more accurate and heuristic trim and stability analysis.

4.2.4 Two DOF Flight Dynamic Model for Balance Analysis

In this subsection, a two DOF model is extracted from the full five DOF model (4.2). This two DOF model resembles an experimental apparatus where a FWMAV is confined to move along vertical rails, as shown in Fig. 4.4. As such, only two degrees of freedom are considered: the body vertical motion with a velocity w and the wing back and forth flapping angle φ. The wing pitching dynamics is ignored as typically done in FWMAVs when considering a constant pitching angle throughout each half stroke.

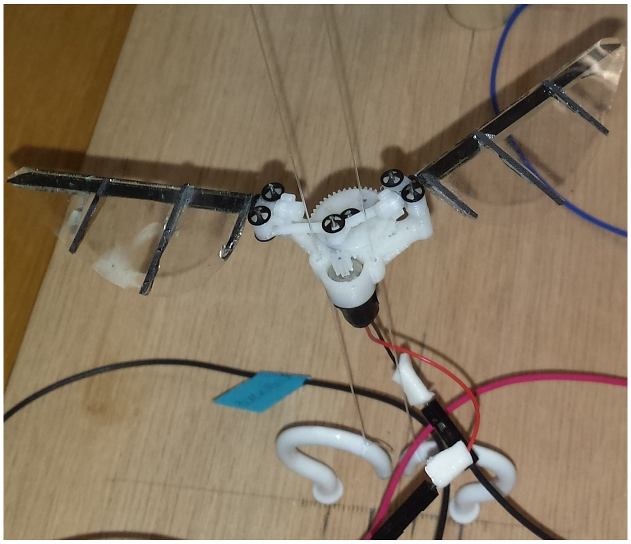

Figure 4.4: Experimental setup of a two DOF FWMAV.

The two DOF FWMAV dynamics can be written as

$$\frac{d}{dt}\begin{bmatrix} z(t) \\ \varphi(t) \\ w(t) \\ \dot{\varphi}(t) \end{bmatrix} = \begin{bmatrix} w(t) \\ \dot{\varphi}(t) \\ g - k_{d_1}\left|\dot{\varphi}(t)\right| w(t) - k_L \dot{\varphi}(t)^2 \\ -k_{d_2}\left|\dot{\varphi}(t)\right| \dot{\varphi}(t) - k_{d_3} w(t)\dot{\varphi}(t) \end{bmatrix} + \begin{bmatrix} 0 \\ 0 \\ 0 \\ \frac{1}{I_F} \end{bmatrix} \tau_{\varphi}(t), \tag{4.8}$$

where g is the gravitational acceleration, I_F is the flapping moment of inertia defined as $I_F = I_{x_\mathrm{w}} \sin^2\alpha_m + I_{z_\mathrm{w}} \cos^2\alpha_m$, and τ_φ is the flapping control input torque. The coefficients k_{d_1}, k_L, k_{d_2}, and k_{d_3} are configuration-dependent parameters and are defined as

$$\begin{aligned} k_{d_1} &= \frac{\rho\ C_{L_\alpha}\ I_{11}\ \cos^2\alpha_m}{2m_v} \\ k_L &= \frac{\rho\ C_{L_\alpha}\ I_{21}\ \sin\alpha_m\cos\alpha_m}{2m_v} \\ k_{d_2} &= \frac{\rho\ C_{L_\alpha}\ I_{31}\ \sin^2\alpha_m}{I_F} \\ k_{d_3} &= \frac{\rho\ C_{L_\alpha}\ I_{21}\ \sin\alpha_m\cos\alpha_m}{I_F}, \end{aligned}$$

where ρ is the air density, C_{L_α} is the wing lift curve slope, α_m is the mean angle of attack maintained throughout the entire stroke, m_v is the total mass of the vehicle, and I_{mn} are constants that depend on the chord distribution of the wing: $I_{mn} = 2\int_0^R r^m c^n(r)\,dr$.

The two DOF system (4.8) can be written abstractly as a typical nonlinear control-affine system

$$\dot{\boldsymbol{x}}(t) = \boldsymbol{Z}(\boldsymbol{x}(t)) + \boldsymbol{Y}(\boldsymbol{x}(t))\ \tau_{\varphi}(t), \tag{4.9}$$

where $\boldsymbol{x}(t) = [z(t) \quad \varphi(t) \quad w(t) \quad \dot{\varphi}(t)]^{\intercal}$ is the state vector. The two DOF system (4.8), or equivalently (4.9), is a NLTP system because the vehicle's weight is balanced by periodic forcing (e.g., $\tau_{\varphi}(t) = U\cos\omega t$). The problem of determining the required amplitude U for balance (i.e., to achieve a specific periodic orbit corresponding to a desired equilibrium, e.g., hovering) is not trivial. For example, Taha et al. [50] refuted the intuitive notion that hovering is achieved by balancing the averaged flapping lift to the weight. Because of the inherent stability of the two DOF system (4.8) due to various damping actions, any deviation from equilibrium will be attributed to unbalance. As such, because of its simplicity and implementation feasibility, the two DOF system (4.8) represents a paradigm for periodic orbit analysis of NLTP systems.

4.2.5 Three DOF Flight Dynamic Model for Balance and Stability Analysis

While the developed model (4.2, 4.7) is amenable to differential-geometric-control tools, we opt to demonstrate such tools on a simpler, yet rich enough, model, not to obscure the details of these tools with the complexity of the full model. In particular, we consider the minimal degrees of freedom required to demonstrate the vibrational pitch stabilization phenomenon. As such, we consider two DOF for the body: body's vertical motion z and pitching angle θ, and one DOF for the wing: the flapping angle φ. The body forward motion is restricted and the wing pitching angle η is assumed to have a piecewise constant variation, commonly used in flapping flight dynamics literature, e.g., [135, 136, 115, 137, 138]

$$\eta(t) = \begin{cases} \alpha_m, & \dot{\varphi} > 0 \\ \pi - \alpha_m, & \dot{\varphi} < 0 \end{cases}.$$

As such, we have $\sin\eta = \sin\alpha_m$ and $\cos\eta = \cos\alpha_m \ \mathrm{sign}(\dot{\varphi})$. This multi-body, three-DOF model resembles (locally at the hovering equilibrium) a lab experiment apparatus [2] that has been developed to verify the results. In this lab experiment, however, the body vertical motion is transformed into pendulum rotation, as shown in Fig. 4.5.

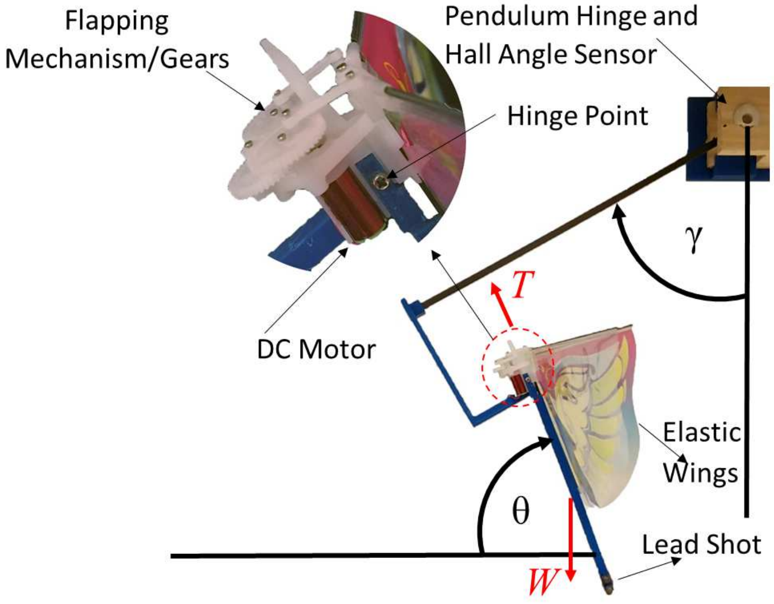

Figure 4.5: The experimental setup developed in [2] to verify the vibrational pitch stabilization phenomenon.

The three DOF model can be written as

$$\mathcal{M}\left(\boldsymbol{q};\ \mathrm{sign}(\dot{\varphi})\right)\ \ddot{\boldsymbol{q}} + \boldsymbol{f}_c(\boldsymbol{q}, \dot{\boldsymbol{q}}) = \boldsymbol{f}_{\mathrm{aero}} + \boldsymbol{g}\ \tau_\phi, \tag{4.10}$$

where $\mathcal{M}$ is the inertia matrix, $\boldsymbol{f}_c$ represents Coriolis and centripetal effects, $\boldsymbol{f}_{\mathrm{aero}}$ represents the aerodynamic loads, $\boldsymbol{g}$ is the input vector field, and τ_ϕ is the input torque. For simplicity, now on, we set the parameter $x_{\mathrm{h}} = 0$ (the distance from the vehicle's center of mass to the root of the wing hinge line). Also, the stroke plane angle in this three DOF model is changed to be measured from the body-fixed frame of reference instead of the inertial frame. As such, $\mathcal{M}$, $\boldsymbol{f}_c$, $\boldsymbol{f}_{\mathrm{aero}}$ and $\boldsymbol{g}$ in system (4.10) are written as

$$\mathcal{M} = \begin{bmatrix} m_{\mathrm{v}} & \mathcal{M}_{12} & \mathcal{M}_{13} \\ \mathcal{M}_{21} & \mathcal{M}_{22} & \mathcal{M}_{23} \\ 0 & 0 & I_{y_{\mathrm{b}}} \end{bmatrix}, \tag{4.11}$$

where

$$\begin{aligned}
\mathcal{M}_{12} &= -r_{\mathrm{cg}} \cos\varphi \sin\theta - \bar{c}\hat{d} \cos\alpha_m \ \mathrm{sign}(\dot{\varphi}) \sin\varphi \sin\theta \\
\mathcal{M}_{13} &= \bar{c}\hat{d} \cos\alpha_m \cos\theta \cos\varphi \ \mathrm{sign}(\dot{\varphi}) - \bar{c}\hat{d} \sin\alpha_m \sin\theta - r_{\mathrm{cg}} \cos\theta \sin\varphi \\
\mathcal{M}_{21} &= -m_{\mathrm{w}} r_{\mathrm{cg}} \cos\varphi \sin\theta - \bar{c}\hat{d} \ m_{\mathrm{w}} \cos\alpha_m \ \mathrm{sign}(\dot{\varphi}) \sin\varphi \sin\theta \qquad\qquad , \\
\mathcal{M}_{22} &= -\tfrac{1}{2} I_{x_{\mathrm{w}}} \cos^2\alpha_m - \tfrac{1}{2} I_{z_{\mathrm{w}}} \sin^2\alpha_m + \tfrac{I_F}{2} + \tfrac{I_{x_{\mathrm{w}}} + I_{z_{\mathrm{w}}}}{2} \\
\mathcal{M}_{23} &= \tfrac{1}{2} I_{y_{\mathrm{w}}} \ \mathrm{sign}(\dot{\varphi}) \sin 2\alpha_m \sin\varphi
\end{aligned}$$

$$\boldsymbol{f}_c = \begin{bmatrix} \begin{gathered} -\dot{\theta}^2\left(\bar{c}\hat{d}\ \sin\alpha_m\cos\theta + \bar{c}\hat{d}\ \cos\alpha_m\sin\theta\ \mathrm{sign}(\dot{\varphi})\cos\varphi - r_{\mathrm{cg}}\sin\theta\sin\varphi\right) + \\ -2\dot{\theta}\dot{\varphi}\left(\bar{c}\hat{d}\cos\alpha_m\cos\theta\ \mathrm{sign}(\dot{\varphi})\sin\varphi + r_{\mathrm{cg}}\cos\theta\cos\varphi\right) + \\ +\dot{\varphi}^2\left(r_{\mathrm{cg}}\sin\theta\sin\varphi - \bar{c}\hat{d}\cos\alpha_m\sin\theta\ \mathrm{sign}(\dot{\varphi})\cos\varphi\right) - g m_{\mathrm{v}} \end{gathered} \\ \\ \begin{gathered} -\dot{\theta}w\left(\bar{c}\hat{d}\ m_{\mathrm{w}}\cos\alpha_m\cos\theta\ \mathrm{sign}(\dot{\varphi})\sin\varphi + m_{\mathrm{w}}r_{\mathrm{cg}}\cos\theta\cos\varphi\right) + \\ +w\dot{\varphi}\left(m_{\mathrm{w}}r_{\mathrm{cg}}\sin\theta\sin\varphi - \bar{c}\hat{d}\ m_{\mathrm{w}}\cos\alpha_m\sin\theta\ \mathrm{sign}(\dot{\varphi})\cos\varphi\right) + \\ +\dot{\theta}^2\Big(\tfrac{1}{2}\cos^2\alpha_m I_{y_{\mathrm{w}}}\sin\varphi\cos\varphi + \tfrac{1}{2}\sin^2\alpha_m(I_{x_{\mathrm{w}}} - I_{z_{\mathrm{w}}})\sin\varphi\cos\varphi + \\ +\tfrac{1}{2}(-I_{x_{\mathrm{w}}} - I_{z_{\mathrm{w}}})\sin\varphi\cos\varphi + \tfrac{1}{2}I_{y_{\mathrm{w}}}\sin 2\varphi\Big) \end{gathered} \\ \\ 0 \end{bmatrix}, \quad (4.12)$$

$$\boldsymbol{f}_{\mathrm{aero}} = \begin{bmatrix} \begin{gathered} -F_x\left(\sin\alpha_m\cos\theta + \cos\alpha_m\sin\theta\ \mathrm{sign}(\dot{\varphi})\cos\varphi\right) + \\ -F_z\left(\sin\alpha_m\sin\theta\cos\varphi - \cos\alpha_m\cos\theta\ \mathrm{sign}(\dot{\varphi})\right) \end{gathered} \\ \sin\alpha_m M_x - \cos\alpha_m M_z\ \mathrm{sign}(\dot{\varphi}) \\ -\cos\alpha_m M_x\ \mathrm{sign}(\dot{\varphi})\sin\varphi + M_y\cos\varphi - \sin\alpha_m M_z\sin\varphi \end{bmatrix}, \qquad (4.13)$$

$$\boldsymbol{g} = \begin{bmatrix} 0 \\ 1 \\ 0 \end{bmatrix}, \qquad (4.14)$$

where F_x, F_z, M_x, M_y, and M_z are the aerodynamic forces and moments represented in the wing frame, as shown in Eq. (4.7), $\bar{c}$ is the mean aerodynamic chord of the wing, and $\hat{d}$ and r_{cg} are the distances from the wing reference point (hinge point at the root section) to the wing center of mass along the negative x_{w}-axis and the y_{w}-axis respectively.

The three DOF model (4.10) is then written in the standard nonlinear control-affine form

$$\dot{\boldsymbol{x}} = \boldsymbol{Z}(\boldsymbol{x}) + \boldsymbol{Y}(\boldsymbol{x})\ \tau_{\varphi}(t), \tag{4.15}$$

where the state vector $\boldsymbol{x}$ is $[\boldsymbol{q} \quad \dot{\boldsymbol{q}}]^{\intercal} = [z \quad \varphi \quad \theta \quad w \quad \dot{\varphi} \quad \dot{\theta}]^{\intercal}$, and the vector fields $\boldsymbol{Z}(\boldsymbol{x})$ and $\boldsymbol{Y}(\boldsymbol{x})$ are written as

$$\boldsymbol{Z}(\boldsymbol{x}) = \begin{bmatrix} \dot{\boldsymbol{q}} \\ \mathcal{M}^{-1}(\boldsymbol{f}_{\mathrm{aero}} - \boldsymbol{f}_{c}) \end{bmatrix}, \qquad \boldsymbol{Y}(\boldsymbol{x}) = \begin{bmatrix} \boldsymbol{0} \\ \mathcal{M}^{-1}\boldsymbol{g} \end{bmatrix}.$$

The geometric control and averaging tools are then combined to rigorously investigate the balance and stability of the NLTP system (4.15) and unravel the unconventional flight dynamic behavior of flapping flight (e.g., vibrational stabilization).

One caveat here is that the averaging theorem requires the NLTP dynamics to be smooth in the states. Unfortunately, both the three DOF and the two DOF systems (4.8, 4.15) are not smooth in the state $\dot{\varphi}$ because of the absolute value function $|\dot{\varphi}|$. In addition, the adopted approximation of the wing pitching angle η results in the existence of the sign function $\mathrm{sign}(\dot{\varphi})$. We tackle both issues by writing $|\dot{\varphi}| = \dot{\varphi}\ \mathrm{sign}(\dot{\varphi})$ and introducing a smooth approximation for the sign function; $\mathrm{sign}(\dot{\varphi}) \approx h(\dot{\varphi}) = (2/\pi)\tan^{-1}(n\ \dot{\varphi})$. We set an appropriate value of n such that, in 1% of the $\dot{\varphi}$ range around the origin, the approximate function $h(\dot{\varphi})$ reaches 99% of the true value (± 1). Alternatively, a hyperbolic tangent sigmoid function could be used as a smooth approximation for the sign function instead of the inverse tangent one. For more details about the adopted smooth approximation, the reader is referred to an earlier work by Taha et al. [139].

4.3 Combined Averaging-Shooting Approach for the Analysis of Flapping Flight Dynamics

In this section, an analysis framework that combines both averaging and periodic shooting approaches is introduced. To focus on balance analysis only first, the reduced-order, two DOF, FWMAV model introduced in Sec. 4.2.4 is considered. Thanks to the inherent stability of the two DOF system (4.8), due to various damping actions, any deviation from equilibrium will be attributed to unbalance. Hence, balance is decoupled from stability and could be scrutinized independently. The averaging techniques introduced in Chapter 2 are applied to the two DOF, multi-body, NLTP FWMAV system (4.8) to perform a mathematically-rigorous analysis for the balance of FWMAVs at hover. That is, the single-body and direct averaging assumptions, that are commonly adopted in analyzing balance and stability of FWMAVs and insects, are relaxed. Moreover, an optimized periodic shooting method is employed to numerically capture the corresponding periodic orbit and verify the obtained results. Finally, we provide a combined averaging-shooting approach for the balance and stability analysis of NLTP systems that (i) unlike typical shooting methods, does not require an initial guess; (ii) provides more accurate results than the analytical averaging approaches, hence relaxing the need for intractable high-order averaged dynamics; and (iii) allows a deeper scrutiny of the system dynamics, in contrast to numerical shooting methods.

4.3.1 Assuming a Prescribed Wing Motion

Ignoring the wing flapping dynamics (i.e., the φ-dynamics) in the two DOF system (4.8) results in the following single DOF system

$$\dot{w}(t) = g - k_{d_1} \left|\dot{\varphi}\right|(t)\; w(t) - k_L\; \dot{\varphi}(t)^2, \tag{4.16}$$

where the flapping angle φ is assumed to follow a cosine wave form: $\varphi(t) = -\Phi \cos \omega t$. By applying first order averaging on the single DOF system (4.16) and solving for the required Φ to achieve hovering, i.e., that makes $\bar{w} = 0$ a fixed point for the averaged dynamics of the system (4.16), we obtain

$$\Phi_{\text{trim}} = \sqrt{\frac{2g}{k_L \omega^2}}, \tag{4.17}$$

which has been derived before by Doman et al. [136] and others.

Figure 4.6 shows a time simulation of the one DOF NLTP dynamics (4.16) with Φ_{trim} determined from (4.17) using the morphological parameters of the hawkmoth insect, given in Appendix F. It is noted from Fig. 4.6 that the system (4.16) indeed goes into the hovering periodic orbit ($\bar{w} = 0$). Therefore, the first order averaging is sufficient to estimate the flapping requirements in the absence of the flapping-wing dynamics.

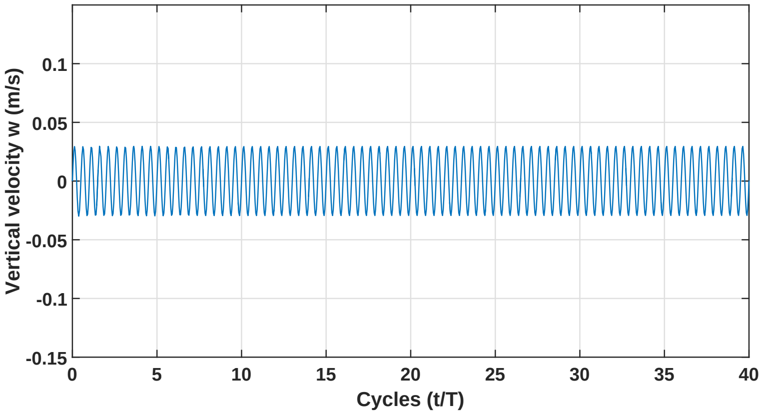

Figure 4.6: Response of the hawkmoth one DOF dynamics (4.16) using Φ_{trim} obtained from (4.17) and an initial condition, $w(0) = 0$.

4.3.2 Effect of Wing Flapping Dynamics

The input to the combined body-flight, wing-flapping two DOF dynamics (4.8) is the flapping torque τ_φ, which is written as

$$\tau_\varphi(t) = U\cos\omega t. \tag{4.18}$$

Clearly, the two DOF system (4.8), or equivalently (4.9), with τ_φ given by (4.18), is not amenable to the averaging theorem (Theorem 1 in Sec. 2.2), i.e., it is not written in the standard averaging form (2.9). The periodic forcing vector field $\boldsymbol{Y}(\boldsymbol{x})\ \tau_\varphi(t)$ is of higher magnitude and faster time scale (i.e., high frequency) than that of the dynamics (drift) vector field $\boldsymbol{Z}(\boldsymbol{x})$. Therefore, averaging theorem cannot be directly applied to system (4.9). In fact, if direct averaging is applied to (4.15), the time-periodic, zero-mean forcing vector field $\boldsymbol{Y}(\boldsymbol{x})\ \tau_\varphi(t)$ would completely vanish. That is, the effects of the flapping-wing dynamics on the body would be completely ignored. In order to resolve this issue, we utilize the nonlinear variation of constants formula, explained in Sec. 2.2. As such, the VOC formula is applied before averaging to obtain the pullback vector field which accounts for the effect of the oscillating forcing vector field on the dynamics (drift) vector filed. That is, the averaged dynamics will be determined from (2.15).

It should be noted that flapping insects, indeed, apply torques at the wing root [140]. Therefore, the current analysis with the assumed simple waveform for the flapping torque is more representative of their natural operation. In contrast, FWMAVs are typically actuated by DC motors or piezo-electric actuators through a drive mechanism where the flapping torque is not the ultimate input to the mechanical system, but rather an intermediate state in the full motor-drive-flapping-body dynamics. Clearly, this full coupling is beyond the scope of this work. The interested reader is referred to the recent effort by Nogar et al. [141], with less emphasis on the higher-order averaging interactions.

VOC Formula with First Order Averaging

Thanks to the mechanical structure of the multi-body, two DOF system (4.8) and because the non-conservative forces (aerodynamic loads) are quadratic in the generalized velocities (w and $\dot{\varphi}$), the integral series of the pullback vector field (2.13) terminates after two terms. Hence, the pullback vector field can be written as

$$\boldsymbol{F}(\boldsymbol{x}(t),t) \quad = \quad \boldsymbol{Z}(\boldsymbol{x}(t)) + [\boldsymbol{Y},\ \boldsymbol{Z}] \int_0^t \tau_\varphi(s_1)\ ds_1 + [\boldsymbol{Y},\ [\boldsymbol{Y},\ \boldsymbol{Z}]] \int_0^t \int_0^{s_1} \tau_\varphi(s_2)\ \tau_\varphi(s_1)\ ds_2\ ds_1. \tag{4.19}$$

The averaging formulas, as defined in (2.17) and (2.18), are then applied to the pullback vector field (4.19) to obtain the first term in the averaging series [142, 143]

$$\boldsymbol{\Lambda_1}(\bar{\boldsymbol{x}}(t)) = \begin{bmatrix} w(t) \\ \\ \dot{\varphi}(t) \\ \\ g - k_L\dot{\varphi}(t)^2 - k_{d_1}w(t)\,|\dot{\varphi}(t)| + \\ + \frac{U^2}{4I_F^2\omega^2}\left(-2k_L - k_{d_1}w(t)\ \mathrm{sign}'(\dot{\varphi}(t))\right) \\ \\ -k_{d_3}w(t)\dot{\varphi}(t) - k_{d_2}\,|\dot{\varphi}(t)|\,\dot{\varphi}(t) + \\ + \frac{U^2}{4I_F^2\omega^2}\left(-2k_{d_2}\ \mathrm{sign}(\dot{\varphi}(t)) - k_{d_2}\dot{\varphi}(t)\ \mathrm{sign}'(\dot{\varphi}(t))\right) \end{bmatrix}. \tag{4.20}$$

The first-order-averaged system (4.20) can be written in terms of the *symmetric product* of the control vector field $\boldsymbol{Y}(\boldsymbol{x})$ as [47], [139]

$$\dot{\bar{\boldsymbol{x}}}(t) = \boldsymbol{Z}(\bar{\boldsymbol{x}}(t)) + \frac{U^2}{4\ \omega^2}\,[\boldsymbol{Y},\ [\boldsymbol{Y},\ \boldsymbol{Z}]]\,(\bar{\boldsymbol{x}}(t)). \tag{4.21}$$

It should be noted that because the assumed cosine waveform for τ_φ satisfies $\int_0^T \int_0^t \tau_\varphi(\sigma)d\sigma dt = 0$, application of the VOC and first-order averaging preserves the mechanical structure of the system as noted from the resulting averaged pullback vector field in Eq. (4.20); the first two equations are simple kinematic equations.

To achieve balance at hover, we solve $\mathbf{\Lambda}_1(\mathbf{0}) = \mathbf{0}$. The third equation implies

$$U_{\text{trim}_{1\text{st}}} = \sqrt{\frac{2\ g I_F^2 \omega^2}{k_L}}, \tag{4.22}$$

while the other three equations are automatically satisfied at the origin. If the torque amplitude U is written in terms of the flapping amplitude Φ as $U = I_F \omega^2 \Phi$, then Eq. (4.22) yields the exact same result for Φ_{trim} as Eq. (4.17). That is, first-order averaging on the single DOF system (4.16), ignoring the wing dynamics, is equivalent to first-order averaging after applying the VOC on the two DOF system (4.8). However, while the direct averaging approach was successful in ensuring hovering for the single DOF case, its equivalent requirements (4.22) in the case of multi-body dynamics is not successful in determining the correct flapping torque amplitude for hover. Figure 4.7 shows the response of the NLTP system (4.8) to the oscillating $\tau_\varphi(t)$ shown in Eq. (4.18) with an amplitude determined from Eq. (4.22) using the morphological parameters of the hawkmoth insect. The insect/FWMAV dynamics goes into a stable periodic orbit that is corresponding to a vertical descent at an average speed of 0.25 m/s. That is, the control input amplitude obtained from Eq. (4.22) is not sufficient to maintain the vehicle in the hovering periodic orbit. Hence, when accounting for the flapping-wing dynamics, direct averaging (even with the aid of the VOC formula) fails to capture important interactions between the two vector fields $\boldsymbol{Y}$ and $\boldsymbol{Z}$; i.e., aerodynamic-dynamic interactions. Therefore, higher order averaging is invoked.

It is interesting to mention that the correct balance requirement can be obtained with the above described procedure but at higher frequencies; that is, as mentioned in Theorem 2, there is a frequency limit (signified by $1/\epsilon^*$) beyond which the obtained periodic orbit for the NLTP system is guaranteed to take values in an open ball of radius $O(1)$ centered at the

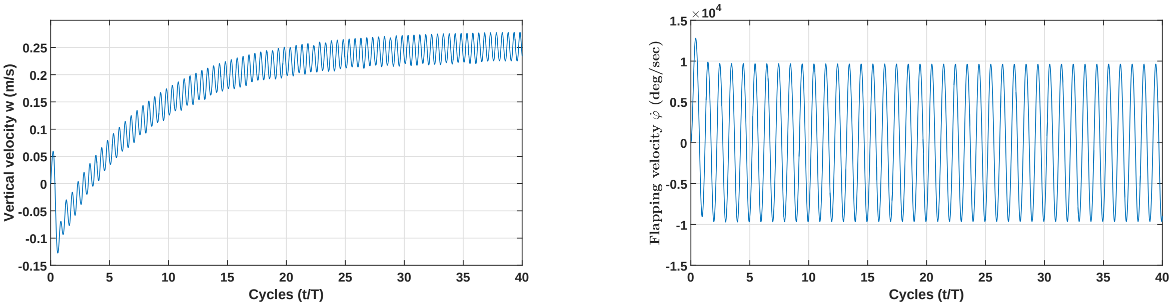

(a) w (b) $\dot{\varphi}$

Figure 4.7: Response of the hawkmoth two DOF dynamics (4.8) using U_{trim} obtained from (4.22) and an initial condition, $\boldsymbol{x}_0 = \mathbf{0}$.

fixed point of the averaged system. To investigate this point more thoroughly, we double the flapping frequency and decrease the mean angle of attack α_m accordingly (almost one fourth) to maintain a similar flapping angle amplitude Φ. In this case, the aerodynamic lift due to flapping is exactly the same. This modification of the flapping parameters while maintaining the aerodynamic lift results in a pure dynamic effect. We use the same formula for flapping torque amplitude, Eq. (4.22), obtained through applying first order averaging after VOC. The resulting NLTP system response is shown in Fig. 4.8. It is noted from Fig. 4.8 that the average vertical velocity is almost zero (i.e., hovering balance is ensured) and the periodic orbit is centered at the fixed point equilibrium (hovering), while $\varphi(t)$ oscillates with a relatively large amplitude.

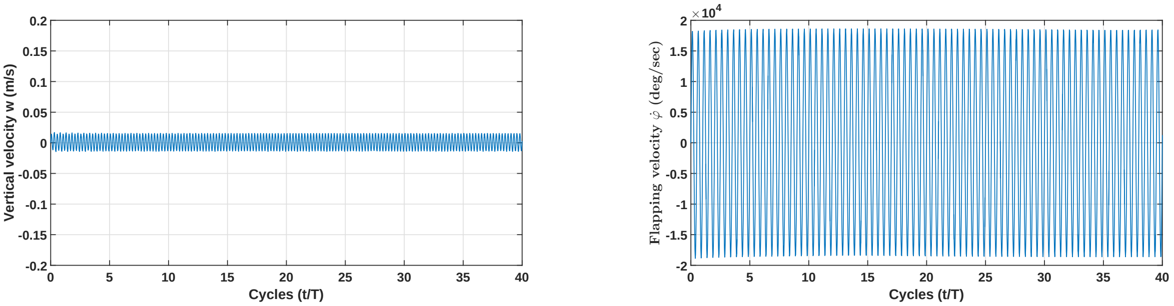

(a) w (b) $\dot{\varphi}$

Figure 4.8: Response of the hawkmoth two DOF dynamics (4.8) at higher flapping frequency (two times the biological value) and lower α_m using U_{trim} obtained from (4.22) and an initial condition, $\boldsymbol{x}_0 = \mathbf{0}$.

VOC Formula with Third Order Averaging

If the frequency limit, dictated by averaging theorems (e.g., Theorem 2), is infeasibly high (e.g., the hawkmoth flapping frequency is below that limit), then the trim result (4.22) obtained through first order averaging after the VOC formula would not be sufficient to ensure the desired equilibrium periodic orbit, as discussed in the previous subsection. Hence, higher order averaging along with the VOC formula would be required. The second order averaging unfortunately yields the same balance requirement, U_{trim}, as given in Eq. (4.22). That is, the second order averaging does not contribute to the balance problem, which invokes third order averaging.

Applying third-order averaging, as shown in Eq. (2.18), on the pullback vector field (4.19), we obtain too lengthy and complicated expressions for the averaged dynamics to show here. Moreover, the mechanical structure is ruined. To explain this point further, recall that the equations of motion of an n-DOF mechanical system are typically represented by n second order differential equations. To represent a mechanical system in a standard first-order form, the first n equations typically define the velocities; i.e., $d\boldsymbol{q}/dt = \dot{\boldsymbol{q}}$ where $\boldsymbol{q}$ represents generalized coordinates (positions and angles). Such a structure may not be maintained under the higher-order averaging process. When it is lost, the balance (trim) problem of the averaged system is quite intricate. Since the first two equations in the third-order-averaged system are not trivial (mechanical structure is not preserved), trim analysis at nonzero $\dot{\bar{\varphi}}$ might be required. As such, a pure analytical solution becomes hard to find. From the multiple solutions of the nonlinear set of algebraic equations for trim, the most feasible numerical solution can be written as [143]

$$U_{\text{trim}_{\text{3rd}}} = 1.0463\sqrt{\frac{2\ g I_F^2 \omega^2}{k_L}}. \tag{4.23}$$

Figure 4.9 shows the simulation of the NLTP dynamics (4.8) of the hawkmoth using the input torque amplitude obtained form Eq. (4.23). The FWMAV's velocity is significantly decreased from 0.25 m/s to 0.02 m/s. That is, the obtained equilibrium is closer to the hovering periodic orbit where w oscillates with a zero mean. This implies the ability of third order averaging to more accurately capture the aerodynamic-dynamic interactions and determine the appropriate balance requirements. However, if more accurate trim results are needed, higher-order averaging (higher than third) would be required, which may be impractical to carry out.

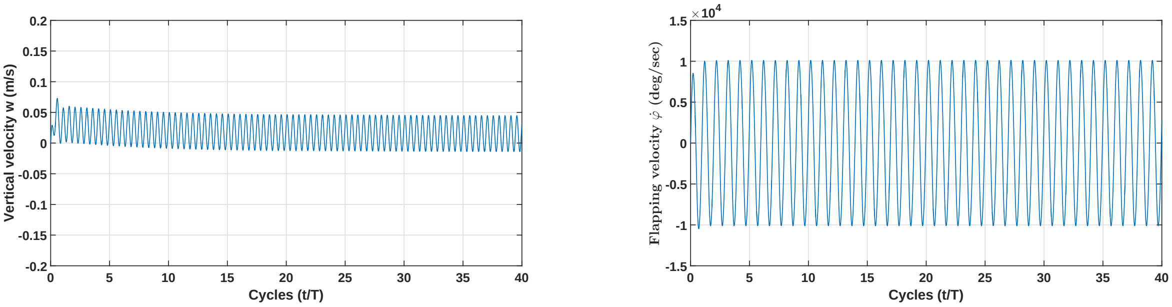

(a) w (b) $\dot{\varphi}$

Figure 4.9: Response of the hawkmoth two DOF dynamics (4.8) using U_{trim} obtained from (4.23) and an initial condition, $\boldsymbol{x}_0 = \mathbf{0}$.

4.3.3 Combining Averaging with Periodic Shooting

In this subsection, we solve for U_{trim} simultaneously with capturing the corresponding periodic orbit. This is achieved through using the optimized shooting technique, explained in Appendix E, to simultaneously obtain the trim requirements to ensure a desired periodic orbit (e.g., hovering) along with capturing the periodic orbit itself. That is, the parameter U_{trim} is considered as an unknown (design variable in the optimization problem) rather than an input to the algorithm and adding one more equation to the residual vector that ensures hovering. More precisely, we require

$$\bar{w} = 0 \quad \Leftrightarrow \quad z(0) = z(T), \tag{4.24}$$

where $\dot{z} = w$. This is equivalent to requesting a periodic solution for the state z representing the vertical displacement of the FWMAV.

Applying the optimized shooting method on the two DOF FWMAV system (4.8) with the additional constraint (4.24), and starting the algorithm with an initial guess for U_{trim} as obtained from averaging approaches ($U_{\text{trim}_{\text{1st}}}$ or $U_{\text{trim}_{\text{3rd}}}$), we obtain the following results [143]

$$\begin{aligned} w(0) &= 0.0177\ m/s \\ \dot{\varphi}(0) &= 50.3857\ rad/s \\ U_{\text{trim}_{\text{exact}}} &= 1.05169\ \sqrt{\frac{2\ gI_F^2\omega^2}{k_L}}. \end{aligned} \tag{4.25}$$

Figure 4.10 shows a time simulation of the NLTP system (4.8) with zero initial conditions and $U_{\text{trim}_{\text{exact}}}$. It is noted from Fig. 4.10 that the system tends rapidly (after around 20 cycles) to an average vertical velocity that is very close to *zero*, i.e., a hovering periodic orbit. Figure 4.11 shows the captured periodic orbit corresponding to $U_{\text{trim}_{\text{exact}}}$. Also, the periodic orbits resulting from the first and third order averaging trim requirement, $U_{\text{trim}_{\text{1st}}}$ and $U_{\text{trim}_{\text{3rd}}}$ respectively, are shown on the same figure for comparison.

One might argue that if the optimized shooting method yields the accurate balance requirements for hovering (an accurate U_{trim}), then the analytical averaging techniques might not be necessary. To address this argument we mention two important points. First, the optimized shooting method explained above is not guaranteed to yield the correct results if it is started at any arbitrary initial guess. The initial guess has to be close enough to the correct result, and this is where the proposed, self-contained, combined averaging-shooting

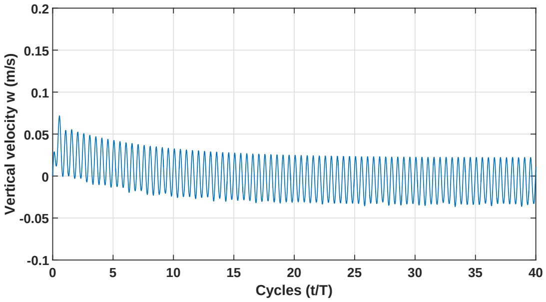

Figure 4.10: Vertical velocity w using $U_{\text{trim}_{\text{exact}}}$ for 40 cycles.

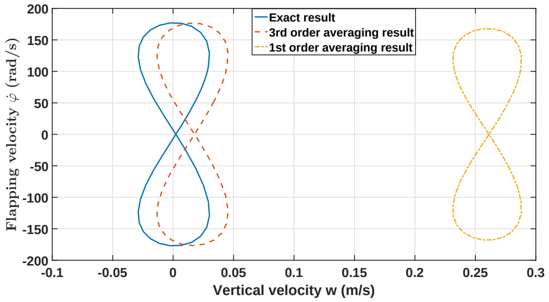

Figure 4.11: The corresponding periodic orbits to $U_{\text{trim}_{\text{exact}}}$, $U_{\text{trim}_{\text{3rd}}}$, and $U_{\text{trim}_{\text{1st}}}$

approach proves its effectiveness. Second, the presented work is a first part of an effort that aims at analyzing not just the balance of FWMAVs but also their stability characteristics. Although FWMAVs stability could be investigated numerically using the Floquet theorem after a periodic orbit is captured, this would only yield a yes/no answer to the stability question without any insights as to why this system has been rendered stable/unstable and what are the stabilizing/destabilizing mechanisms. On the other hand, using the accurate balance requirements obtained from the numerical shooting algorithm and feeding it back to the averaged dynamics, one can gain insights into different stabilizing/destabilizing mechanisms (e.g., positive/negative stiffness) by comparing the entries of the Jacobian of the first- and higher-order averaged dynamics at the ensured equilibrium point. Hence, one can identify potential unconventional stabilizing mechanisms (e.g., vibrational stabilization), as performed by Taha et al. [50] on the single body problem. As such, the proposed approach exploits (i) the accuracy of numerical shooting methods in comparison to the analytical averaging approaches, hence, relaxing the need for intractably high-order averaging, and (ii) the analytical tractability of averaging to scrutinize the dynamical behavior of the system. Finally, Fig. 4.12 summarizes the analysis procedure and results in this section [144, 143].

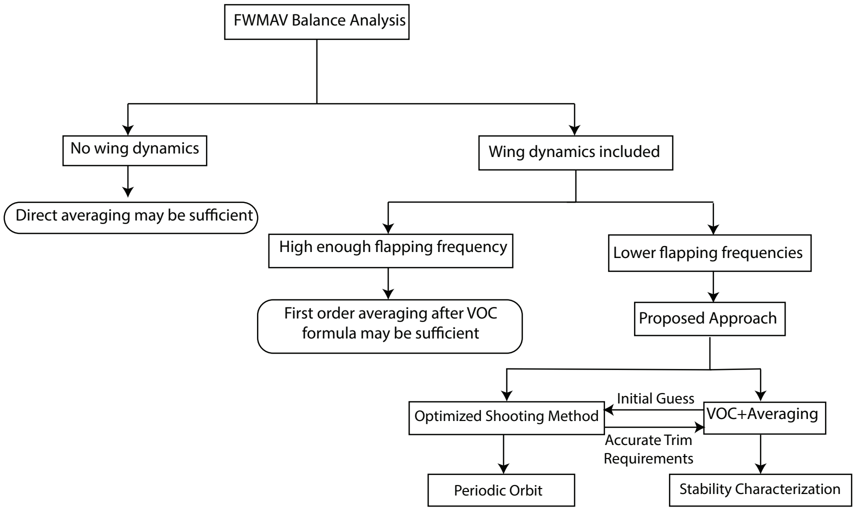

Figure 4.12: A schematic for the analysis procedure and results in this section.

4.4 Balance and Stability Analysis of the Three DOF FWMAV Model

In this section, we use the geometric control and averaging tools explained in Chapter 2 to investigate the balance and stability of the three DOF model derived in Sec. 4.2.5. As explained earlier, the direct application of the averaging theorem to the NLTP system (4.15), with zero-mean τ_φ, yields trivial results (i.e., no effect of flapping on the dynamics). Therefore, the VOC formula is applied before averaging to obtain the pullback vector field (2.13), which accounts for the effects of the forcing vector field on the dynamics (drift) vector filed. That is, the averaged dynamics will be determined from Eq. (2.15). It should be noted that because of the mechanical structure of the system (4.15) and the non-conservative forces (aerodynamic loads) being quadratic in the generalized velocities, the integral series (2.13) of the pullback vector field is expected to terminate after two terms [47]. However, the essentially-high-order smooth approximation of the sign function hinders the termination after two terms in this case. The pullback series of the system (4.15) terminates after three terms and can be written as

$$\begin{aligned} \boldsymbol{F}(\boldsymbol{x},t) &= \boldsymbol{Z}(\boldsymbol{x}) + [\boldsymbol{Y},\ \boldsymbol{Z}] \int_0^t \tau_\varphi(s_1)\ ds_1 + ad^2_{\boldsymbol{Y}} \boldsymbol{Z} \int_0^t \int_0^{s_1} \tau_\varphi(s_2)\ \tau_\varphi(s_1)\ ds_2\ ds_1 \\ &+ ad^3_{\boldsymbol{Y}} \boldsymbol{Z} \int_0^t \int_0^{s_2} \int_0^{s_1} \tau_\varphi(s_3) \tau_\varphi(s_2)\ \tau_\varphi(s_1)\ ds_3\ ds_2\ ds_1, \end{aligned} \tag{4.26}$$

where $ad^n_{\boldsymbol{Y}} \boldsymbol{Z} \equiv [\boldsymbol{Y}, ad^{n-1}_{\boldsymbol{Y}} \boldsymbol{Z}]$.

4.4.1 Balance (Trim)

Unlike the simpler two-DOF model, which has been investigated in the previous section, a simple harmonic waveform ($\tau_\varphi = U \cos \omega t$) for the the flapping torque cannot achieve balance for the three-DOF system (4.10), or equivalently (4.15), where the body pitching angle θ is a state. The reason is that a non-zero mean flapping angle may be required to adjust the center of pressure of the aerodynamic forces with respect to the body center of gravity to achieve pitch trim. Therefore, we suggest writing the input torque $\tau_\varphi(t)$ as

$$\tau_\varphi(t) = U_1 \cos \omega t + U_2 \sin \omega t, \tag{4.27}$$

where the resultant amplitude of the two sinusoids will be denoted by U_R (i.e., $U_\text{R} = \sqrt{U_1^2 + U_2^2}$). Note that this same objective could be achieved by using only one harmonic with a phase shift. However, the adopted form (4.27) is easier to manipulate during the variation of constants and averaging processes.

Using the input waveform in Eq. (4.27), the averaged dynamics (i.e., the averaged pullback vector field (4.26)) is obtained as

$$\dot{\bar{\boldsymbol{x}}} = \bar{\boldsymbol{F}}(\bar{\boldsymbol{x}}) = \boldsymbol{Z}(\bar{\boldsymbol{x}}) + \frac{U_2}{\omega} [\boldsymbol{Y},\ \boldsymbol{Z}](\bar{\boldsymbol{x}}) + \left(\frac{U_1^2 + 3U_2^2}{4\ \omega^2}\right) ad^2_{\boldsymbol{Y}} \boldsymbol{Z}(\bar{\boldsymbol{x}}) + \left(\frac{31 U_1^2 U_2 + 5U_2^3}{12\ \omega^3}\right) ad^3_{\boldsymbol{Y}} \boldsymbol{Z}(\bar{\boldsymbol{x}}). \tag{4.28}$$

In order to achieve balance at hovering, we solve for the trim input torque amplitudes, $U_{1_{\mathrm{t}}}$ and $U_{2_{\mathrm{t}}}$, along with a fixed point $\bar{\boldsymbol{x}}_0$ that ensure $\dot{\boldsymbol{x}} = \mathbf{0}$. Now on, we consider the hawkmoth insect for this analysis whose morphological parameters are given in Appendix F. As such, we obtain

$$\begin{aligned} U_{1_{\mathrm{t}}} &= 0.97\, U^{\dagger} \\ U_{2_{\mathrm{t}}} &= 0.24\, U^{\dagger} \\ \bar{\boldsymbol{x}}_0 &= [0 \quad 7.12^{\circ} \quad 0 \quad 0 \quad 0 \quad 0]^{*} \end{aligned} , \tag{4.29}$$

where the subscript t denotes trim/balance condition at hover, $U^{\dagger}$ is the input torque amplitude needed to balance the two DOF model at hover using a simple harmonic waveform, and is equal to $U_{\mathrm{trim}_{1\mathrm{st}}}$ in Eq. (4.22).

It should be noted that the resultant trim input torque amplitude ($U_{\mathrm{R_t}} = \sqrt{U_{1_{\mathrm{t}}}^2 + U_{2_{\mathrm{t}}}^2}$) is equal to $U^{\dagger}$. That is, the flapping torque amplitude required to maintain the hovering equilibrium for the considered three DOF system (4.15) is the same as that of the previously-analyzed two DOF system in Sec. 4.3; only phase shift is required to achieve pitch trim as explained earlier.

4.4.2 Stability Analysis

Now, that balance/trim at the hovering equilibrium has been ensured for the averaged system (4.28), a linearized version of the averaged dynamics could be obtained at the hovering fixed point (4.29). Having an LTI version of the NLTP system (4.15) at hover would: (i) significantly simplify stability analysis: it can be analyzed by checking eigenvalues; and (ii) allow us to obtain analytical (or semi-analytical) results and gain insights into various stabilizing/destabilizing mechanisms.

To obtain an LTI representation of the NLTP dynamics (4.15), we evaluate the Jacobian matrix, $\boldsymbol{A}$, of the averaged nonlinear dynamics (4.28) at the hovering trim point ($U_{1_\mathrm{t}} = 0.97\, U^\dagger,\ U_{2_\mathrm{t}} = 0.24\, U^\dagger,\ \bar{z} = 0,\ \bar{\varphi} = 7.12°,\ \bar{\theta} = 0,\ \bar{w} = 0,\ \dot{\bar{\varphi}} = 0,\ \dot{\bar{\theta}} = 0$). As such, we obtain

$$\frac{d}{dt}\begin{pmatrix} \bar{z} \\ \bar{\varphi} \\ \bar{\theta} \\ \bar{w} \\ \dot{\bar{\varphi}} \\ \dot{\bar{\theta}} \end{pmatrix} = [\boldsymbol{A}](\bar{\boldsymbol{x}}) = \begin{bmatrix} 0 & 0 & 0 & 1 & 0 & 0 \\ 0 & 0 & 0 & 0 & 1 & 0 \\ 0 & 0 & 0 & 0 & 0 & 1 \\ 0 & -0.19 & 4.7 & -4.05 & 0.0002 & 0.1 \\ 0 & -19 & -621.98 & -0.85 & -9.55 & 0.005 \\ 0 & 6093 & -72.96 & 269.22 & -5.42 & -1.54 \end{bmatrix} \begin{pmatrix} \bar{z} \\ \bar{\varphi} \\ \bar{\theta} \\ \bar{w} \\ \dot{\bar{\varphi}} \\ \dot{\bar{\theta}} \end{pmatrix}, \tag{4.30}$$

where $[\boldsymbol{A}] = \left[\frac{\partial \bar{\boldsymbol{F}}}{\partial \bar{\boldsymbol{x}}}\right]\Big|_{\bar{\boldsymbol{x}}_0}$.

Investigating the eigenvalues of the linearized system (4.30), we find

$$\text{eigenvalues}(\boldsymbol{A}) = -33.85 \pm 31.9\ \text{i},\ 28.31 \pm 30.8\ \text{i},\ \ -4.05,\ 0,$$

which indicates an unstable averaged system due to the complex-conjugate pair ($28.31 \pm 30.8\, i$) having positive real parts. This implies that a feedback control would be needed to stabilize this system at the hovering equilibrium. This result is consistent with many of the previous analyses in the literature [113, 114, 109, 145, 125, 146] that concluded the hovering equilibrium of FWMAVs/insects to be open-loop unstable.

4.4.3 Stability Characterization

Thanks to the simultaneous analytical tractability and mathematical rigor of the geometric-control-averaging tools, the stability of the NLTP system (4.15) could be investigated on a deeper level through scrutinizing the correspondent LTI system. The linearization of the averaged system (4.28) at the hovering fixed point $\bar{\boldsymbol{x}}_0$ can be written abstractly as

$$\boldsymbol{A} = \left.\frac{\partial \bar{\boldsymbol{F}}}{\partial \bar{\boldsymbol{x}}}\right|_{\bar{\boldsymbol{x}}_0} = \begin{bmatrix} 0 & 0 & 0 & 1 & 0 & 0 \\ 0 & 0 & 0 & 0 & 1 & 0 \\ 0 & 0 & 0 & 0 & 0 & 1 \\ 0 & A_{42} & A_{43} & A_{44} & A_{45} & A_{46} \\ 0 & A_{52} & A_{53} & A_{54} & A_{55} & A_{56} \\ 0 & A_{62} & A_{63} & A_{64} & A_{65} & A_{66} \end{bmatrix}, \tag{4.31}$$

where the analytical expressions of the elements of the matrix $\boldsymbol{A}$ are shown in detail in Appendix D.

Since the open-loop instability at the hovering equilibrium of FWMAVs/insects has been attributed mostly to the lack of body pitch stiffness [113, 114, 109, 145, 125, 146]. It is of great interest to scrutinize the stability derivative A_{63} which represents body pitch stiffness: it corresponds to a pitching moment resulting from a pitch angle disturbance. The stability derivative A_{63} can be analytically written as

$$\begin{aligned} A_{63} = \frac{1}{I_F^2 I_{y_b} m_{\mathrm{v}} \omega^2} C_{L_\alpha} m_{\mathrm{w}} \rho \cos\alpha_m \Bigg(\cos\alpha_m \Bigg(\bar{c}\hat{d} \Bigg(I_{11} k \left(-5.23 I_F U_2 \omega + 0.06 U_1^2 + 0.18 U_2^2 \right) + \\ + I_{12} \left(3.9 I_F U_2 \omega - 0.05 U_1^2 - 0.14 U_2^2 \right) \Bigg) + \bar{c}\hat{d} I_{21} \cos\alpha_m \left(U_2 (0.02 U_2 - 2.4 I_F \omega) + 0.01 U_1^2 \right) + \\ + I_{21} r_{\mathrm{cg}} \left(U_2 (0.18 U_2 - 19.27 I_F \omega) + 0.06 U_1^2 \right) \Bigg) + r_{\mathrm{cg}} \Bigg(I_{11} k \left(U_2 (1.48 U_2 - 41.88 I_F \omega) + 0.49 U_1^2 \right) + \\ + I_{12} \left(U_2 (31.4 I_F \omega - 1.1 U_2) - 0.37 U_1^2 \right) \Bigg) \Bigg). \end{aligned}$$

Considering the hawkmoth parameters, we find $A_{63} = -72.96$ as shown in Eq. (4.30). The negative sign indicates a restoring pitching moment under a pitch angle perturbation from the equilibrium, hence a stabilizing pitch stiffness. This result revises the community's belief. That is, the natural (open-loop) longitudinal flight dynamics possesses a stabilizing body pitch stiffness mechanism [147].

To investigate the main contributors to this pitch stiffness mechanism, we write the averaged dynamics in terms of its two components: the dynamics vector field $\boldsymbol{Z}$ and the Lie brackets between the dynamics and control vector fields (i.e., control effects), as shown in Eq. (4.28). As such, the Jacobian matrix $\boldsymbol{A}$ can be considered as an addition of two matrices $\boldsymbol{A}_{\mathrm{d}}$ and $\boldsymbol{A}_{\mathrm{c}}$, where

$$\begin{aligned} \boldsymbol{A}_{\mathrm{d}} &= \left.\frac{\partial}{\partial \bar{\boldsymbol{x}}}\right|_{\bar{\boldsymbol{x}}_0} \left(\boldsymbol{Z} \right) \\ \boldsymbol{A}_{\mathrm{c}} &= \left.\frac{\partial}{\partial \bar{\boldsymbol{x}}}\right|_{\bar{\boldsymbol{x}}_0} \left(\frac{U_2}{\omega} \left[\boldsymbol{Y},\ \boldsymbol{Z} \right] + \left(\frac{U_1^2 + 3U_2^2}{4\ \omega^2} \right) ad_{\boldsymbol{Y}}^2 \boldsymbol{Z} + \left(\frac{31 U_1^2 U_2 + 5 U_2^3}{12\ \omega^3} \right) ad_{\boldsymbol{Y}}^3 \boldsymbol{Z} \right) \end{aligned}, \tag{4.32}$$

where the subscripts d and c refer to dynamics and control, respectively. Hence, the effect emanating from each source can be shown separately. We find that, as maybe expected, $A_{\mathrm{d}_{63}} = 0$. Hence, the pitch stiffness emanates solely from flapping actuation. This fact implies that the high-frequency periodic forcing applied on the wings induces a stabilizing effect on the slower body pitching motion. That is, this pitch stiffness mechanism relies essentially on the vibrational stabilization phenomenon.

It should be noted that the pitch stiffness term A_{63} stems from a combined inertial-aerodynamic root; i.e.,

$$\lim_{m_{\mathrm{w}} \to 0} A_{63} = 0 \quad \text{and} \quad \lim_{C_{L_\alpha} \to 0} A_{63} = 0.$$

The pitch stiffness term A_{63} can be abstractly written as

$$A_{63} = k_{63}\ m_{\mathrm{w}} \cos \bar{\phi}_0 M_{y_w}^{(I)},$$

where k_{63} is a function of the vehicle parameters and the flapping torque amplitude and frequency, $\bar{\phi}_0$ is the average flapping angle at the trim condition (4.29), and $M_{y_w}^{(I)}$ is an aerodynamic derivative that represents a pitching moment in the inertial frame due to a disturbance in the vertical velocity w. For an intuitive explanation of this pitch stiffness mechanism and the role of wing inertia, consider a body pitch up disturbance $\Delta\theta$. This pitch disturbance causes a change of the lift force vector direction, which, in turn, results in a deficit in the lift force needed for balance. Hence, a downward vertical velocity disturbance Δw would be generated. The vertical velocity disturbance Δw can be written as an addition of two components: $\Delta w = \Delta\bar{w} + \Delta\tilde{w}$, where $\Delta\bar{w}$ is the cycle-average and $\Delta\tilde{w}$ is a zero-mean oscillatory component because of the fast time-scale of the wing dynamics. Due to the aerodynamic derivative $M_{y_w}^{(I)}$, a pitching moment is generated as a consequence of Δw. The derivative $M_{y_w}^{(I)}$ can be decomposed similarly: $M_{y_w}^{(I)} = \bar{M}_{y_w} + \tilde{M}_{y_w}$. As such, the resulting pitching moment $\Delta M_y^{(I)} = M_{y_w}^{(I)}\Delta w$ will have three contributions: (i) $\bar{M}_{y_w}\Delta\bar{w}$ which is captured by direct averaging; (ii) $\bar{M}_{y_w}\Delta\tilde{w} + \tilde{M}_{y_w}\Delta\bar{w}$ whose net effect cancel over the flapping cycle (zero mean); and (iii) $\tilde{M}_{y_w}\Delta\tilde{w}$ which is the multiplication of two zero-mean terms and will have a non-zero mean value if the variations of these two terms are synchronized. It should be noted that the last contribution is clearly due to the oscillation (vibration) of the system characteristics (i.e., the multi-time-scale nature of the system); it is typically neglected by direct averaging. The wing inertial effects promote the last contribution, $\tilde{M}_{y_w}\Delta\tilde{w}$, through amplifying $\Delta\tilde{w}$ resulting from a pitch disturbance. This effect can be seen from the $\dot{w}$ equation in the three DOF NLTP system, i.e., the fourth line in Eq. (4.15). The right hand side of that line contains terms like the following: $m_\mathrm{w} r_\mathrm{cg}\dot{\theta}\dot{\varphi}\cos\theta\cos\varphi$; $m_\mathrm{w} r_\mathrm{cg}\dot{\theta}^2\sin\theta\sin\varphi$; $m_\mathrm{w}\bar{c}\hat{d}\cos\alpha_m\dot{\theta}\dot{\varphi}\cos\theta\sin\varphi\mathrm{sign}(\dot{\varphi})$; and $m_\mathrm{w}\bar{c}\hat{d}\cos\alpha_m w\dot{\theta}\cos\theta\sin\varphi\mathrm{sign}(\dot{\varphi})$. This implies that these terms are producing body's vertical velocity through an interaction between the wing inertial effects and the body pitch angle/rate. Therefore, any first order analysis that neglects the wing inertial effects would yield a zero pitch stiffness for the body.

4.4.4 Averaging-Aided Shooting-Floquet Analysis

Although the adopted approach (applying the VOC formula first to the NLTP system and then averaging over the flapping cycle) captures a wide range of aerodynamic-dynamic interactions, it is still an approximation of the true time-periodic. Thus, there are some phenomena that are not very well captured in the averaged dynamics sense. One important aspect is the effect of the wing-body interactions on the generated lift over the cycle. That is, an averaged lift over the flapping cycle that is equal to the weight of the vehicle may not be enough for balance. This phenomenon has been referred to as a *negative lifting mechanism* in an earlier work by Taha et al. [139]. This phenomenon, in turn, affects stability since balance and stability are coupled in this problem. That is, if the flapping input torque amplitudes are not enough to ensure balance at hover, the vehicle will be deviating from its hovering periodic orbit (or fixed point in the averaged sense).

Therefore, in this subsection, a time-periodic analysis will be performed by using the averaging analysis results as an initial guess for an optimized periodic shooting method [148]. This shooting method is used to determine the hovering periodic orbit of the three DOF system (4.15) simultaneously with more accurate (i.e., accounts for the negative lifting mechanism) values of the trim input torque amplitudes (U_{1_t}, U_{2_t}). This procedure has been proposed and applied on a simpler model in the previous section. The Floquet theorem [149] is then used to analyze stability of the captured hovering periodic orbit. In the Floquet stability analysis, the NLTP dynamics (4.15) is linearized about the numerically-captured periodic orbit, yielding a linear time-periodic (LTP) system. The stability of the obtained LTP system is then analyzed through investigating the monodromy matrix: the state transition matrix evaluated after one period T. The eigenvalues of the monodromy matrix (also called Floquet multipliers) have to be inside the unit disk (in the complex plane) for the periodic orbit to be stable. The Floquet multipliers could then be transformed into Floquet exponents, which represent eigenvalues of the corresponding continuous LTI system. That is, a positive-real-part Floquet exponent implies instability. Therefore, the obtained Floquet exponents will be used to construct a comparison against the averaging stability results obtained in Sec. 4.4.2.

Feeding the trim input torque amplitudes (U_{1_t}, U_{2_t}) from Eq. (4.29) as an initial guess to the optimized periodic shooting, we obtain the following point on the hovering periodic orbit along with the associated trim input torque amplitudes

$$\begin{aligned} \varphi(0) &= -1.1\ rad, \quad \theta(0) = 0.11\ rad, \quad w(0) = -0.01\ m/s \\ \dot{\varphi}(0) &= -0.74\ rad/s, \quad \dot{\theta}(0) = 5.29\ rad/s \\ U_{1_{\mathrm{tn}}} &= 1.02\ U^{\dagger}, \quad U_{2_{\mathrm{tn}}} = 0.07\ U^{\dagger}, \end{aligned} \tag{4.33}$$

where the subscript n in $U_{1_{\mathrm{tn}}}, U_{2_{\mathrm{tn}}}$, refers to the numerical optimized shooting method. Investigating the resultant trim amplitude, we find $U_{\mathrm{R_{tn}}} = \sqrt{U_{1_{\mathrm{tn}}}^2 + U_{2_{\mathrm{tn}}}^2} = 1.0225\ U^{\dagger}$. That is, the resultant trim amplitude from the optimized shooting is slightly higher than that of averaging. This result conforms with the previous findings for the two DOF model in Sec. 4.3 that averaging may not very well capture the negative lifting phenomenon (i.e., averaging underestimates the required flapping torque to ensure hovering). Figure 4.13 shows the periodic orbit corresponding to the initial conditions and trim input torque amplitudes in (4.33).

To investigate stability, the NLTP dynamics (4.15) is linearized about the captured hovering periodic orbit (4.33). The Floquet multipliers for the obtained LTP system are found to be

$$0.69 \pm 1.99i, \ 0.11 \pm 0.22i, \ 0.87, \ 0,$$

which also indicates an unstable hovering periodic orbit due to the existence of the complex-conjugate pair ($0.69 \pm 1.99i$) outside the unit disk. Figure 4.14 shows the Floquet exponents corresponding to the above Floquet multipliers along with the eigenvalues from averaging for comparison [147]. Both techniques yield similar stability characteristics: an unstable oscillatory mode, a stable oscillatory mode, a stable eigenvalue on the real line, and a neutral (zero) eigenvalue. Note that the zero eigenvalue corresponds to the ignorable coordinate z in both cases.

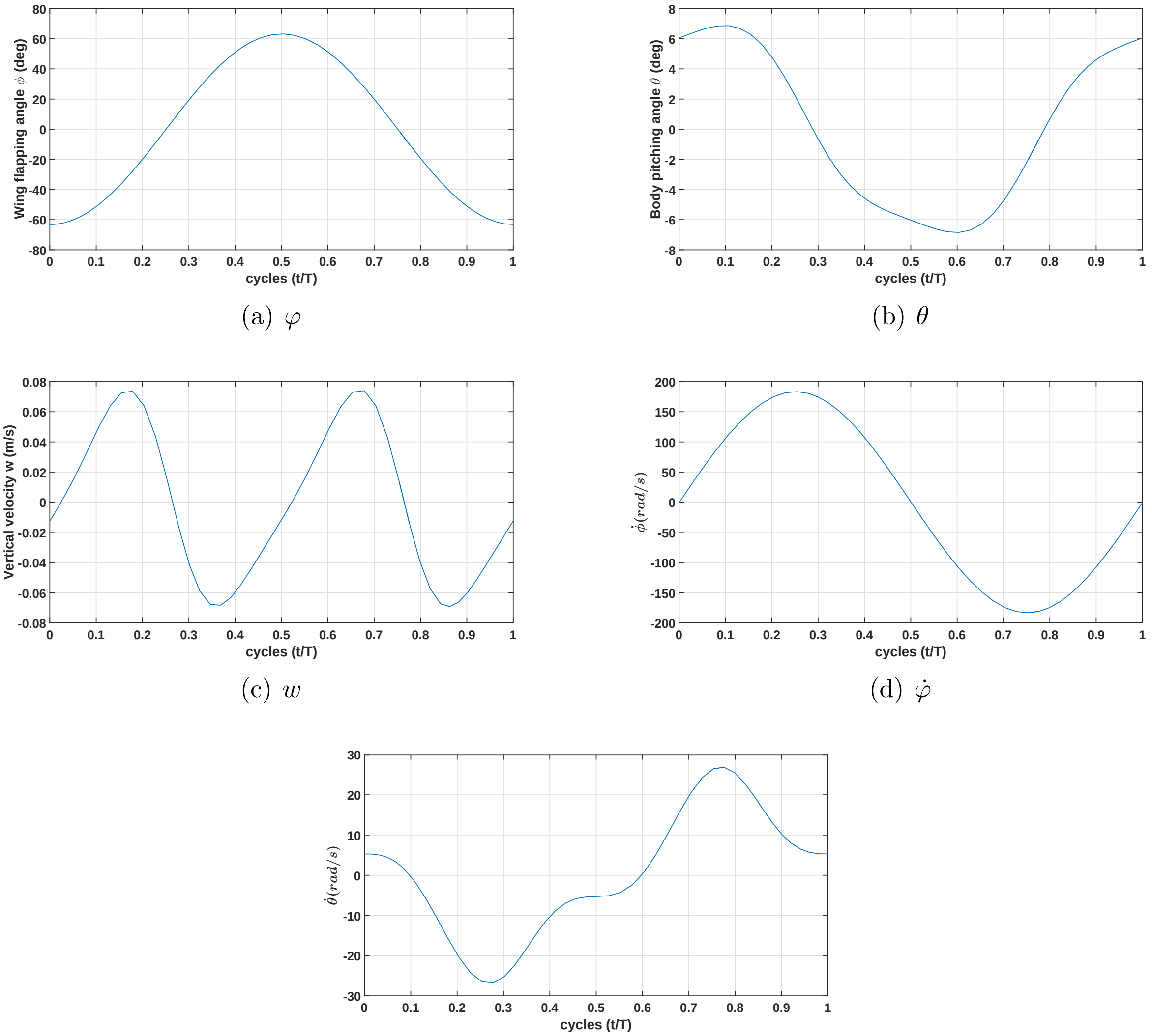

(a) φ

(b) θ

(c) w

(d) $\dot{\varphi}$

(e) $\dot{\theta}$

Figure 4.13: The captured hovering periodic orbit (4.33) for the NLTP system (4.15) under the input waveform (4.27) and using the hawkmoth parameters.

4.4.5 Effects of High Flapping Frequency

It is well-known that the vibrational pitch stabilization phenomenon is intimately tied to high-frequency periodic forcing [25, 28, 30, 29]. Therefore, the effect of flapping frequency on stability of the NLTP system (4.15) is investigated in this subsection.

Considering a flapping frequency that is ten times the documented value for the hawkmoth, the captured hovering periodic orbit is found to have the following trim input torque ampli-

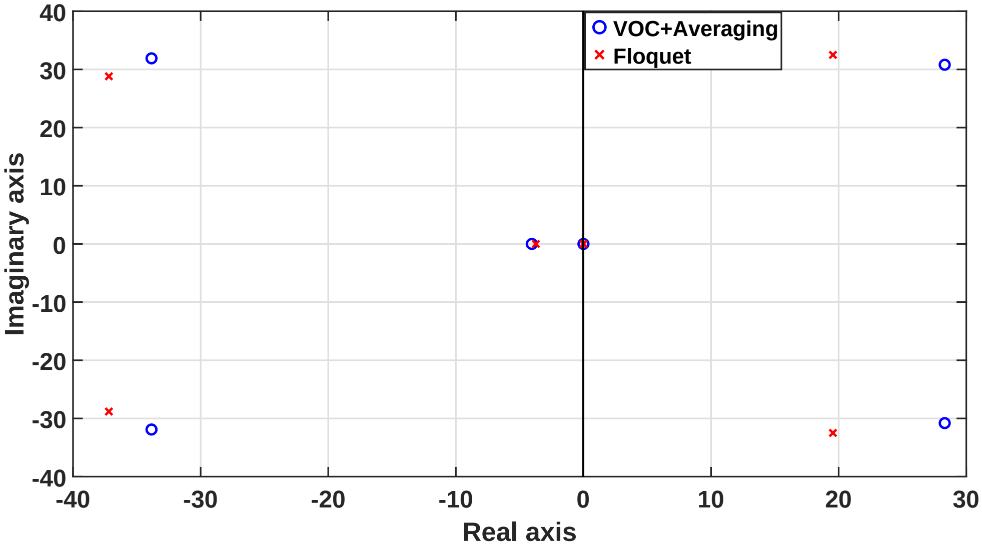

Figure 4.14: Eigenvalues determining the stability of the NLTP system (4.15) for the hawkmoth case using averaging and Floquet theorem.

tudes

$$\begin{aligned} U^{\mathrm{hf}}_{1_{\mathrm{tn}}} &= 1.00\ U^{\dagger} \\ U^{\mathrm{hf}}_{2_{\mathrm{tn}}} &= 0.01\ U^{\dagger} \end{aligned}, \tag{4.34}$$

where the superscript hf denotes high frequency. It is noted that the resultant amplitude $U^{\mathrm{hf}}_{\mathrm{R}_{\mathrm{tn}}} = 1.00032\ U^{\dagger}$, which is less than that of the original flapping frequency and closer to the averaging one. This implies that the negative lifting mechanism effects tends to diminish as the flapping frequency increases, hence the closeness to the averaging result. This, in fact, conforms with the averaging theorem statement that the averaging results are valid for high enough frequency. That is, the averaging results become more representative of the physical (time-periodic) system at higher frequencies.

The obtained Floquet multipliers for this high-frequency periodic orbit are

$$1.1055 \pm 0.1297i,\ 0.8745 \pm 0.1074i,\ 0.9849, 0,$$

whose unstable pair ($1.1055 \pm 0.1297i$) shifts towards the stable region. This indicates that the higher flapping frequency amplifies the effect of the vibrational pitch stabilization mechanism. However, to achieve passive (open-loop) stability, a change in the vehicle parameters (e.g., wing mass, wing size, hinge location, etc.) maybe required.

4.4.6 Comparison with the Corresponding Single-Body Model

One legitimate question that needs to be addressed is: Can direct averaging (which is essentially less rigorous) capture such stabilizing effects? Realizing that direct averaging of the NLTP system (4.15) would yield trivial results (completely ignoring the flapping effects), the simplest non-trivial analysis, avoiding differential geometric tools (e.g., VOC), would have to ignore the flapping dynamics and assume a waveform for the flapping angle $\varphi(t)$ as if the flapping wing is controlled by a fast servo mechanism. This analysis essentially neglects the multi-body nature of the problem (i.e., a single body problem). Therefore, it is interesting to investigate the differences between the three DOF model (4.15) and the single-body version of it. In the latter, the VOC formula would not be needed. After applying direct averaging to the single-body version of the three DOF system (4.15) and linearizing the resulting NLTI system, we obtain the following Jacobian matrix

$$\frac{d}{dt}\begin{pmatrix}\theta \\ w \\ \dot{\theta}\end{pmatrix} = [A_{sb}](\boldsymbol{x}_{sb}) = \begin{bmatrix} 0 & 0 & 1 \\ 0.01 & -0.15 & 0 \\ 0 & -0.03 & -0.88 \end{bmatrix}\begin{pmatrix}\theta \\ w \\ \dot{\theta}\end{pmatrix}, \tag{4.35}$$

where the state vector is $\boldsymbol{x}_{sb} = [\theta \quad w \quad \dot{\theta}]^\intercal$. It should be noted that the pitch stiffness, the element (3, 1), is *zero*, whereas in the multi-body averaged system (4.30), the pitch stiffness has a significant value (-72.96). This implies that the discovered pitch stiffness mechanism is essentially induced due to the mutual interactions between the body and wing dynamics [147]. That is, such a mechanism is revealed only when the wing flapping dynamics is included and/or higher-order averaging is used.

4.5 Conclusion

In this chapter, the full multi-body, nonlinear, longitudinal, flight dynamics of FWMAVs are formulated and cast in a differential-geometric-control framework. We relaxed the two common assumptions (neglecting wing inertia and performing direct-averaging) usually adopted in the balance and stability analysis of FWMAVs and insects. We noted that while direct averaging provides non-trivial results, though inaccurate, when ignoring the wing inertial effects, it completely fails if this assumption is relaxed; it neglects the entire flapping effects. To overcome this predicament, we provided a mathematically rigorous analysis for the balance and stability of FWMAVs by combining tools from chronological calculus, geometric control, and averaging.

On the other hand, an optimized shooting method was adopted to numerically capture the resulting periodic orbits. To circumvent providing an accurate initial guess as needed by shooting methods, we proposed combining the averaging approach with the shooting method; the result of first-order averaging after the VOC formula is a convenient initial guess. The shooting method was then used to determine a more accurate estimate for the hovering balance flapping requirements than those resulting from higher-order averaging. Moreover, these requirements (flapping parameters) can then be fed to the analytically determined higher-order averaged dynamics to scrutinize the dynamical behavior of the system for discovery of potential unconventional stabilizing mechanisms (vibrational stabilization).

The most important finding of this effort is that the high-frequency periodic forcing on FWMAVs/insects induces vibrational stabilization mechanisms to their relatively slow body dynamics. These stabilizing mechanisms are mainly due to the interaction between the aero-inertial loads on the flapping wings due to the fast flapping motion and those due to the slow body motion: what we call aerodynamic-dynamic interaction. The main conclusion is that this interaction is instrumental for the open-loop stability analysis of such nonlinear time-periodic systems. Moreover, it cannot be captured by direct averaging or without accounting for the wing flapping dynamics. Therefore, the differential-geometric-control tools are essential to properly analyze the complex dynamics of these systems as they naturally account for the multi-body dynamics, hence capture the vibrational stabilization mechanisms due to aerodynamic-dynamic interactions. Finally, Fig. 4.15 summarizes the analysis performed in this section.

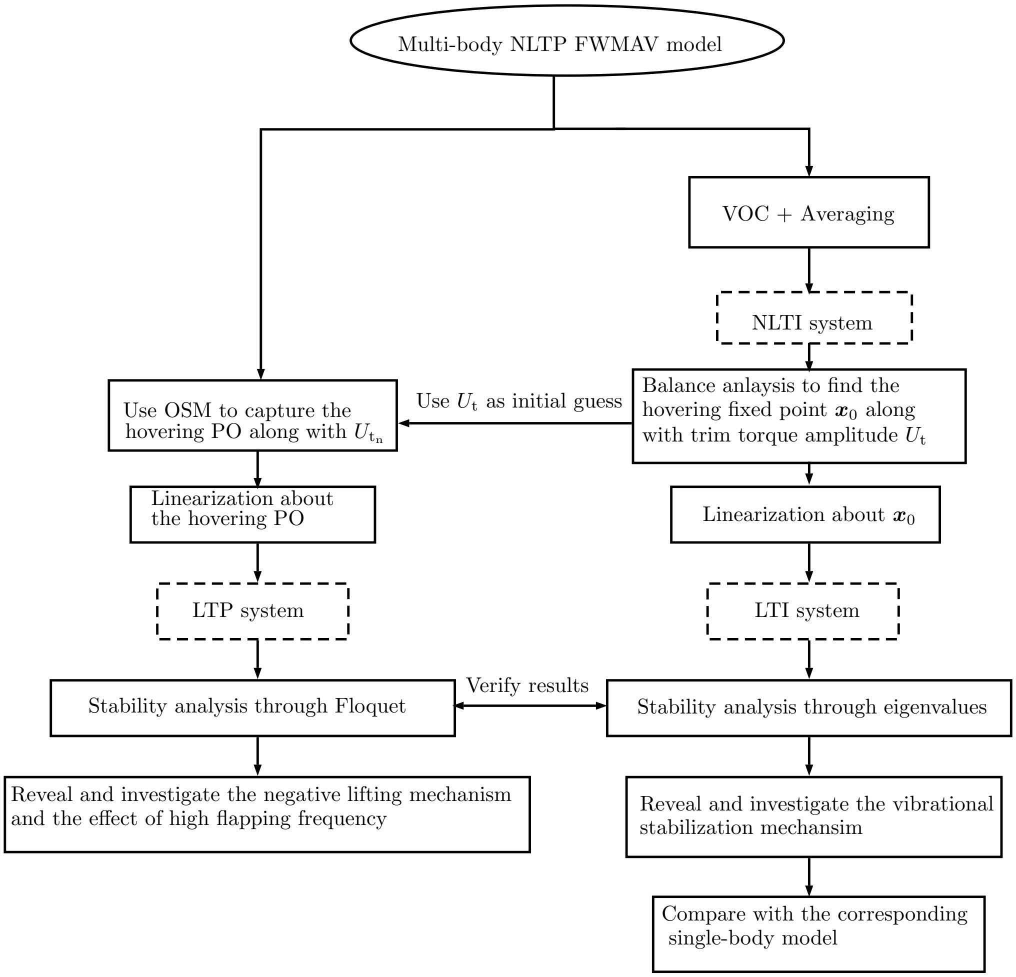

Figure 4.15: Summary of the analysis steps performed in Sec. 4.4.

Chapter 5

Conclusions and Future Work

5.1 Conclusions

5.1.1 Airplane Nonlinear Controllability and Motion Planning

The fixed-wing airplane flight dynamics has been formulated in a differential-geometric-control framework. A new rolling/yawing mechanism that could be utilized for stall recovery has been discovered. A reduced-order, three DOF flight dynamics model has been developed to perform a comprehensive investigation of the novel roll mechanism. Employing nonlinear motion planning tools, the maximum capability of the novel roll mechanism near stall has been examined and compared to that of the conventional one. The novel roll mechanism has been proved to be superior to the conventional one at near-stall operating points, where aileron sensitivity degrades. In particular, the novel roll mechanism was able to generate more than four times as much roll as the conventional one was capable of at that operating point, abiding by the same control input limits and within the same amount of time. Hence, the novel roll mechanism may provide a more efficient way to recover from stall/spin situations in commercial aircraft. Also, it could be employed by fighter aircraft to perform high angle of attack (low speed) maneuvers.

Moreover, a methodology for analyzing the nonlinear controllability of the airplane utilizing the differential-geometric control tools has been introduced. Employing this methodology, nonlinear controllability analysis in case of complete hydraulic failure, i.e., using thrust controls only, has been performed. The system has shown to be nonlinearly controllable if either I_{XZ} or $M_{\delta_{t_s}}$ is non-zero., despite being linearly uncontrollable.

5.1.2 FWMAVs Differential-Geometric-Control Formulation and Averaging Analysis

The two common assumptions (neglecting wing inertia and performing direct-averaging) usually adopted in balance and stability analysis of FWMAVs and insects have been relaxed. Hence, the full (five DOF) multi-body, nonlinear, longitudinal flight dynamics of FWMAVs have been formulated and cast in a differential-geometric-control framework. A mathematically rigorous analysis for the balance and stability of FWMAVs has been performed by combining tools from chronological calculus, geometric control, averaging, periodic shooting, and Floquet theorem.

In particular, a two DOF model (where balance and stability are decoupled) has been extracted from the full model to rigorously investigate the balance problem at hover. A procedure that combines averaging and periodic shooting techniques has been introduced to accurately capture the balance requirement at hover. It has been found that the a cycle-averaged lift force that is equal to the vehicle's weight is not enough to maintain balance at hover, due to the existence of a negative lifting mechanism. The negative lifting mechanism is induced by the multi-body (wing-body) interactions that are not typically captured by a single-body model or even by applying first-order averaging (after VOC formula) on a multi-body model. That is, this mechanism is only captured when applying higher-order averaging on the multi-body model or if the periodic orbit of the multi-body dynamics is numerically captured.

Moreover, a three DOF (vertical motion, pitching motion, and wing flapping dynamics) model has been extracted from the full model to rigorously investigate both balance and stability at hover. The most important finding of the three DOF model analysis is that the high-frequency periodic forcing on FWMAVs/insects induces vibrational stabilization mechanisms to their relatively slow body dynamics. These stabilizing mechanisms are mainly due to the interaction between the aero-inertial loads on the flapping wings due to the fast flapping motion and those due to the slow body motion: what we call aerodynamic-dynamic interaction. The main conclusion is that this interaction is instrumental for the open-loop stability analysis of such nonlinear time-periodic systems. Moreover, it cannot be captured by direct averaging or without accounting for the wing flapping dynamics. Therefore, the differential-geometric-control tools are proven to be essential to properly analyze the complex dynamics of these systems as they naturally account for the multi-body dynamics and nonlinear phenomena.

5.2 Future Work

5.2.1 Degree of Nonlinear Controllability

The nonlinear controllability concept is a qualitative (binary) one; a given system is either controllable or not. That is, there is no quantitative measure that gives an insight into how easy/hard to steer a system to its equilibrium from a given point in the state space. However, such a quantitative measure has been developed for linear controllability. Eising [150] introduced the concept of *distance from uncontrollable* to characterize how weakly controllable a linear system is. Later, Hamdan and Nayfeh [151] defined the concept of *modal controllability measure* which provides a continuous measure (from zero to one) to characterize the linear controllability of each mode (eigenvector) of the linear system. Extending these quantitative measures to nonlinear systems would allow a rigorous assessment of any discovered unconventional (Lie bracket action) motion generation mechanism, e.g., the novel roll mechanism explained in Sec. 3.5.

5.2.2 Experimental Demonstration of the Novel Roll Mechanism

A wind tunnel experiment is recommended to verify the obtained results for the novel roll mechanism in Sec. 3.5. Figure 5.1 shows a schematic diagram for the experiment apparatus. The experiment constitutes of a sub-scale airplane model of a commercial transport airplane that is placed on a test rig which allows for pitch and roll but not yaw. Heaving motion is also allowed but constrained through a tension spring. The airplane model is trimmed at a near-stall angle of attack and the aileron and elevator are commanded sinusoid control signals to realize the Lie-bracket roll mechanism as explained in Sec. 3.5. The roll response is measured through an inertial measurement unit (IMU) and logged into a computer for further analysis. The same experiment is repeated while commanding a fixed aileron deflection (i.e., the conventional roll mechanism). Responses from both mechanisms are then compared.

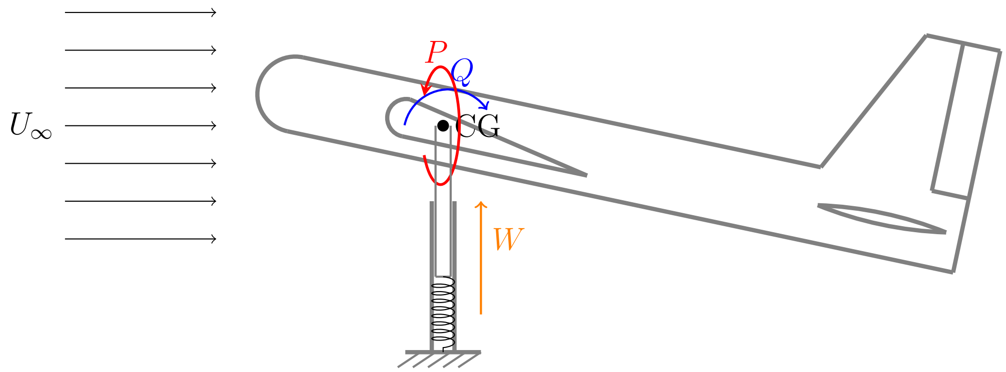

Figure 5.1: A schematic diagram for the wind tunnel experiment.

5.2.3 Nonlinear Controllability Analysis of FWMAVs

The flight dynamics of FWMAVs/insects is heavily under-actuated; only two control inputs are available to the five DOF longitudinal flight dynamics as explained in Sec. 4.2. Hence, a next step in this endeavor should be performing a rigorous nonlinear controllability analysis, similar to that performed for the fixed-wing aircraft in Chapter 3. As such, various unconventional motion generation mechanisms could be revealed. To perform such an analysis, the equations of motion of the lateral DOF have to be derived and augmented with the longitudinal ones. Afterwards, the nonlinear controllability of the full (longitudinal and lateral) nonlinear, multi-body dynamics could be assessed at the hovering equilibrium.

Bibliography

[1] H. E. Taha. Aircraft guidance along a prescribed trajectory using inverse simulation and model reference adaptive control. *Cairo University*, 2008.

[2] Haithem Taha, Mohammadali Kiani, and Joel Navarro. Experimental demonstration of the vibrational stabilization phenomenon in bio-inspired flying robots. *IEEE Robotics and Automation Letters*, 3(2):643–647, 2018.

[3] Rudolf Kalman. On the general theory of control systems. *IRE Transactions on Automatic Control*, 4(3):110–110, 1959.

[4] Rudolf Emil Kalman. Mathematical description of linear dynamical systems. *Journal of the Society for Industrial and Applied Mathematics, Series A: Control*, 1(2):152–192, 1963.

[5] Rudolph Emil Kalman. A new approach to linear filtering and prediction problems. *Journal of basic Engineering*, 82(1):35–45, 1960.

[6] Rudolph E Kalman and Richard S Bucy. New results in linear filtering and prediction theory. *Journal of basic engineering*, 83(1):95–108, 1961.

[7] Solomon Lefschetz. Stability of nonlinear control systems. Technical report, MARTIN MARIETTA CORP BALTIMORE MD RESEARCH INST FOR ADVANCED STUDIES, 1965.

[8] Joseph P La Salle. An invariance principle in the theory of stability. 1966.

[9] George Zames. On the input-output stability of time-varying nonlinear feedback systems part one: Conditions derived using concepts of loop gain, conicity, and positivity. *IEEE transactions on automatic control*, 11(2):228–238, 1966.

[10] Haithem E Taha. UCI MAE 276: Lecture Notes on Geometric Nonlinear Control. `http://taha.eng.uci.edu/Geometric_Control_Course.html`, Spring 2017.

[11] John M Lee. Smooth manifolds. In *Introduction to Smooth Manifolds*, pages 1–29. Springer, 2003.

[12] Sanjay P Bhat and Dennis S Bernstein. A topological obstruction to continuous global stabilization of rotational motion and the unwinding phenomenon. *Systems & Control Letters*, 39(1):63–70, 2000.

[13] K.S. Narendra R.E. Kalman, Y.C. Ho. Controllability of linear dynamical systems. *Contrib. Differential Equations*, 1:189–213, 1963.

[14] Peter E Crouch. Spacecraft attitude control and stabilization: Applications of geometric control theory to rigid body models. *Automatic Control, IEEE Transactions on*, 29(4):321–331, 1984.

[15] Roger W Brockett. *Finite dimensional linear systems*. Wiley New York, 1970.

[16] Gerardo Lafferriere and H Sussmann. Motion planning for controllable systems without drift. In *Robotics and Automation, 1991. Proceedings., 1991 IEEE International Conference on*, pages 1148–1153. IEEE, 1991.

[17] Héctor J Sussmann and Wensheng Liu. Limits of highly oscillatory controls and the approximation of general paths by admissible trajectories. In *Decision and Control, 1991., Proceedings of the 30th IEEE Conference on*, pages 437–442. IEEE, 1991.

[18] Richard M Murray and Sosale Shankara Sastry. Nonholonomic motion planning: Steering using sinusoids. *IEEE Transactions on Automatic Control*, 38(5):700–716, 1993.

[19] Jérôme Barraquand and Jean-Claude Latombe. Nonholonomic multibody mobile robots: Controllability and motion planning in the presence of obstacles. *Algorithmica*, 10(2-4):121, 1993.

[20] J-P Laumond, Paul E Jacobs, Michel Taix, and Richard M Murray. A motion planner for nonholonomic mobile robots. *IEEE Transactions on Robotics and Automation*, 10(5):577–593, 1994.

[21] Wensheng Liu. An approximation algorithm for nonholonomic systems. *SIAM Journal on Control and Optimization*, 35(4):1328–1365, 1997.

[22] Sepanta Sekhavat and J-P Laumond. Topological property for collision-free nonholonomic motion planning: The case of sinusoidal inputs for chained form systems. *IEEE Transactions on Robotics and Automation*, 14(5):671–680, 1998.

[23] A. A. Agrachev and R. V. Gamkrelidze. The exponential representation of flows and the chronological calculus. *Matematicheskii Sbornik*, 149(4):467–532, 1978.

[24] S. M. Meerkov. Principle of vibrational control: theory and applications. *Automatic Control, IEEE Transactions on*, 25(4):755–762, 1980.

[25] R. Bellman, J. Bentsman, and S. M. Meerkov. On vibrational stabilizability of nonlinear systems. *Journal of optimization theory and applications*, 46(4):421–430, 1985.

[26] R. E. Bellman, J. Bentsman, and S. M. Meerkov. Vibrational control of nonlinear systems: Vibrational stabilizability. *Automatic Control, IEEE Transactions on*, 31(8):710–716, 1986.

[27] J. Bentsman. Vibrational control of a class of nonlinear systems by nonlinear multiplicative vibrations. *Automatic Control, IEEE Transactions on*, 32(8):711–716, 1987.

[28] A. Stephenson. On induced stability. *The London, Edinburgh, and Dublin Philosophical Magazine and Journal of Science*, 15(86):233–236, 1908.

[29] PL Kapitsa. Pendulum with a vibrating suspension. *Uspekhi Fiz. Nauk*, 44(1):7–20, 1951.

[30] PL Kapitsa. Dynamical stability of a pendulum when its point of suspension vibrates. *Collected Papers by PL Kapitsa*, 2:714–725, 1965.

[31] Henk Nijmeijer and Arjan Van der Schaft. *Nonlinear dynamical control systems.* Springer Science & Business Media, 1990.

[32] PAVOL Brunovsky. Local controllability of odd systems. *Banach Center Publ., Warsaw*, 1:39–45, 1974.

[33] Henry Hermes. On local controllability. *SIAM Journal on Control and Optimization*, 20(2):211–220, 1982.

[34] V. Jurdjevic. Polynomial control systems. In *Proc. 22nd IEEE CDC*, volume 2, pages 904–906, 1983.

[35] Peter E Crouch and Christopher I. Byrnes. Local accessibility, local reachability, and representations of compact groups. *Mathematical systems theory*, 19(1):43–65, 1986.

[36] Hector J Sussmann. A general theorem on local controllability. *SIAM Journal on Control and Optimization*, 25(1):158–194, 1987.

[37] Rosa Maria Bianchini and Gianna Stefani. Graded approximations and controllability along a trajectory. *SIAM Journal on Control and Optimization*, 28(4):903–924, 1990.

[38] Wensheng Liu. Averaging theorems for highly oscillatory differential equations and iterated lie brackets. *SIAM journal on control and optimization*, 35(6):1989–2020, 1997.

[39] GW Haynes and H Hermes. Nonlinear controllability via lie theory. *SIAM Journal on Control*, 8(4):450–460, 1970.

[40] J. M. Dietl and E. Garcia. Stability in ornithopter longitudinal flight dynamics. *Journal of Guidance, Control and Dynamics*, 31(4):1157–1162, 2008.

[41] Jiang Hao Wu and Mao Sun. Floquet stability analysis of the longitudinal dynamics of two hovering model insects. *Journal of The Royal Society Interface*, 9(74):2033–2046, 2012.

[42] Bret Stanford, Philip Beran, and Mayuresh Patil. Optimal flapping-wing vehicle dynamics via floquet multiplier sensitivities. *Journal of Guidance, Control, and Dynamics*, 36(2):454–466, 2013.

[43] J. Guckenheimer and P. Holmes. *Nonlinear oscillations, dynamical systems, and bifurcations of vector fields*, volume 42. Springer Science & Business Media, 2013.

[44] J. A. Sanders, F. Verhulst, and J. A Murdock. *Averaging methods in nonlinear dynamical systems*, volume 59. Springer, 2007.

[45] H. K. Khalil. *Nonlinear Systems.* Prentice Hall, 3 edition, 2002.

[46] F. Bullo and A. D Lewis. *Geometric control of mechanical systems: modeling, analysis, and design for simple mechanical control systems*, volume 49. Springer Science & Business Media, 2004.

[47] F. Bullo. Averaging and vibrational control of mechanical systems. *SIAM Journal on Control and Optimization*, 41(2):542–562, 2002.

[48] A. Sarychev. Stability criteria for time-periodic systems via high-order averaging techniques. In *Nonlinear control in the year 2000 volume 2*, pages 365–377. Springer, 2001.

[49] P. A. Vela. *Averaging and control of nonlinear systems.* PhD thesis, California Institute of Technology, 2003.

[50] Haithem E Taha, Sevak Tahmasian, Craig A Woolsey, Ali H Nayfeh, and Muhammad R Hajj. The need for higher-order averaging in the stability analysis of hovering, flapping-wing flight. *Bioinspiration & biomimetics*, 10(1):016002, 2015.

[51] A. H. Nayfeh. *Perturbation Methods.* John Wiley and Sons, Inc., 1973.

[52] Ahmed M Hassan and Haithem E Taha. Airplane loss of control problem: Linear controllability analysis. *Aerospace Science and Technology*, 55:264–271, 2016.

[53] James Wilborn and John Foster. Defining commercial transport loss-of-control: A quantitative approach. In *AIAA atmospheric flight mechanics conference and exhibit*, page 4811, 2004.

[54] Eduardo D Sontag and Hector J Sussmann. Nonlinear output feedback design for linear systems with saturating controls. In *Decision and Control, 1990., Proceedings of the 29th IEEE Conference on*, pages 3414–3416. IEEE, 1990.

[55] Wojciech Blajer and Krzysztof Kołodziejczyk. A geometric approach to solving problems of control constraints: theory and a dae framework. *Multibody System Dynamics*, 11(4):343–364, 2004.

[56] Wojciech Blajer, Robert Seifried, and Krzysztof Kołodziejczyk. Servo-constraint realization for underactuated mechanical systems. *Archive of Applied Mechanics*, 85(9-10):1191–1207, 2015.

[57] Alessandro Fumagalli, Pierangelo Masarati, Marco Morandini, and Paolo Mantegazza. Control constraint realization for multibody systems. *Journal of Computational and Nonlinear Dynamics*, 6(1):011002, 2011.

[58] Pierangelo Masarati, Marco Morandini, and Alessandro Fumagalli. Control constraint of underactuated aerospace systems. *Journal of Computational and Nonlinear Dynamics*, 9(2):021014, 2014.

[59] B. L. Stevens and F. L. Lewis. *Aircraft Control and Simulation.* Wiley-Interscience, 2003.

[60] D. McLean. *Automatic flight control systems.* Prentice Hall, 1990.

[61] Robert C Nelson and Alain Pelletier. The unsteady aerodynamics of slender wings and aircraft undergoing large amplitude maneuvers. *Progress in Aerospace Sciences*, 39(2):185–248, 2003.

[62] Koichi Yamasaki, Yoshimasa Ichihara, Hisako Yasui, and Satoshi Hiranuma. A thrust-only flight-control system as a backup for loss of primary flight controls. *Mitsubishi Heavy Industries Technical Review*, 48(4):1, 2011.

[63] Frank W Burcham, John Burken, and Trindel A Maine. *Flight testing a propulsion-controlled aircraft emergency flight control system on an F-15 airplane.* National Aeronautics and Space Administration, Office of Management, Scientific and Technical Information Program, 1994.

[64] Frank W Burcham, Trindel A Maine, and John J Burken. *Development and flight test of an augmented thrust-only flight control system on an MD-11 transport airplane.* National Aeronautics and Space Administration, Office of Management, Scientific and Technical Information Program, 1996.

[65] Tom Tucker. *Touchdown: The development of propulsion controlled aircraft at NASA Dryden.* NASA History Office, Office of Policy and Plans, NASA Headquarters, 1999.

[66] Ahmed M Hassan and Haithem E Taha. Geometric control formulation and nonlinear controllability of airplane flight dynamics. *Nonlinear Dynamics*, 88(4):2651–2669, 2017.

[67] E. C. Polhamus. A concept of the vortex lift of sharp-edge delta wings based on a leading-edge-suction analogy. Technical Report NASA TN D-3767, Langely Research Center, Langely Station, Hampton, Va, 1966.

[68] Haithem E Taha, Muhammad R Hajj, and Philip S Beran. State-space representation of the unsteady aerodynamics of flapping flight. *Aerospace Science and Technology*, 34:1–11, 2014.

[69] Zhimiao Yan, Haithem E Taha, and Muhammad R Hajj. Geometrically-exact unsteady model for airfoils undergoing large amplitude maneuvers. *Aerospace Science and Technology*, 39:293–306, 2014.

[70] Thomas Jordan, William Langford, Christine Belcastro, John Foster, Gautam Shah, Gregory Howland, and Reggie Kidd. Development of a dynamically scaled generic transport model testbed for flight research experiments. 2004.

[71] Harry G Kwatny, Jean-Etienne T Dongmo, Bor-Chin Chang, Gaurav Bajpai, Murat Yasar, and Christine Belcastro. Nonlinear analysis of aircraft loss of control. *Journal of Guidance, Control, and Dynamics*, 36(1):149–162, 2012.

[72] Alberto Isidori. *Nonlinear control systems*. Springer Science & Business Media, 2013.

[73] Benoit Lemaignan. Flying with no flight controls: Handling qualities analyses of the baghdad event. In *AIAA Atmospheric Flight Mechanics Conference, AIAA-2005-5907*, 2005.

[74] Robert C Nelson. *Flight stability and automatic control*. McGraw-Hill, 2nd edition, 1998.

[75] Hans Munthe-Kaas and Brynjulf Owren. Computations in a free lie algebra. *Philosophical Transactions of the Royal Society of London A: Mathematical, Physical and Engineering Sciences*, 357(1754):957–981, 1999.

[76] Ahmed M Hassan and Haitham E Taha. Geometric nonlinear controllability analysis for airplane flight dynamics. In *AIAA Guidance, Navigation, and Control Conference*, page 0079, 2016.

[77] C. P. Ellington. The aerodynamics of hovering insect flight: Iii. kinematics. *Philosophical Transactions Royal Society London Series B*, 305:41–78, 1984.

[78] X. Deng, L. Schenato, W. C. Wu, and S. S. Sastry. Flapping flight for biomemetic robotic insects: Part ii flight control design. *IEEE Transactions on Robotics*, 22(4):789–803, 2006.

[79] Kirill V Rozhdestvensky and Vladimir A Ryzhov. Aerohydrodynamics of flapping-wing propulsors. *Progress in aerospace sciences*, 39(8):585–633, 2003.

[80] R. J. Wood. The first takeoff of a biologically inspired at-scale robotic insect. *IEEE Transactions on Robotics and Automation*, 24(2):341–347, 2008.

[81] R Åke Norberg. Hovering flight of the dragonfly aeschna juncea l., kinematics and aerodynamics. In *Swimming and flying in nature*, pages 763–781. Springer, 1975.

[82] R. Dudley and C. P. Ellington. Mechanics of forward flight in bumblebees: Ii. quasi-steady lift and power requirements. *Journal of Experimental Biology*, 148:53–88, 1990.

[83] C. P. Ellington. Unsteady aerodynamics of insect flight. volume 49, pages 109–129. Soc. Exp. Biol., 1995.

[84] A. P. Willmott and C. P. Ellington. The mechanisms of flight in the hawkmoth manduca sexta, i: Kinematics of hovering and forward flight. *Journal of Experimental Biology*, 200(21), 1997.

[85] C. P. Ellington, Van den Berg C., A. P. Willmott, and A. L. R. Thomas. Leading-edge vortices in insect flight. *Nature*, 384:626–630, 1996.

[86] Hao Liu, Charles P Ellington, Keiji Kawachi, Coen Van Den Berg, and Alexander P Willmott. A computational fluid dynamic study of hawkmoth hovering. *Journal of experimental biology*, 201(4):461–477, 1998.

[87] Amir S Rezaei and Haitham E Taha. Computational study of lift frequency responses of pitching airfoils at low reynolds numbers. In *55th AIAA Aerospace Sciences Meeting*, page 0716, 2017.

[88] Haitham E Taha and Amir S Rezaei. Unsteady viscous lift frequency response using the triple deck theory. In *2018 AIAA Aerospace Sciences Meeting*, page 0038, 2018.

[89] Mohamed Yehia Zakaria Mohamed. Unsteady nonlinear aerodynamic modeling and applications. *PhD Dissertation, Virginia Tech.*, 2016.

[90] Ahmed A Hussein, Muhammad R Hajj, Samir M Elkholy, and Gamal M ELbayoumi. Dynamic stability of hingeless rotor blade in hover using padé approximations. *AIAA Journal*, pages 1769–1777, 2016.

[91] Ahmed A Hussein and Robert A Canfield. Unsteady aerodynamic stabilization of the dynamics of hingeless rotor blades in hover. *AIAA Journal*, 56(3):1298–1303, 2017.

[92] Ahmed A Hussein, Haithem E Taha, Saad Ragab, and Muhammad R Hajj. A variational approach for the dynamics of unsteady point vortices. *Aerospace Science and Technology*, 78:559–568, 2018.

[93] Ahmed Hussein, Haithem Taha, Saad Ragab, and Muhammad R Hajj. A variational approach for the dynamics of unsteady point vortices with application to impulsively started aerofoil. In *2018 Applied Aerodynamics Conference*, page 3172, 2018.

[94] Ahmed Hussein, Saad A Ragab, Haitham E Taha, and Muhammad R Hajj. Optimal tail kinematics for fish-like locomotion using the unsteady vortex lattice method. In *2018 AIAA Aerospace Sciences Meeting*, page 0311, 2018.

[95] Ahmed A Hussein, Muhammad R Hajj, and Craig Woolsey. Stable, planar self propulsion using a hinged flap. *IFAC-PapersOnLine*, 51(29):395–399, 2018.

[96] Hisham Shehata, Mohamed Zakaria, Ahmed Hussein, and Muhammad R Hajj. Aerodynamic analysis of flapped airfoil at high angles of attack. In *2018 AIAA Aerospace Sciences Meeting*, page 0037, 2018.

[97] Mohamed Y Zakaria, Haithem E Taha, Muhammad R Hajj, and Ahmed A Hussein. Experimental-based unified unsteady nonlinear aerodynamic modeling for two-dimensional airfoils. In *33rd AIAA Applied Aerodynamics Conference*, page 3167, 2015.

[98] M.R. Hajj M.Y. Zakaria, H.E. Taha. Measurement and modeling of lift enhancement on plunging airfoils: A frequency response approach. *Journal of Fluids and Structures*, 69(February 2017):Pages–187, 2017.

[99] Flávio D Marques, Daniel A Pereira, Mohamed Y Zakaria, and Muhammad R Hajj. Power extraction from stall-induced oscillations of an airfoil. *Journal of Intelligent Material Systems and Structures*, page 1045389X17739161, 2017.

[100] AM bayoumy OE Abdelhamid MY Zakaria, AM Elshabka. Aerodynamic characterestics of flapping wings. In *13th Aerospace Sciences and Aviation Technology*, page 18, 2013.

[101] M Y Zakaria, D A Periera, S Ragab, M Hajj, and D Marques. An experimental assessment of unsteady forces on a plunging airfoil oscillating in stationary fluid at high frequencies. *Engineering of Science and Military Technologies Journal*, 1:13, 2017.

[102] MY Zakaria, AM Bayoumy, AM Elshabka, and OE Abd Elhamid. Experimental aerodynamic characteristics of flapping membrane wings. In *13th International Conference on Aerospace Sciences & Aviation Technology, Cairo, Egypt*, 2009.

[103] Mohamed Y Zakaria. Low to medium fidelity models for unsteady pitching maneuvers at low reynolds number. In *2018 AIAA Aerospace Sciences Meeting*, page 0040, 2018.

[104] Mohamed Y Zakaria, David W Allen, Craig A Woolsey, and Muhammad R Hajj. Lift and drag of flapping membrane wings at high angles of attack. In *34th AIAA Applied Aerodynamics Conference*, page 3554, 2016.

[105] Mohamed Y Zakaria, Mostafa M Ibrahim, Saad Ragab, and Muhammad R Hajj. A computational study of vortex shedding from a naca-0012 airfoil at high angles of attack. *International Journal of Aerodynamics*, 6(1):1–17, 2018.

[106] A. L. R. Thomas and G. K. Taylor. Animal flight dynamics i. stability in gliding flight. *Journal of Theoretical Biology*, 212(1):399–424, 2001.

[107] H. E. Taha, M. R. Hajj, and A. H. Nayfeh. Flight dynamics and control of flapping-wing mavs: A review. *Nonlinear Dynamics*, 70(2):907–939, 2012.

[108] J. H. Wu, Y. L. Zhang, and M. Sun. Hovering of model insects: simulation by coupling equations of motion with navier-stokes equations. *The Journal of Experimental Biology*, 212(20):3313–3329, 2009.

[109] G. K. Taylor and A. L. R. Thomas. Animal flight dynamics ii. longitudinal stability in flapping flight. *Journal of Theoretical Biology*, 214, 2002.

[110] G. K. Taylor and A. L. R. Thomas. Dynamic flight stability in the desert locust. *Journal of Theoretical Biology*, 206:2803–2829, 2003.

[111] G. K. Taylor and R. Zbikowski. Nonlinear time periodic models of the longitudinal flight dynamics of desert locusts. *J. Roy. Soc. Interface*, 1, 2005.

[112] Z. A. Khan and S. K. Agrawal. Control of longitudinal flight dynamics of a flapping wing micro air vehicle using time averaged model and differential flatness based controller. pages 5284–5289. IEEE American Control Conference, 2007.

[113] M. Sun and Y. Xiong. Dynamic flight stability of a hovering bumblebee. *Journal of Experimental Biology*, 208(3):447–459, 2005.

[114] Y. Xiong and M. Sun. Dynamic flight stability of a bumble bee in forward flight. *Acta Mechanica Sinica*, 24(3):25–36, 2008.

[115] M. W. Oppenheimer, D. B. Doman, and D. O. Sigthorsson. Dynamics and control of a biomimetic vehicle using biased wingbeat forcing functions. *Journal Guidance, Control and Dynamics*, 34(1):204–217, 2011.

[116] Sevak Tahmasian and Craig A Woolsey. Flight control of biomimetic air vehicles using vibrational control and averaging. *Journal of Nonlinear Science*, 27(4):1193–1214, 2017.

[117] Ahmed Hussein and Haitham E Taha. Minimum-time transition of fwmavs from hovering to forward flight. In *AIAA Atmospheric Flight Mechanics Conference*, page 0017, 2016.

[118] Mohamed Y Zakaria, Haithem E Taha, and Muhammad R Hajj. Design optimization of flapping ornithopters: the pterosaur replica in forward flight. *Journal of Aircraft*, 53(1):48–59, 2015.

[119] Christopher T Orlowski and Anouck R Girard. Dynamics, stability, and control analyses of flapping wing micro-air vehicles. *Progress in Aerospace Sciences*, 51:18–30, 2012.

[120] Haithem E Taha, Ali H Nayfeh, and Muhammad R Hajj. Effect of the aerodynamic-induced parametric excitation on the longitudinal stability of hovering mavs/insects. *Nonlinear Dynamics*, 78(4):2399–2408, 2014.

[121] John M Dietl and Ephrahim Garcia. Stability in ornithopter longitudinal flight dynamics. *Journal of Guidance, Control, and Dynamics*, 31(4):1157–1163, 2008.

[122] Andrey V Sarychev. Lie-and chronologico-algebraic tools for studying stability of time-varying systems. *Systems & Control Letters*, 43(1):59–76, 2001.

[123] D. T. Greenwood. *Advanced Dynamics*. Cambridge University Press, The Edinburgh Building, Cambridge CB2 2RU, UK, 2003.

[124] T. Weis-Fogh. Quick estimates of flight fitness in hovering animals, including novel mechanisms for lift production. *Journal of Experimental Biology*, 59(1):169–230, 1973.

[125] Haithem E Taha, Muhammad R Hajj, and Ali H Nayfeh. Longitudinal flight dynamics of hovering mavs/insects. *Journal of Guidance, Control, and Dynamics*, 37(3):970–979, 2014.

[126] H. E. Taha, A. H. Nayfeh, and M. R. Hajj. Aerodynamic-dynamic interaction and longitudinal stability of hovering mavs/insects. Number AIAA 2013-1707, Boston, Apr 2013. 54th Structural Dynamics and Materials Conference.

[127] H. E. Taha, M. R. Hajj, and P. S. Beran. Unsteady nonlinear aerodynamics of hovering mavs/insects. AIAA-Paper 2013-0504, Jan 2013.

[128] Haithem E Taha, Muhammad R Hajj, and Philip S Beran. State-space representation of the unsteady aerodynamics of flapping flight. *Aerospace Science and Technology*, 34:1–11, 2014.

[129] G. J. Berman and Z. J. Wang. Energy-minimizing kinematics in hovering insect flight. *Journal of Fluid Mechanics*, 582(1):153,168, 2007.

[130] M. H. Dickinson, F.-O. Lehmann, and S. P. Sane. Wing rotation and the aerodynamic basis of insect flight. *Science*, 284(5422):1954–1960, 1999.

[131] H. Schlichting and E. Truckenbrodt. *Aerodynamics of the Airplane*. McGraw-Hill, 1979.

[132] Z Jane Wang. Vortex shedding and frequency selection in flapping flight. *Journal of Fluid Mechanics*, 410:323–341, 2000.

[133] Ravi Ramamurti and William C Sandberg. A three-dimensional computational study of the aerodynamic mechanisms of insect flight. *Journal of experimental biology*, 205(10):1507–1518, 2002.

[134] Bernard Etkin. *Dynamics of Flight - Stabililty and Control*. JOHN WILEY and SONS, 1996.

[135] L. Schenato, D. Campolo, and S. S. Sastry. Controllability issues in flapping flight for biomemetic mavs. volume 6, pages 6441–6447. 42nd IEEE conference on Decision and Control, 2003.

[136] D. B. Doman, M. W. Oppenheimer, and D. O. Sigthorsson. Wingbeat shape modulation for flapping-wing micro-air-vehicle control during hover. *Journal of Guidance, Control and Dynamics*, 33(3):724–739, 2010.

[137] H. E. Taha, M. R. Hajj, and A. H. Nayfeh. Wing kinematics optimization for hovering micro air vehicles using calculus of variation. *Journal of Aircraft*, 50(2):610–614, 2013.

[138] H. E. Taha, A. H. Nayfeh, and M. R. Hajj. Saturation-based actuation for flapping mavs in hovering and forward flight. *Nonlinear Dynamics*, 73(1):1125–1138, 2013.

[139] H. E. Taha, C. A. Woolsey, and M. R Hajj. Geometric control approach to longitudinal stability of flapping flight. *Journal of Guidance, Control, and Dynamics*, 39(2):214–226, 2016.

[140] Robert Dudley. *The biomechanics of insect flight: form, function, evolution*. Princeton University Press, 2002.

[141] Stephen M Nogar, Abhijit Gogulapati, Jack J McNamara, Andrea Serrani, Michael W Oppenheimer, and David B Doman. Control-oriented modeling of coupled electromechanical-aeroelastic dynamics for flapping-wing vehicles. *Journal of Guidance, Control, and Dynamics*, 2017.

[142] Ahmed M Hassan and Haithem E Taha. Higher-order averaging analysis of the nonlinear time-periodic dynamics of hovering insects/flapping-wing micro-air-vehicles. In *Decision and Control (CDC), 2016 IEEE 55th Conference on*, pages 7477–7482. IEEE, 2016.

[143] Ahmed M Hassan and Haithem E Taha. Combined averaging–shooting approach for the analysis of flapping flight dynamics. *Journal of Guidance, Control, and Dynamics*, 41(2):542–549, 2017.

[144] Ahmed M Hassan and Haitham E Taha. A combined averaging-shooting approach for the trim analysis of hovering insects/flapping-wing micro-air-vehicles. In *AIAA Guidance, Navigation, and Control Conference*, page 1734, 2017.

[145] M. Sun, J. Wang, and Y. Xiong. Dynamic flight stability of hovering insects. *Acta Mechanica Sinica*, 23(3):231–246, 2007.

[146] B. Cheng and X. Deng. Translational and rotational damping of flapping flight and its dynamics and stability at hovering. *IEEE Transactions On Robotics*, 27(5):849–864, 2011.

[147] Ahmed M. Hassan and Haithem E. Taha. Differential-geometric-control formulation of flapping flight multi-body dynamics. *Journal of Nonlinear Science*, Dec 2018.

[148] W Dednam and Andre E Botha. Optimized shooting method for finding periodic orbits of nonlinear dynamical systems. *Engineering with Computers*, 31(4):749–762, 2015.

[149] A. H. Nayfeh and B. Balachandran. *Applied Nonlinear Dynamics.* John Wiley and Sons, Inc., 1995.

[150] Rikus Eising. Between controllable and uncontrollable. *Systems & control letters*, 4(5):263–264, 1984.

[151] AMA Hamdan and AH Nayfeh. Measures of modal controllability and observability for first-and second-order linear systems. *Journal of guidance, control, and dynamics*, 12(3):421–428, 1989.

[152] Ahmed M Hassan and Haitham E Taha. Aerodynamic-dynamic interactions and multibody formulation of flapping wing dynamics: Part i modeling. In *AIAA Guidance, Navigation, and Control Conference*, page 1274, 2017.

[153] Ahmed M Hassan and Haitham E Taha. Aerodynamic-dynamic interactions and multibody formulation of flapping wing dynamics: Part ii trim and stability analysis. In *AIAA Guidance, Navigation, and Control Conference*, page 1275, 2017.

[154] Henri Gavin. The levenberg-marquardt method for nonlinear least squares curve-fitting problems. *Department of Civil and Environmental Engineering, Duke University*, pages 1–15, 2011.

[155] C. P. Ellington. The aerodynamics of hovering insect flight: Ii. morphological parameters. *Philosophical Transactions Royal Society London Series B*, 305:17–40, 1984.

Appendix A

First order Lie brackets of Airplane Nonlinear Dynamics Vector Fields

In this Appendix, we show the ten first-order Lie brackets between the vector fields $\boldsymbol{f}$ and $\boldsymbol{g}_i$'s, Eqs. (3.6–3.10) at the cruise flight condition.

$$\left[\boldsymbol{f}, \boldsymbol{g}_{\delta_e}\right] = \begin{bmatrix} \begin{array}{c} \frac{q^2 S^2 W_0 C_{X_{\delta_e}}(\alpha) C_X{}'(\alpha)}{m^2 U_0^2 \left(\frac{W_0^2}{U_0^2}+1\right)} - \frac{q^2 S^2 C_{Z_{\delta_e}}(\alpha) C_X{}'(\alpha)}{m^2 U_0 \left(\frac{W_0^2}{U_0^2}+1\right)} + \\ -C_7 q S \bar{c} C_{M_{\delta_e}}(\alpha) \left(\frac{q S \bar{c} C_{X_Q}(\alpha)}{2m\sqrt{U_0^2+W_0^2}} - W_0\right) \end{array} \\ \\ 0 \\ \\ \begin{array}{c} \frac{q^2 S^2 W_0 C_{X_{\delta_e}}(\alpha) C_Z{}'(\alpha)}{m^2 U_0^2 \left(\frac{W_0^2}{U_0^2}+1\right)} - \frac{q^2 S^2 C_{Z_{\delta_e}}(\alpha) C_Z{}'(\alpha)}{m^2 U_0 \left(\frac{W_0^2}{U_0^2}+1\right)} + \\ -C_7 \bar{c} q S C_{M_{\delta_e}}(\alpha) \left(U_0 + \frac{q S \bar{c} C_{Z_Q}(\alpha)}{2m\sqrt{U_0^2+W_0^2}}\right) \end{array} \\ \\ \begin{array}{c} -\frac{q S C_{Z_{\delta_e}}(\alpha)}{m} \left(\frac{C_3 q S b \frac{\partial C_{\mathcal{L}}(\alpha,\beta)}{\partial \alpha}}{U_0\left(\frac{W_0^2}{U_0^2}+1\right)} + \frac{C_4 q S b \frac{\partial C_N(\alpha,\beta)}{\partial \alpha}}{U_0\left(\frac{W_0^2}{U_0^2}+1\right)}\right) + \\ -\frac{q S C_{X_{\delta_e}}(\alpha)}{m} \left(-\frac{C_3 q S b W_0 \frac{\partial C_{\mathcal{L}}(\alpha,\beta)}{\partial \alpha}}{U_0^2\left(\frac{W_0^2}{U_0^2}+1\right)} - \frac{C_4 q S b W_0 \frac{\partial C_N(\alpha,\beta)}{\partial \alpha}}{U_0^2\left(\frac{W_0^2}{U_0^2}+1\right)}\right) \end{array} \\ \\ \begin{array}{c} \frac{C_7 q^2 S^2 \bar{c} W_0 C_{X_{\delta_e}}(\alpha) C_M'(\alpha)}{m U_0^2 \left(\frac{W_0^2}{U_0^2}+1\right)} - \frac{C_7^2 q^2 S^2 \bar{c}^2 C_{M_{\delta_e}}(\alpha) C_{M_Q}(\alpha)}{2\sqrt{U_0^2+W_0^2}} + \\ -\frac{C_7 q^2 S^2 \bar{c} C_{Z_{\delta_e}}(\alpha) C_M'(\alpha)}{m U_0 \left(\frac{W_0^2}{U_0^2}+1\right)} \end{array} \\ \\ \begin{array}{c} -\frac{q S C_{Z_{\delta_e}}(\alpha)}{m} \left(\frac{C_4 q S b \frac{\partial C_{\mathcal{L}}(\alpha,\beta)}{\partial \alpha}}{U_0\left(\frac{W_0^2}{U_0^2}+1\right)} + \frac{C_9 q S b \frac{\partial C_N(\alpha,\beta)}{\partial \alpha}}{U_0\left(\frac{W_0^2}{U_0^2}+1\right)}\right) + \\ -\frac{q S C_{X_{\delta_e}}(\alpha)}{m} \left(-\frac{C_4 q S b W_0 \frac{\partial C_{\mathcal{L}}(\alpha,\beta)}{\partial \alpha}}{U_0^2\left(\frac{W_0^2}{U_0^2}+1\right)} - \frac{C_9 q S b W_0 \frac{\partial C_N(\alpha,\beta)}{\partial \alpha}}{U_0^2\left(\frac{W_0^2}{U_0^2}+1\right)}\right) \end{array} \\ 0 \\ \\ -C_7 q S \bar{c} C_{M_{\delta_e}}(\alpha) \\ \\ 0 \end{bmatrix} \tag{A.1}$$

$$\left[\boldsymbol{f},\boldsymbol{g}_{\delta_a}\right]=\begin{bmatrix} 0 \\[2ex] \begin{array}{c} -\frac{q^2S^2C_{Y_{\delta_a}}(\beta)C'_Y(\beta)}{m^2\sqrt{U_0^2+W_0^2}}+\frac{q^2S^2C_Y(\beta)C'_{Y_{\delta_a}}(\beta)}{m^2\sqrt{U_0^2+W_0^2}}+ \\ -qSb\left(C_3C_{\mathcal{L}_{\delta_a}}(\alpha,\beta)+C_4C_{N_{\delta_a}}(\alpha,\beta)\right)\left(W_0+\frac{qSbC_{Y_p}(\alpha)}{2m\sqrt{U_0^2+W_0^2}}\right)+ \\ -qSb\left(C_4C_{\mathcal{L}_{\delta_a}}(\alpha,\beta)+C_9C_{N_{\delta_a}}(\alpha,\beta)\right)\left(\frac{qSbC_{Y_r}(\alpha)}{2m\sqrt{U_0^2+W_0^2}}-U_0\right) \end{array} \\[2ex] 0 \\[2ex] \begin{array}{c} \frac{q^2S^2bC_Y(\beta)}{m}\left(\frac{C_3\frac{\partial C_{\mathcal{L}_{\delta_a}}(\alpha,\beta)}{\partial\beta}}{\sqrt{U_0^2+W_0^2}}+\frac{C_4\frac{\partial C_{N_{\delta_a}}(\alpha,\beta)}{\partial\beta}}{\sqrt{U_0^2+W_0^2}}\right)+ \\ -\frac{qSC_{Y_{\delta_a}}(\beta)}{m}\left(\frac{C_3qSb\frac{\partial C_{\mathcal{L}}(\alpha,\beta)}{\partial\beta}}{\sqrt{U_0^2+W_0^2}}+\frac{C_4qSb\frac{\partial C_N(\alpha,\beta)}{\partial\beta}}{\sqrt{U_0^2+W_0^2}}\right)+ \\ -qSb\left(C_3C_{\mathcal{L}_{\delta_a}}(\alpha,\beta)+C_4C_{N_{\delta_a}}(\alpha,\beta)\right)\left(\frac{C_3qSbC_{\mathcal{L}_P}(\alpha)}{2\sqrt{U_0^2+W_0^2}}+\frac{C_4qSbC_{N_P}(\alpha)}{2\sqrt{U_0^2+W_0^2}}\right)+ \\ -qSb\left(C_4C_{\mathcal{L}_{\delta_a}}(\alpha,\beta)+C_9C_{N_{\delta_a}}(\alpha,\beta)\right)\left(\frac{C_3qSbC_{\mathcal{L}_R}(\alpha)}{2\sqrt{U_0^2+W_0^2}}+\frac{C_4qSbC_{N_R}(\alpha)}{2\sqrt{U_0^2+W_0^2}}\right) \end{array} \\[2ex] 0 \\[2ex] \begin{array}{c} \frac{q^2S^2bC_Y(\beta)}{m}\left(\frac{C_4\frac{\partial C_{\mathcal{L}_{\delta_a}}(\alpha,\beta)}{\partial\beta}}{\sqrt{U_0^2+W_0^2}}+\frac{C_9\frac{\partial C_{N_{\delta_a}}(\alpha,\beta)}{\partial\beta}}{\sqrt{U_0^2+W_0^2}}\right)+ \\ -\frac{qSC_{Y_{\delta_a}}(\beta)}{m}\left(\frac{C_4qSb\frac{\partial C_{\mathcal{L}}(\alpha,\beta)}{\partial\beta}}{\sqrt{U_0^2+W_0^2}}+\frac{C_9qSb\frac{\partial C_N(\alpha,\beta)}{\partial\beta}}{\sqrt{U_0^2+W_0^2}}\right) \\ -qSb\left(C_3C_{\mathcal{L}_{\delta_a}}(\alpha,\beta)+C_4C_{N_{\delta_a}}(\alpha,\beta)\right)\left(\frac{C_4qSbC_{\mathcal{L}_P}(\alpha)}{2\sqrt{U_0^2+W_0^2}}+\frac{C_9qSbC_{N_P}(\alpha)}{2\sqrt{U_0^2+W_0^2}}\right) \\ -qSb\left(C_4C_{\mathcal{L}_{\delta_a}}(\alpha,\beta)+C_9C_{N_{\delta_a}}(\alpha,\beta)\right)\left(\frac{C_4qSbC_{\mathcal{L}_R}(\alpha)}{2\sqrt{U_0^2+W_0^2}}+\frac{C_9qSbC_{N_R}(\alpha)}{2\sqrt{U_0^2+W_0^2}}\right) \end{array} \\[2ex] \begin{array}{c} -qSb\left(C_3C_{\mathcal{L}_{\delta_a}}(\alpha,\beta)+C_4C_{N_{\delta_a}}(\alpha,\beta)\right)+ \\[1ex] -\frac{qSbW_0}{U_0}\left(C_4C_{\mathcal{L}_{\delta_a}}(\alpha,\beta)+C_9C_{N_{\delta_a}}(\alpha,\beta)\right) \end{array} \\[2ex] 0 \\[2ex] -qSb\sqrt{\frac{W_0^2}{U_0^2}+1}\left(C_4C_{\mathcal{L}_{\delta_a}}(\alpha,\beta)+C_9C_{N_{\delta_a}}(\alpha,\beta)\right) \end{bmatrix} \tag{A.2}$$

$$
\left[\boldsymbol{f},\boldsymbol{g}_{\delta_r}\right]=\begin{bmatrix}
0\\
\begin{gathered}
-\frac{q^2S^2C_{Y_{\delta_r}}(\beta)C'_Y(\beta)}{m^2\sqrt{U_0^2+W_0^2}}+\frac{q^2S^2C_Y(\beta)C'_{Y_{\delta_r}}(\beta)}{m^2\sqrt{U_0^2+W_0^2}}+\\
-qSb\left(C_3C_{\mathcal{L}_{\delta_r}}(\alpha,\beta)+C_4C_{N_{\delta_r}}(\alpha,\beta)\right)\left(W_0+\frac{qSbC_{Y_p}(\alpha)}{2m\sqrt{U_0^2+W_0^2}}\right)+\\
-qSb\left(C_4C_{\mathcal{L}_{\delta_r}}(\alpha,\beta)+C_9C_{N_{\delta_r}}(\alpha,\beta)\right)\left(\frac{qSbC_{Y_r}(\alpha)}{2m\sqrt{U_0^2+W_0^2}}-U_0\right)
\end{gathered}\\
0\\
\begin{gathered}
\frac{q^2S^2bC_Y(\beta)}{m}\left(\frac{C_3\frac{\partial C_{\mathcal{L}_{\delta_r}}(\alpha,\beta)}{\partial\beta}}{\sqrt{U_0^2+W_0^2}}+\frac{C_4\frac{\partial C_{N_{\delta_r}}(\alpha,\beta)}{\partial\beta}}{\sqrt{U_0^2+W_0^2}}\right)+\\
-\frac{qSC_{Y_{\delta_r}}(\beta)}{m}\left(\frac{C_3qSb\frac{\partial C_{\mathcal{L}}(\alpha,\beta)}{\partial\beta}}{\sqrt{U_0^2+W_0^2}}+\frac{C_4qSb\frac{\partial C_N(\alpha,\beta)}{\partial\beta}}{\sqrt{U_0^2+W_0^2}}\right)+\\
-qSb\left(C_3C_{\mathcal{L}_{\delta_r}}(\alpha,\beta)+C_4C_{N_{\delta_r}}(\alpha,\beta)\right)\left(\frac{C_3qSbC_{\mathcal{L}_P}(\alpha)}{2\sqrt{U_0^2+W_0^2}}+\frac{C_4qSbC_{N_P}(\alpha)}{2\sqrt{U_0^2+W_0^2}}\right)+\\
-qSb\left(C_4C_{\mathcal{L}_{\delta_r}}(\alpha,\beta)+C_9C_{N_{\delta_r}}(\alpha,\beta)\right)\left(\frac{C_3qSbC_{\mathcal{L}_R}(\alpha)}{2\sqrt{U_0^2+W_0^2}}+\frac{C_4qSbC_{N_R}(\alpha)}{2\sqrt{U_0^2+W_0^2}}\right)
\end{gathered}\\
0\\
\begin{gathered}
\frac{q^2S^2bC_Y(\beta)}{m}\left(\frac{C_4\frac{\partial C_{\mathcal{L}_{\delta_r}}(\alpha,\beta)}{\partial\beta}}{\sqrt{U_0^2+W_0^2}}+\frac{C_9\frac{\partial C_{N_{\delta_r}}(\alpha,\beta)}{\partial\beta}}{\sqrt{U_0^2+W_0^2}}\right)+\\
-\frac{qSC_{Y_{\delta_r}}(\beta)}{m}\left(\frac{C_4qSb\frac{\partial C_{\mathcal{L}}(\alpha,\beta)}{\partial\beta}}{\sqrt{U_0^2+W_0^2}}+\frac{C_9qSb\frac{\partial C_N(\alpha,\beta)}{\partial\beta}}{\sqrt{U_0^2+W_0^2}}\right)+\\
-qSb\left(C_3C_{\mathcal{L}_{\delta_r}}(\alpha,\beta)+C_4C_{N_{\delta_r}}(\alpha,\beta)\right)\left(\frac{C_4qSbC_{\mathcal{L}_P}(\alpha)}{2\sqrt{U_0^2+W_0^2}}+\frac{C_9qSbC_{N_P}(\alpha)}{2\sqrt{U_0^2+W_0^2}}\right)+\\
-qSb\left(C_4C_{\mathcal{L}_{\delta_r}}(\alpha,\beta)+C_9C_{N_{\delta_r}}(\alpha,\beta)\right)\left(\frac{C_4qSbC_{\mathcal{L}_R}(\alpha)}{2\sqrt{U_0^2+W_0^2}}+\frac{C_9qSbC_{N_R}(\alpha)}{2\sqrt{U_0^2+W_0^2}}\right)
\end{gathered}\\
-qSb\left(C_3C_{\mathcal{L}_{\delta_r}}(\alpha,\beta)+C_4C_{N_{\delta_r}}(\alpha,\beta)\right)-\frac{qSbW_0\left(C_4C_{\mathcal{L}_{\delta_r}}(\alpha,\beta)+C_9C_{N_{\delta_r}}(\alpha,\beta)\right)}{U_0}\\
0\\
-qSb\sqrt{\frac{W_0^2}{U_0^2}+1}\left(C_4C_{\mathcal{L}_{\delta_r}}(\alpha,\beta)+C_9C_{N_{\delta_r}}(\alpha,\beta)\right)
\end{bmatrix}\tag{A.3}
$$

$$\left[\boldsymbol{f},\boldsymbol{g}_{\delta_t}\right]=\begin{bmatrix}
\begin{gathered}-C_7M_{\delta_t}\left(\frac{qS\bar{c}C_{X_Q}(\alpha)}{2m\sqrt{U_0^2+W_0^2}}-W_0\right)+\\
+\frac{qSW_0X_{\delta_t}C'_X(\alpha)}{m^2U_0^2\left(\frac{W_0^2}{U_0^2}+1\right)}-\frac{qSZ_{\delta_t}C'_X(\alpha)}{m^2U_0\left(\frac{W_0^2}{U_0^2}+1\right)}\end{gathered}\\
0\\
\begin{gathered}-C_7M_{\delta_t}\left(\frac{qS\bar{c}C_{Z_Q}(\alpha)}{2m\sqrt{U_0^2+W_0^2}}+U_0\right)+\\
+\frac{qSW_0X_{\delta_t}C'_Z(\alpha)}{m^2U_0^2\left(\frac{W_0^2}{U_0^2}+1\right)}-\frac{qSZ_{\delta_t}C'_Z(\alpha)}{m^2U_0\left(\frac{W_0^2}{U_0^2}+1\right)}\end{gathered}\\
\begin{gathered}-\frac{X_{\delta_t}}{m}\left(-\frac{C_3qSbW_0\frac{\partial C_{\mathcal{L}}(\alpha,\beta)}{\partial\alpha}}{U_0^2\left(\frac{W_0^2}{U_0^2}+1\right)}-\frac{C_4qSbW_0\frac{\partial C_N(\alpha,\beta)}{\partial\alpha}}{U_0^2\left(\frac{W_0^2}{U_0^2}+1\right)}\right)+\\
-\frac{Z_{\delta_t}}{m}\left(\frac{C_3qSb\frac{\partial C_{\mathcal{L}}(\alpha,\beta)}{\partial\alpha}}{U_0\left(\frac{W_0^2}{U_0^2}+1\right)}+\frac{C_4qSb\frac{\partial C_N(\alpha,\beta)}{\partial\alpha}}{U_0\left(\frac{W_0^2}{U_0^2}+1\right)}\right)\end{gathered}\\
-\frac{C_7^2qS\bar{c}M_{\delta_t}C_{M_Q}(\alpha)}{2\sqrt{U_0^2+W_0^2}}+\frac{C_7qS\bar{c}W_0X_{\delta_t}C'_M(\alpha)}{mU_0^2\left(\frac{W_0^2}{U_0^2}+1\right)}-\frac{C_7qS\bar{c}Z_{\delta_t}C'_M(\alpha)}{mU_0\left(\frac{W_0^2}{U_0^2}+1\right)}\\
\begin{gathered}-\frac{X_{\delta_t}}{m}\left(-\frac{C_4qSbW_0\frac{\partial C_{\mathcal{L}}(\alpha,\beta)}{\partial\alpha}}{U_0^2\left(\frac{W_0^2}{U_0^2}+1\right)}-\frac{C_9qSbW_0\frac{\partial C_N(\alpha,\beta)}{\partial\alpha}}{U_0^2\left(\frac{W_0^2}{U_0^2}+1\right)}\right)+\\
-\frac{Z_{\delta_t}}{m}\left(\frac{C_4qSb\frac{\partial C_{\mathcal{L}}(\alpha,\beta)}{\partial\alpha}}{U_0\left(\frac{W_0^2}{U_0^2}+1\right)}+\frac{C_9qSb\frac{\partial C_N(\alpha,\beta)}{\partial\alpha}}{U_0\left(\frac{W_0^2}{U_0^2}+1\right)}\right)\end{gathered}\\
0\\
-C_7M_{\delta_t}\\
0
\end{bmatrix}\tag{A.4}$$

$$\left[\boldsymbol{g}_{\delta_e}, \boldsymbol{g}_{\delta_a}\right] = \begin{bmatrix} 0 \\ 0 \\ 0 \\ \begin{gathered} \frac{q^2 S^2 b\ C_{X_{\delta_e}}(\alpha)}{m}\left(-\frac{C_3 W_0 \frac{\partial C_{\mathcal{L}_{\delta_a}}(\alpha,\beta)}{\partial \alpha}}{U_0^2\left(\frac{W_0^2}{U_0^2}+1\right)} - \frac{C_4 W_0 \frac{\partial C_{N_{\delta_a}}(\alpha,\beta)}{\partial \alpha}}{U_0^2\left(\frac{W_0^2}{U_0^2}+1\right)}\right)+ \\ +\frac{q^2 S^2 b\ C_{Z_{\delta_e}}(\alpha)}{m}\left(\frac{C_3 \frac{\partial C_{\mathcal{L}_{\delta_a}}(\alpha,\beta)}{\partial \alpha}}{U_0\left(\frac{W_0^2}{U_0^2}+1\right)} + \frac{C_4 \frac{\partial C_{N_{\delta_a}}(\alpha,\beta)}{\partial \alpha}}{U_0\left(\frac{W_0^2}{U_0^2}+1\right)}\right) \end{gathered} \\ 0 \\ \begin{gathered} \frac{q^2 S^2 b\ C_{X_{\delta_e}}(\alpha)}{m}\left(-\frac{C_4 W_0 \frac{\partial C_{\mathcal{L}_{\delta_a}}(\alpha,\beta)}{\partial \alpha}}{U_0^2\left(\frac{W_0^2}{U_0^2}+1\right)} - \frac{C_9 W_0 \frac{\partial C_{N_{\delta_a}}(\alpha,\beta)}{\partial \alpha}}{U_0^2\left(\frac{W_0^2}{U_0^2}+1\right)}\right)+ \\ +\frac{q^2 S^2 b\ C_{Z_{\delta_e}}(\alpha)}{m}\left(\frac{C_4 \frac{\partial C_{\mathcal{L}_{\delta_a}}(\alpha,\beta)}{\partial \alpha}}{U_0\left(\frac{W_0^2}{U_0^2}+1\right)} + \frac{C_9 \frac{\partial C_{N_{\delta_a}}(\alpha,\beta)}{\partial \alpha}}{U_0\left(\frac{W_0^2}{U_0^2}+1\right)}\right) \end{gathered} \\ 0 \\ 0 \\ 0 \end{bmatrix} \tag{A.5}$$

$$\left[\boldsymbol{g}_{\delta_e},\boldsymbol{g}_{\delta_r}\right]=\begin{bmatrix} 0 \\ 0 \\ 0 \\ \begin{gathered}\frac{q^2S^2b\ C_{X_{\delta_e}}(\alpha)}{m}\left(-\frac{C_3W_0\frac{\partial C_{\mathcal{L}_{\delta_r}}(\alpha,\beta)}{\partial\alpha}}{U_0^2\left(\frac{W_0^2}{U_0^2}+1\right)}-\frac{C_4W_0\frac{\partial C_{N_{\delta_r}}(\alpha,\beta)}{\partial\alpha}}{U_0^2\left(\frac{W_0^2}{U_0^2}+1\right)}\right)+\\ +\frac{q^2S^2b\ C_{Z_{\delta_e}}(\alpha)}{m}\left(\frac{C_3\frac{\partial C_{\mathcal{L}_{\delta_r}}(\alpha,\beta)}{\partial\alpha}}{U_0\left(\frac{W_0^2}{U_0^2}+1\right)}+\frac{C_4\frac{\partial C_{N_{\delta_r}}(\alpha,\beta)}{\partial\alpha}}{U_0\left(\frac{W_0^2}{U_0^2}+1\right)}\right)\end{gathered} \\ 0 \\ \begin{gathered}\frac{q^2S^2b\ C_{X_{\delta_e}}(\alpha)}{m}\left(-\frac{C_4W_0\frac{\partial C_{\mathcal{L}_{\delta_r}}(\alpha,\beta)}{\partial\alpha}}{U_0^2\left(\frac{W_0^2}{U_0^2}+1\right)}-\frac{C_9W_0\frac{\partial C_{N_{\delta_r}}(\alpha,\beta)}{\partial\alpha}}{U_0^2\left(\frac{W_0^2}{U_0^2}+1\right)}\right)+\\ +\frac{q^2S^2b\ C_{Z_{\delta_e}}(\alpha)}{m}\left(\frac{C_4\frac{\partial C_{\mathcal{L}_{\delta_r}}(\alpha,\beta)}{\partial\alpha}}{U_0\left(\frac{W_0^2}{U_0^2}+1\right)}+\frac{C_9\frac{\partial C_{N_{\delta_r}}(\alpha,\beta)}{\partial\alpha}}{U_0\left(\frac{W_0^2}{U_0^2}+1\right)}\right)\end{gathered} \\ 0 \\ 0 \\ 0 \end{bmatrix} \tag{A.6}$$

$$\left[\boldsymbol{g}_{\delta_e}, \boldsymbol{g}_{\delta_t}\right] = \begin{bmatrix} \frac{qSW_0X_{\delta_t}C'_{X_{\delta_e}}(\alpha)}{m^2U_0^2\left(\frac{W_0^2}{U_0^2}+1\right)} - \frac{qSZ_{\delta_t}C'_{X_{\delta_e}}(\alpha)}{m^2U_0\left(\frac{W_0^2}{U_0^2}+1\right)} \\ 0 \\ \frac{qSW_0X_{\delta_t}C'_{Z_{\delta_e}}(\alpha)}{m^2U_0^2\left(\frac{W_0^2}{U_0^2}+1\right)} - \frac{qSZ_{\delta_t}C'_{Z_{\delta_e}}(\alpha)}{m^2U_0\left(\frac{W_0^2}{U_0^2}+1\right)} \\ 0 \\ \frac{C_7qS\bar{c}W_0X_{\delta_t}C'_{M_{\delta_e}}(\alpha)}{mU_0^2\left(\frac{W_0^2}{U_0^2}+1\right)} - \frac{C_7qS\bar{c}Z_{\delta_t}C'_{M_{\delta_e}}(\alpha)}{mU_0\left(\frac{W_0^2}{U_0^2}+1\right)} \\ 0 \\ 0 \\ 0 \\ 0 \end{bmatrix} \tag{A.7}$$

$$
\left[\boldsymbol{g}_{\delta_a}, \boldsymbol{g}_{\delta_r}\right] = \begin{bmatrix}
0 \\
\frac{q^2 S^2 C_{Y_{\delta_a}}(\beta) C'_{Y_{\delta_r}}(\beta)}{m^2 \sqrt{U_0^2+W_0^2}} - \frac{q^2 S^2 C_{Y_{\delta_r}}(\beta) C'_{Y_{\delta_a}}(\beta)}{m^2 \sqrt{U_0^2+W_0^2}} \\
0 \\
\begin{gathered}
\frac{q^2 S^2 b \;\, C_{Y_{\delta_a}}(\beta)}{m} \left(\frac{C_3 \frac{\partial C_{\mathcal{L}_{\delta_r}}(\alpha,\beta)}{\partial \beta}}{\sqrt{U_0^2+W_0^2}} + \frac{C_4 \frac{\partial C_{N_{\delta_r}}(\alpha,\beta)}{\partial \beta}}{\sqrt{U_0^2+W_0^2}} \right) + \\
- \frac{q^2 S^2 b \;\, C_{Y_{\delta_r}}(\beta)}{m} \left(\frac{C_3 \frac{\partial C_{\mathcal{L}_{\delta_a}}(\alpha,\beta)}{\partial \beta}}{\sqrt{U_0^2+W_0^2}} + \frac{C_4 \frac{\partial C_{N_{\delta_a}}(\alpha,\beta)}{\partial \beta}}{\sqrt{U_0^2+W_0^2}} \right)
\end{gathered} \\
0 \\
\begin{gathered}
\frac{q^2 S^2 b \;\, C_{Y_{\delta_a}}(\beta)}{m} \left(\frac{C_4 \frac{\partial C_{\mathcal{L}_{\delta_r}}(\alpha,\beta)}{\partial \beta}}{\sqrt{U_0^2+W_0^2}} + \frac{C_9 \frac{\partial C_{N_{\delta_r}}(\alpha,\beta)}{\partial \beta}}{\sqrt{U_0^2+W_0^2}} \right) + \\
- \frac{q^2 S^2 b \;\, C_{Y_{\delta_r}}(\beta)}{m} \left(\frac{C_4 \frac{\partial C_{\mathcal{L}_{\delta_a}}(\alpha,\beta)}{\partial \beta}}{\sqrt{U_0^2+W_0^2}} + \frac{C_9 \frac{\partial C_{N_{\delta_a}}(\alpha,\beta)}{\partial \beta}}{\sqrt{U_0^2+W_0^2}} \right)
\end{gathered} \\
0 \\
0 \\
0
\end{bmatrix} \tag{A.8}
$$

$$\left[\boldsymbol{g}_{\delta_r}, \boldsymbol{g}_{\delta_t}\right] = \begin{bmatrix} 0 \\ 0 \\ 0 \\ -\frac{qSbX_{\delta_t}}{m}\left(-\frac{C_3 W_0 \frac{\partial C_{\mathcal{L}_{\delta_r}}(\alpha,\beta)}{\partial\alpha}}{U_0^2\left(\frac{W_0^2}{U_0^2}+1\right)} - \frac{C_4 W_0 \frac{\partial C_{N_{\delta_r}}(\alpha,\beta)}{\partial\alpha}}{U_0^2\left(\frac{W_0^2}{U_0^2}+1\right)}\right) + \\ -\frac{qSbZ_{\delta_t}}{m}\left(\frac{C_3 \frac{\partial C_{\mathcal{L}_{\delta_r}}(\alpha,\beta)}{\partial\alpha}}{U_0\left(\frac{W_0^2}{U_0^2}+1\right)} + \frac{C_4 \frac{\partial C_{N_{\delta_r}}(\alpha,\beta)}{\partial\alpha}}{U_0\left(\frac{W_0^2}{U_0^2}+1\right)}\right) \\ 0 \\ -\frac{qSbX_{\delta_t}}{m}\left(-\frac{C_4 W_0 \frac{\partial C_{\mathcal{L}_{\delta_r}}(\alpha,\beta)}{\partial\alpha}}{U_0^2\left(\frac{W_0^2}{U_0^2}+1\right)} - \frac{C_9 W_0 \frac{\partial C_{N_{\delta_r}}(\alpha,\beta)}{\partial\alpha}}{U_0^2\left(\frac{W_0^2}{U_0^2}+1\right)}\right) + \\ -\frac{qSbZ_{\delta_t}}{m}\left(\frac{C_4 \frac{\partial C_{\mathcal{L}_{\delta_r}}(\alpha,\beta)}{\partial\alpha}}{U_0\left(\frac{W_0^2}{U_0^2}+1\right)} + \frac{C_9 \frac{\partial C_{N_{\delta_r}}(\alpha,\beta)}{\partial\alpha}}{U_0\left(\frac{W_0^2}{U_0^2}+1\right)}\right) \\ 0 \\ 0 \\ 0 \end{bmatrix} \tag{A.9}$$

$$\left[\boldsymbol{g}_{\delta_a},\boldsymbol{g}_{\delta_t}\right]=\begin{bmatrix}0\\0\\0\\-\frac{qSbX_{\delta_t}}{m}\left(-\frac{C_3W_0\frac{\partial C_{\mathcal{L}_{\delta_a}}(\alpha,\beta)}{\partial\alpha}}{U_0^2\left(\frac{W_0^2}{U_0^2}+1\right)}-\frac{C_4W_0\frac{\partial C_{N_{\delta_a}}(\alpha,\beta)}{\partial\alpha}}{U_0^2\left(\frac{W_0^2}{U_0^2}+1\right)}\right)+\\-\frac{qSbZ_{\delta_t}}{m}\left(\frac{C_3\frac{\partial C_{\mathcal{L}_{\delta_a}}(\alpha,\beta)}{\partial\alpha}}{U_0\left(\frac{W_0^2}{U_0^2}+1\right)}+\frac{C_4\frac{\partial C_{N_{\delta_a}}(\alpha,\beta)}{\partial\alpha}}{U_0\left(\frac{W_0^2}{U_0^2}+1\right)}\right)\\0\\-\frac{qSbX_{\delta_t}}{m}\left(-\frac{C_4W_0\frac{\partial C_{\mathcal{L}_{\delta_a}}(\alpha,\beta)}{\partial\alpha}}{U_0^2\left(\frac{W_0^2}{U_0^2}+1\right)}-\frac{C_9W_0\frac{\partial C_{N_{\delta_a}}(\alpha,\beta)}{\partial\alpha}}{U_0^2\left(\frac{W_0^2}{U_0^2}+1\right)}\right)+\\-\frac{qSbZ_{\delta_t}}{m}\left(\frac{C_4\frac{\partial C_{\mathcal{L}_{\delta_a}}(\alpha,\beta)}{\partial\alpha}}{U_0\left(\frac{W_0^2}{U_0^2}+1\right)}+\frac{C_9\frac{\partial C_{N_{\delta_a}}(\alpha,\beta)}{\partial\alpha}}{U_0\left(\frac{W_0^2}{U_0^2}+1\right)}\right)\\0\\0\\0\end{bmatrix}\tag{A.10}$$

Appendix B

Derivation of the FWMAV's Five DOF Equations of Motion

We use the principle of virtual power [123], as explained in Sec. 4.2, to derive the five-DOF equations of motion (4.2) in detail. The various terms in Eq. (4.1) for the body and wing are given below.

B.1 Body

The linear velocity of the reference point of the body axis system (the body's center of gravity) and the corresponding angular velocity are written as

$$\boldsymbol{v}_{\mathrm{b}} = \dot{x}\boldsymbol{i}_{\mathrm{I}} + \dot{z}\boldsymbol{k}_{\mathrm{I}} \quad \text{and} \quad \boldsymbol{\omega}_{\mathrm{b}} = \dot{\theta}\boldsymbol{j}_{\mathrm{b}} = \dot{\theta}\boldsymbol{j}_{\mathrm{I}},$$

where $\boldsymbol{i}$, $\boldsymbol{j}$, and $\boldsymbol{k}$ are unit vectors along the x, y, and z directions in the axis-system indicated by the subscript. Thus, one obtains

$$\begin{array}{lllll} \dfrac{\partial \boldsymbol{v}_{\mathrm{b}}}{\partial \dot{x}} = \boldsymbol{i}_{\mathrm{I}} & \dfrac{\partial \boldsymbol{v}_{\mathrm{b}}}{\partial \dot{z}} = \boldsymbol{k}_{\mathrm{I}} & \dfrac{\partial \boldsymbol{v}_{\mathrm{b}}}{\partial \dot{\theta}} = \mathbf{0} & \dfrac{\partial \boldsymbol{v}_{\mathrm{b}}}{\partial \dot{\varphi}} = \mathbf{0} & \dfrac{\partial \boldsymbol{v}_{\mathrm{b}}}{\partial \dot{\eta}} = \mathbf{0} \\ \dfrac{\partial \boldsymbol{\omega}_{\mathrm{b}}}{\partial \dot{x}} = \mathbf{0} & \dfrac{\partial \boldsymbol{\omega}_{\mathrm{b}}}{\partial \dot{z}} = \mathbf{0} & \dfrac{\partial \boldsymbol{\omega}_{\mathrm{b}}}{\partial \dot{\theta}} = \boldsymbol{j}_{\mathrm{I}} & \dfrac{\partial \boldsymbol{\omega}_{\mathrm{b}}}{\partial \dot{\varphi}} = \mathbf{0} & \dfrac{\partial \boldsymbol{\omega}_{\mathrm{b}}}{\partial \dot{\eta}} = \mathbf{0} \end{array} ,$$

and

$$\dot{\boldsymbol{v}}_{\mathrm{b}} = \ddot{x}\boldsymbol{i}_{\mathrm{I}} + \ddot{z}\boldsymbol{k}_{\mathrm{I}}.$$

The angular momentum vector of the body about its center of gravity and its inertial derivative are given by

$$\boldsymbol{h}_{\mathrm{b}} = I_{yb}\dot{\theta}\boldsymbol{j}_{\mathrm{I}}, \qquad \dot{\boldsymbol{h}}_{\mathrm{b}} = I_{yb}\ddot{\theta}\boldsymbol{j}_{\mathrm{I}}.$$

The aerodynamic contribution of the body is neglected and, hence, the body exhibits gravitational forces only with no moments. Thus, the body force in the inertial frame is written as

$$\boldsymbol{f}_{\mathrm{b}}^{(\mathrm{I})} = [0, \;\; 0, \;\; m_{\mathrm{b}}g]^{*}.$$

B.2 Wing

The linear velocity of the reference point of the wing frame (the hinge root) and its angular velocity are written as

$$\boldsymbol{v}_{\mathrm{w}} = (\dot{x} - x_{\mathrm{h}}\dot{\theta}\sin\theta)\boldsymbol{i}_{\mathrm{I}} + (\dot{z} - x_{\mathrm{h}}\dot{\theta}\cos\theta)\boldsymbol{k}_{\mathrm{I}}, \qquad \boldsymbol{\omega}_{\mathrm{w}} = \dot{\theta}\boldsymbol{j}_{\mathrm{b}} - \dot{\varphi}\boldsymbol{k}_{\mathrm{s}} + \dot{\eta}\boldsymbol{j}_{\mathrm{w}}.$$

Thus, one obtains

$$\begin{array}{lllll}\dfrac{\partial \boldsymbol{v}_{\mathrm{w}}}{\partial \dot{x}} = \boldsymbol{i}_{\mathrm{I}} & \dfrac{\partial \boldsymbol{v}_{\mathrm{w}}}{\partial \dot{z}} = \boldsymbol{k}_{\mathrm{I}} & \dfrac{\partial \boldsymbol{v}_{\mathrm{w}}}{\partial \dot{\theta}} = -x_{\mathrm{h}}(\sin\theta \boldsymbol{i}_{\mathrm{I}} + \cos\theta \boldsymbol{k}_{\mathrm{I}}) & \dfrac{\partial \boldsymbol{v}_{\mathrm{w}}}{\partial \dot{\varphi}} = \mathbf{0} & \dfrac{\partial \boldsymbol{v}_{\mathrm{w}}}{\partial \dot{\eta}} = \mathbf{0} \\ \dfrac{\partial \boldsymbol{\omega}_{\mathrm{w}}}{\partial \dot{x}} = \mathbf{0} & \dfrac{\partial \boldsymbol{\omega}_{\mathrm{w}}}{\partial \dot{z}} = \mathbf{0} & \dfrac{\partial \boldsymbol{\omega}_{\mathrm{w}}}{\partial \dot{\theta}} = \boldsymbol{j}_{\mathrm{I}} & \dfrac{\partial \boldsymbol{\omega}_{\mathrm{w}}}{\partial \dot{\varphi}} = -\boldsymbol{k}_{\mathrm{b}} & \dfrac{\partial \boldsymbol{\omega}_{\mathrm{w}}}{\partial \dot{\eta}} = -\boldsymbol{j}_{\mathrm{w}} \end{array} ,$$

and

$$\dot{\boldsymbol{v}}_{\mathrm{w}} = [\ddot{x} - x_{\mathrm{h}}\ddot{\theta}\sin\theta - x_{\mathrm{h}}\dot{\theta}^2\cos\theta]\boldsymbol{i}_{\mathrm{I}} + [\ddot{z} - x_{\mathrm{h}}\ddot{\theta}\cos\theta + x_{\mathrm{h}}\dot{\theta}^2\sin\theta]\boldsymbol{k}_{\mathrm{I}}.$$

The rotation matrix from the inertial frame to the stroke plane frame is given by

$$\boldsymbol{R}_{\beta} = \begin{bmatrix} \cos\beta & 0 & -\sin\beta \\ 0 & 1 & 0 \\ \sin\beta & 0 & \cos\beta \end{bmatrix},$$

and rotation matrices from the stroke plane frame to the wing frame are

$$\boldsymbol{R}_{\varphi} = \begin{bmatrix} \cos\varphi & -\sin\varphi & 0 \\ \sin\varphi & \cos\varphi & 0 \\ 0 & 0 & 1 \end{bmatrix}, \quad \boldsymbol{R}_{\eta} = \begin{bmatrix} \cos\eta & 0 & -\sin\eta \\ 0 & 1 & 0 \\ \sin\eta & 0 & \cos\eta \end{bmatrix},$$

and

$$\boldsymbol{R}_{\mathrm{ws}} = \boldsymbol{R}_{\eta}\boldsymbol{R}_{\varphi}.$$

The wing angular velocity vector in the wing frame is

$$\boldsymbol{\omega}_{\mathrm{w}}^{(\mathrm{w})} = \begin{pmatrix} \omega_1 \\ \omega_2 \\ \omega_3 \end{pmatrix} = \boldsymbol{R}_{\mathrm{ws}} \begin{pmatrix} 0 \\ \dot{\theta} \\ -\dot{\varphi} \end{pmatrix} + \begin{pmatrix} 0 \\ \dot{\eta} \\ 0 \end{pmatrix} = \begin{pmatrix} \dot{\varphi}\sin\eta - \dot{\theta}\cos\eta\sin\varphi \\ \dot{\theta}\cos\varphi + \dot{\eta} \\ -\dot{\varphi}\cos\eta - \dot{\theta}\sin\eta\sin\varphi \end{pmatrix}.$$

The position vector pointing from the hinge root to the wing center of gravity is $\boldsymbol{\rho}_{\boldsymbol{c}_{\mathrm{w}}} = -\hat{d}\boldsymbol{i}_{\mathrm{w}} + r_{\mathrm{cg}}\boldsymbol{j}_{\mathrm{w}}$ where $\hat{d}$ and r_{cg} are the distances between the wing root hinge point and the wing center of gravity along the negative x_{w}-axis and the y_{w}-axis, respectively. Thus, the inertial acceleration is obtained as

$$\ddot{\boldsymbol{\rho}}_{\boldsymbol{c}_{\mathrm{w}}}^{(\mathrm{w})} = \begin{pmatrix} \ddot{\rho}_1 \\ \ddot{\rho}_2 \\ \ddot{\rho}_3 \end{pmatrix} = \begin{pmatrix} \hat{d}(\omega_2^2 + \omega_3^2) - r_{\mathrm{cg}}(\dot{\omega}_3 - \omega_1\omega_2) \\ -\hat{d}(\dot{\omega}_3 + \omega_1\omega_2) - r_{\mathrm{cg}}(\omega_1^2 + \omega_3^2) \\ \hat{d}(\dot{\omega}_2 - \omega_1\omega_3) + r_{\mathrm{cg}}(\dot{\omega}_1 + \omega_2\omega_3) \end{pmatrix}.$$

Assuming the wing reference frame is fixed in the wing principal axes, the inertial time derivative of the angular momentum vector represented in the wing frame is written as

$$\dot{\boldsymbol{h}}_{\mathrm{w}}^{(\mathrm{w})} = \begin{pmatrix} \dot{h}_1 \\ \dot{h}_2 \\ \dot{h}_3 \end{pmatrix} = \begin{pmatrix} I_x\dot{\omega}_1 + (I_z - I_y)\omega_2\omega_3 \\ I_y\dot{\omega}_y + (I_x - I_z)\omega_1\omega_3 \\ I_z\dot{\omega}_3 + (I_y - I_x)\omega_1\omega_2 \end{pmatrix}.$$

The wing is subject to aerodynamic and gravitational forces. Noting that the y_b-components of the aerodynamic force on each wing are equal and opposite, the force vector applied on the wing is written as

$$\boldsymbol{f}_{\mathrm{w}} = \begin{pmatrix} F_x \\ 0 \\ F_z \end{pmatrix}^{(\mathrm{w})} + \begin{pmatrix} 0 \\ 0 \\ m_{\mathrm{w}}g \end{pmatrix}^{(\mathrm{I})},$$

where F_x and F_z are the aerodynamic loads along the x_{w} and z_{w} directions, respectively. The moment vector comprises three contributions: aerodynamic, gravitational, and the control torque. The aerodynamic contribution $\boldsymbol{M}_{\mathrm{a_w}}$ is determined by integrating the radial distributions of the forces F_x and F_z over the wing. That is, $\boldsymbol{M}_{\mathrm{a_w}} = M_x \boldsymbol{i}_{\mathrm{w}} + M_y \boldsymbol{j}_{\mathrm{w}} + M_z \boldsymbol{k}_{\mathrm{w}}$, where

$$M_x = 2\int_0^R F_z'(r) r dr, \quad M_y = 2\int_0^R F_z'(r) d_{\mathrm{ac}}(r) dr, \quad \text{and} \quad M_z = -2\int_0^R F_x'(r) r dr,$$

where $F_x'(r)$ and $F_z'(r)$ are the two-dimensional aerodynamic loads on an airfoil that is at distance r from the wing root and $d_{\mathrm{ac}}(r)$ is the distance between the hinge line and the quarter-chord line (aerodynamic center) at each airfoil section along x_{w} direction. The gravitational contribution is written as $\boldsymbol{M}_{\mathrm{g_w}} = (-\hat{d}\boldsymbol{i}_{\mathrm{w}} + r_{\mathrm{cg}}\boldsymbol{j}_{\mathrm{w}}) \times m_{\mathrm{w}} g \boldsymbol{k}_{\mathbf{I}}$. The last contribution (the control torque) is written as $\boldsymbol{M}_{\mathrm{c_w}} = -\tau_\varphi \boldsymbol{k}_{\mathrm{s}} + \tau_\eta \boldsymbol{j}_{\mathrm{w}}$, where τ_φ and τ_η are the actuating torque along the flapping and pitching directions, respectively.

Constructing all the required terms to apply the principle of virtual power (4.1), the five-DOF equations of motion are obtained as [152] (with obvious correspondence to the abstract form (4.2))

$$\begin{aligned} & m_{\mathrm{w}}\Big(\ddot{\rho}_1(\cos\beta\cos\eta\cos\varphi - \sin\beta\sin\eta) + \ddot{\rho}_3(\cos\beta\sin\eta\cos\varphi + \sin\beta\cos\eta) + \\ + \quad & \ddot{\rho}_2\cos\beta\sin\varphi - x_{\mathrm{h}}\ddot{\theta}\sin\theta - x_{\mathrm{h}}\dot{\theta}^2\cos\theta\Big) + m_{\mathrm{v}}\dot{u} = \\ = \quad & F_x(\cos\beta\cos\eta\cos\varphi - \sin\beta\sin\eta) + F_z(\cos\beta\sin\eta\cos\varphi + \sin\beta\cos\eta) \end{aligned} \tag{B.1}$$

$$\begin{aligned} - \quad & m_{\mathrm{w}}\Big(\ddot{\rho}_1(\sin\beta\cos\eta\cos\varphi + \cos\beta\sin\eta) + \ddot{\rho}_3(\sin\beta\sin\eta\cos\varphi - \cos\beta\cos\eta) + \\ + \quad & \ddot{\rho}_2\sin\beta\sin\varphi + x_{\mathrm{h}}\ddot{\theta}\cos\theta - x_{\mathrm{h}}\dot{\theta}^2\sin\theta\Big) + m_{\mathrm{v}}(\dot{w} - g) = \\ = \quad & -F_x(\sin\beta\cos\eta\cos\varphi + \cos\beta\sin\eta) - F_z(\sin\beta\sin\eta\cos\varphi - \cos\beta\cos\eta) \end{aligned} \tag{B.2}$$

$$
\begin{aligned}
& m_{\mathrm{w}}\biggl[-x_{\mathrm{h}}\biggl(\ddot{\theta}\ \hat{d}(\cos\beta\cos\eta\cos\theta\cos\varphi+\sin\beta\cos\eta\sin\theta\cos\varphi-\sin\beta\sin\eta\cos\theta+ \\
+ \quad & \cos\beta\sin\eta\sin\theta)-\ddot{\theta}\ r_{\mathrm{cg}}\sin\varphi\cos(\beta-\theta)+ \\
+ \quad & \dot{\theta}^{2}\left(-r_{\mathrm{cg}}\sin\varphi\sin(\beta-\theta)+\hat{d}\cos\eta\cos\varphi\sin(\beta-\theta)+\hat{d}\sin\eta\cos(\beta-\theta)\right)\biggr)+ \\
+ \quad & \dot{u}\left(-\sin\beta\ r_{\mathrm{cg}}\sin\varphi+\hat{d}\sin\beta\cos\eta\cos\varphi+\hat{d}\cos\beta\sin\eta\right)+ \\
+ \quad & \dot{w}\left(-\cos\beta\ r_{\mathrm{cg}}\sin\varphi+\hat{d}\cos\beta\cos\eta\cos\varphi-\hat{d}\sin\beta\sin\eta\right)\biggr]+ \\
+ \quad & I_{y_b}\ddot{\theta}+x_{\mathrm{h}}m_{\mathrm{w}}\biggl[\ddot{\rho}_3\sin\beta\sin\eta\cos\theta\cos\varphi+\ddot{\rho}_1\left(\cos\eta\cos\varphi\sin(\beta-\theta)+\sin\eta\cos(\beta-\theta)\right) \\
- \quad & \ddot{\rho}_3\left(\cos\beta\sin\eta\sin\theta\cos\varphi-\cos\beta\cos\eta\cos\theta-\sin\beta\cos\eta\sin\theta\right)+\ddot{\rho}_2\sin\varphi\sin(\beta-\theta)+ \\
+ \quad & g\cos\theta+x_{\mathrm{h}}\ddot{\theta}-\dot{u}\sin\theta-\dot{w}\cos\theta\biggr]-\dot{h}_3\sin\eta\sin\varphi-\dot{h}_1\cos\eta\sin\varphi+\dot{h}_2\cos\varphi= \\
= \quad & \tau_\eta\cos\varphi-F_z\ x_{\mathrm{h}}\biggl(\sin\beta(\cos\eta\sin\theta-\sin\eta\cos\theta\cos\varphi)+ \\
+ \quad & \cos\beta(\sin\eta\sin\theta\cos\varphi+\cos\eta\cos\theta)\biggr)+F_x x_{\mathrm{h}}(\cos\eta\cos\varphi\sin(\beta-\theta)+\sin\eta\cos(\beta-\theta))+ \\
- \quad & M_x\cos\eta\sin\varphi+M_y\cos\varphi-M_z\sin\eta\sin\varphi
\end{aligned}
\tag{B.3}
$$

$$
\begin{aligned}
& r_{\mathrm{cg}}\ x_{\mathrm{h}}\ m_{\mathrm{w}}\cos\varphi\biggl(\ddot{\theta}\cos\theta\sin\beta-\ddot{\theta}\sin\theta\cos\beta-2\dot{\theta}^{2}\cos\theta\cos\beta-2\ \dot{\theta}^{2}\sin\theta\sin\beta\biggr)+ \\
+ \quad & r_{\mathrm{cg}}\ m_{\mathrm{w}}\cos\varphi\biggl(\dot{u}\cos\beta+u\ \dot{\theta}\sin\beta-\dot{w}\ \sin\beta+w\ \dot{\theta}\cos\beta\biggr)+ \\
+ \quad & \hat{d}\ x_{\mathrm{h}}\ m_{\mathrm{w}}\cos\eta\sin\varphi\biggl(\ddot{\theta}\cos\theta\sin\beta-\ddot{\theta}\sin\theta\cos\beta-2\ \dot{\theta}^{2}\cos\theta\cos\beta-2\ \dot{\theta}^{2}\sin\theta\sin\beta\biggr)+ \\
+ \quad & \hat{d}\ m_{\mathrm{w}}\cos\eta\sin\varphi\biggl(\dot{u}\cos\beta+u\ \dot{\theta}\sin\beta-\dot{w}\ \sin\beta+w\ \dot{\theta}\cos\beta\biggr)+\dot{h}_1\sin\eta-\dot{h}_3\cos\eta= \\
= \quad & \tau_\varphi+M_x\sin\eta-M_z\cos\eta
\end{aligned}
\tag{B.4}
$$

$$\begin{aligned}
& \hat{d}\ x_{\mathrm{h}}\ m_{\mathrm{w}}\Bigg(\ddot{\theta}\sin\eta\cos\theta\cos\varphi\sin\beta - \ddot{\theta}\sin\eta\sin\theta\cos\varphi\cos\beta - \ddot{\theta}\cos\eta\cos\theta\cos\beta + \\
- \quad & \ddot{\theta}\cos\eta\sin\theta\sin\beta - 2\ \dot{\theta}^2\sin\eta\cos\theta\cos\varphi\cos\beta - 2\ \dot{\theta}^2\sin\eta\sin\theta\cos\varphi\sin\beta + \\
- \quad & 2\ \dot{\theta}^2\cos\eta\cos\theta\sin\beta + 2\ \dot{\theta}^2\cos\eta\sin\theta\cos\beta\Bigg) + \hat{d}\ m_{\mathrm{w}}\Bigg(\dot{u}\ \sin\eta\cos\varphi\cos\beta + \\
+ \quad & \dot{u}\ \cos\eta\sin\beta + u\ \dot{\theta}\sin\eta\cos\varphi\sin\beta - u\ \dot{\theta}\cos\eta\cos\beta - \sin\eta\cos\varphi\sin\beta\ \dot{w} + \\
+ \quad & \dot{w}\cos\eta\cos\beta + w\ \dot{\theta}\sin\eta\cos\varphi\cos\beta + w\ \dot{\theta}\cos\eta\sin\beta\Bigg) + \dot{h}_2 = \tau_\eta + M_y,
\end{aligned} \tag{B.5}$$

where $m_{\mathrm{v}} = m_{\mathrm{b}} + m_{\mathrm{w}}$.

Appendix C

FWMAV's Aerodynamic Model

The aerodynamic derivatives in Eq. (4.7) are defined below

$F_{x_0} = \rho\pi \left(kI_{11} - \frac{1}{4}I_{12}\right) \sin\eta \; \dot{\eta}\dot{\varphi}$

$F_{z_0} = -\frac{1}{2}\rho \; C_{L_\alpha} I_{21} \sin\eta \; \dot{\varphi} \, |\dot{\varphi}| - \rho\pi \left(kI_{11} - \frac{1}{4}I_{12}\right) \cos\eta \; \dot{\eta}\dot{\varphi}$

$M_{x_0} = -\frac{1}{2}\rho \; C_{L_\alpha} I_{31} \sin\eta \; \dot{\varphi} \, |\dot{\varphi}| - \rho\pi \left(kI_{21} - \frac{1}{4}I_{22}\right) \cos\eta \; \dot{\eta}\dot{\varphi}$

$M_{y_0} = \frac{3}{4}\Bigg(-\frac{1}{2}\rho \; C_{L_\alpha} I_{22} \sin\eta \; \dot{\varphi} \, |\dot{\varphi}| - \rho\pi \left(kI_{12} - \frac{1}{4}I_{13}\right) \cos\eta \; \dot{\eta}\dot{\varphi} \Bigg) - k \; F_{z_0}$

$M_{z_0} = -\rho\pi \left(kI_{21} - \frac{1}{4}I_{22}\right) \sin\eta \; \dot{\eta}\dot{\varphi}$

$F_{x_u} = \rho\pi \left(kI_{01} - \frac{1}{4}I_{02}\right) (\cos\beta \sin\eta \cos\varphi + \sin\beta \cos\eta) \, \dot{\eta}$

$F_{x_w} = -\rho\pi \left(kI_{01} - \frac{1}{4}I_{02}\right) (\sin\beta \sin\eta \cos\varphi - \cos\beta \cos\eta) \, \dot{\eta}$

$$F_{x_q} = \rho\pi \left(kI_{11} - \frac{1}{4}I_{12}\right) \sin\eta \cos\varphi \; \dot{\varphi} - \rho\pi \Bigg(x_{\mathrm{h}} \left(kI_{01} - \frac{1}{4}I_{02}\right) \Big(\cos\eta \cos(\beta - \theta) + \\ - \sin\eta \cos\varphi \sin(\beta - \theta) \Big) + \cos\eta \sin\varphi \left(kI_{11} - \frac{1}{4}I_{12}\right) \Bigg) \dot{\eta}$$

$$
\begin{aligned}
F_{x_{nl}} = {} & \rho\pi\cos\varphi\ \dot{\theta}\left(kI_{01}-\frac{1}{4}I_{02}\right)\bigg(u\left(\cos\beta\sin\eta\cos\varphi+\sin\beta\cos\eta\right)+ \\
& + w\left(\cos\beta\cos\eta-\sin\beta\sin\eta\cos\varphi\right)\bigg)-\rho\pi\bigg(x_{\mathrm{h}}\cos\varphi\left(kI_{01}-\frac{1}{4}I_{02}\right)\bigg(\cos\eta\cos\left(\beta-\theta\right)+ \\
& -\sin\eta\cos\varphi\sin\left(\beta-\theta\right)\bigg)+\cos\eta\sin\varphi\left(kI_{11}-\frac{1}{4}I_{12}\right)\bigg)\dot{\theta}^{2}
\end{aligned}
$$

$$
\begin{aligned}
F_{z_u} = {} & -\frac{1}{2}\rho\ C_{L_\alpha}I_{11}(2\cos\beta\sin\eta\cos\varphi+\sin\beta\cos\eta)\left|\dot{\varphi}\right|+ \\
& -\rho\pi\left(kI_{01}-\frac{1}{4}I_{02}\right)\left(\cos\beta\cos\eta\cos\varphi-\sin\beta\sin\eta\right)\ \dot{\eta}
\end{aligned}
$$

$$
\begin{aligned}
F_{z_w} = {} & \rho\pi\left(kI_{01}-\frac{1}{4}I_{02}\right)\left(\sin\beta\cos\eta\cos\varphi+\cos\beta\sin\eta\right)\ \dot{\eta}+ \\
& -\frac{1}{2}\rho\ C_{L_\alpha}I_{11}(\cos\beta\cos\eta-2\sin\beta\sin\eta\cos\varphi)\left|\dot{\varphi}\right|
\end{aligned}
$$

$$
\begin{aligned}
F_{z_q} = {} & \frac{1}{2}\rho\ C_{L_\alpha}I_{21}\cos\eta\sin\varphi\ \ \left|\dot{\varphi}\right|+ \\
& +\rho\ C_{L_\alpha}I_{11}\left|\dot{\varphi}\right|\bigg(x_{\mathrm{h}}\sin\beta\sin\eta\cos\theta\cos\varphi+\frac{1}{2}\cos\beta(2x_{\mathrm{h}}\sin\eta\sin\theta\cos\varphi+x_{\mathrm{h}}\cos\eta\cos\theta)+ \\
& +\frac{1}{2}x_{\mathrm{h}}\sin\beta\cos\eta\sin\theta\bigg)+\rho\pi\ x_{\mathrm{h}}\cos\eta\cos\varphi\sin(\beta-\theta)\left(\frac{1}{4}I_{02}-kI_{01}\right)\dot{\eta}+ \\
& +\rho\pi\ x_{\mathrm{h}}\sin\eta\cos(\beta-\theta)\left(\frac{1}{4}I_{02}-kI_{01}\right)\dot{\eta}-\rho\pi\sin\eta\sin\varphi\left(kI_{11}-\frac{1}{4}I_{12}\right)\dot{\eta}+ \\
& -\rho\pi\cos\eta\cos\varphi\left(kI_{11}-\frac{1}{4}I_{12}\right)\dot{\varphi}
\end{aligned}
$$

$$
\begin{aligned}
F_{z_{nl}} = & -\rho\pi\ \cos\varphi\ \dot{\theta}\left(kI_{01}-\frac{1}{4}I_{02}\right)\biggl(u\ (\cos\beta\cos\eta\cos\varphi-\sin\beta\sin\eta)+\\
& + w\ (\sin\beta\cos\eta\cos\varphi+\cos\beta\sin\eta)\biggr)+\\
& + \dot{\theta}^2\biggl(2\pi\rho x_{\mathrm{h}}\cos\varphi\left(\frac{1}{4}I_{02}-kI_{01}\right)(\cos\eta\cos\varphi\sin(\beta-\theta)+\sin\eta\cos(\beta-\theta))+\\
& - 2\pi\rho\sin\eta\sin\varphi\cos\varphi\left(kI_{11}-\frac{1}{4}I_{12}\right)\biggr)
\end{aligned}
$$

$$
\begin{aligned}
M_{x_u} = & -\frac{1}{2}\rho\ C_{L_\alpha}I_{21}(2\cos\beta\sin\eta\cos\varphi+\sin\beta\cos\eta)\,|\dot{\varphi}|+\\
& - \rho\pi\left(kI_{11}-\frac{1}{4}I_{12}\right)(\cos\beta\cos\eta\cos\varphi-\sin\beta\sin\eta)\ \dot{\eta}
\end{aligned}
$$

$$
\begin{aligned}
M_{x_w} = & \ \rho\pi\left(kI_{11}-\frac{1}{4}I_{12}\right)(\sin\beta\cos\eta\cos\varphi+\cos\beta\sin\eta)\ \dot{\eta}+\\
& - \frac{1}{2}\rho\ C_{L_\alpha}I_{21}(\cos\beta\cos\eta-2\sin\beta\sin\eta\cos\varphi)\,|\dot{\varphi}|
\end{aligned}
$$

$$
\begin{aligned}
M_{x_q} = & \ \frac{1}{2}\rho\ C_{L_\alpha}I_{31}\cos\eta\sin\varphi\ \ |\dot{\varphi}|+\rho\ C_{L_\alpha}I_{21}\,|\dot{\varphi}|\ \biggl(x_{\mathrm{h}}\sin\beta\sin\eta\cos\theta\cos\varphi+\\
& + \frac{1}{2}\cos\beta(2x_{\mathrm{h}}\sin\eta\sin\theta\cos\varphi+x_{\mathrm{h}}\cos\eta\cos\theta)+\frac{1}{2}x_{\mathrm{h}}\sin\beta\cos\eta\sin\theta\biggr)+\\
& + \rho\pi x_{\mathrm{h}}\left(\frac{1}{4}I_{12}-kI_{11}\right)\dot{\eta}\ \biggl(\cos\eta\cos\varphi\sin(\beta-\theta)+\sin\eta\cos(\beta-\theta)\biggr)+\\
& - \rho\pi\ \left(kI_{21}-\frac{1}{4}I_{22}\right)\biggl(\sin\eta\sin\varphi\ \dot{\eta}-\cos\eta\cos\varphi\ \dot{\varphi}\biggr)
\end{aligned}
$$

$$
\begin{aligned}
M_{x_{nl}} = & -\rho\pi\ \cos\varphi\left(kI_{11}-\frac{1}{4}I_{12}\right)(\cos\beta\cos\eta\cos\varphi-\sin\beta\sin\eta)\ \dot{\theta}\ u+\\
& +\rho\pi\ \cos\varphi\left(kI_{11}-\frac{1}{4}I_{12}\right)(\sin\beta\cos\eta\cos\varphi+\cos\beta\sin\eta)\ \dot{\theta}\ w+\\
& +\dot{\theta}^2\Bigg(2\rho\pi x_{\mathrm{h}}\cos\varphi\left(\frac{1}{4}I_{12}-kI_{11}\right)(\cos\eta\cos\varphi\sin(\beta-\theta)+\sin\eta\cos(\beta-\theta))+\\
& -2\rho\pi\sin\eta\sin\varphi\cos\varphi\left(kI_{21}-\frac{1}{4}I_{22}\right)\Bigg)
\end{aligned}
$$

$$
\begin{aligned}
M_{y_u} = & \frac{3}{4}\Bigg(-\frac{1}{2}\rho\ C_{L_\alpha}I_{12}(2\cos\beta\sin\eta\cos\varphi+\sin\beta\cos\eta)\,|\dot{\varphi}|+\\
& -\rho\pi\left(kI_{02}-\frac{1}{4}I_{03}\right)(\cos\beta\cos\eta\cos\varphi-\sin\beta\sin\eta)\ \dot{\eta}\Bigg)-k\ F_{z_u}
\end{aligned}
$$

$$
\begin{aligned}
M_{y_w} = & \frac{3}{4}\Bigg(\rho\pi\left(kI_{02}-\frac{1}{4}I_{03}\right)(\sin\beta\cos\eta\cos\varphi+\cos\beta\sin\eta)\ \dot{\eta}+\\
& -\frac{1}{2}\rho\ C_{L_\alpha}I_{12}(\cos\beta\cos\eta-2\sin\beta\sin\eta\cos\varphi)\,|\dot{\varphi}|\Bigg)-k\ F_{z_w}
\end{aligned}
$$

$$
\begin{aligned}
M_{y_q} = & \frac{3}{4}\Bigg(\frac{1}{2}\rho\ C_{L_\alpha}I_{22}\cos\eta\sin\varphi\,|\dot{\varphi}|+\rho\ C_{L_\alpha}I_{12}\,|\dot{\varphi}|\,\Big[x_{\mathrm{h}}\sin\beta\sin\eta\cos\theta\cos\varphi+\\
& +\frac{1}{2}\cos\beta(2x_{\mathrm{h}}\sin\eta\sin\theta\cos\varphi+x_{\mathrm{h}}\cos\eta\cos\theta)+\frac{1}{2}x_{\mathrm{h}}\sin\beta\cos\eta\sin\theta\Big]+\\
& +\rho\pi x_{\mathrm{h}}\cos\eta\cos\varphi\sin(\beta-\theta)\left(\frac{1}{4}I_{03}-kI_{02}\right)\dot{\eta}+\rho\pi x_{\mathrm{h}}\sin\eta\cos(\beta-\theta)\left(\frac{1}{4}I_{03}-kI_{02}\right)\dot{\eta}+\\
& -\rho\pi\sin\eta\sin\varphi\left(kI_{12}-\frac{1}{4}I_{13}\right)\dot{\eta}-\rho\pi\cos\eta\cos\varphi\left(kI_{12}-\frac{1}{4}I_{13}\right)\dot{\varphi}\Bigg)-k\ F_{z_q}
\end{aligned}
$$

$$\begin{aligned}
M_{y_{nl}} = \frac{3}{4}\Bigg(&-\rho\pi\left(kI_{02}-\frac{1}{4}I_{03}\right)\cos\varphi\;\dot{\theta}\Bigg[u\;(\cos\beta\cos\eta\cos\varphi-\sin\beta\sin\eta)+\\
&-w\;(\sin\beta\cos\eta\cos\varphi+\cos\beta\sin\eta)\Bigg]+\\
&+\dot{\theta}^2\Bigg[2\rho\pi x_{\mathrm{h}}\left(\frac{1}{4}I_{03}-kI_{02}\right)\cos\varphi\;(\cos\eta\cos\varphi\sin(\beta-\theta)+\sin\eta\cos(\beta-\theta))+\\
&-2\rho\pi\left(kI_{12}-\frac{1}{4}I_{13}\right)\sin\eta\sin\varphi\cos\varphi\Bigg]\Bigg)-k\;F_{z_{nl}}
\end{aligned}$$

$$M_{z_u} = -\rho\pi\left(kI_{11}-\frac{1}{4}I_{12}\right)(\cos\beta\sin\eta\cos\varphi+\sin\beta\cos\eta)\,\dot{\eta}$$

$$M_{z_w} = \rho\pi\left(kI_{11}-\frac{1}{4}I_{12}\right)(\sin\beta\sin\eta\cos\varphi-\cos\beta\cos\eta)\,\dot{\eta}$$

$$\begin{aligned}
M_{z_q} = \rho\pi\Bigg(&x_{\mathrm{h}}\left(kI_{11}-\frac{1}{4}I_{12}\right)(\cos\eta\cos(\beta-\theta)-\sin\eta\cos\varphi\sin(\beta-\theta))+\\
&+\cos\eta\sin\varphi\left(kI_{21}-\frac{1}{4}I_{22}\right)\Bigg)\;\dot{\eta}-\rho\pi\left(kI_{21}-\frac{1}{4}I_{22}\right)\sin\eta\cos\varphi\;\dot{\varphi}
\end{aligned}$$

$$\begin{aligned}
M_{z_{nl}} = -\rho\pi&\left(kI_{11}-\frac{1}{4}I_{12}\right)\cos\varphi\;\dot{\theta}\Bigg(u\,(\cos\beta\sin\eta\cos\varphi+\sin\beta\cos\eta)+\\
&+w\,(\cos\beta\cos\eta-\sin\beta\sin\eta\cos\varphi)\Bigg)+\\
&+\rho\pi\;\dot{\theta}^2\Bigg(x_{\mathrm{h}}\cos\varphi\left(kI_{11}-\frac{1}{4}I_{12}\right)(\cos\eta\cos(\beta-\theta)-\sin\eta\cos\varphi\sin(\beta-\theta))+\\
&+\cos\eta\sin\varphi\left(kI_{21}-\frac{1}{4}I_{22}\right)\Bigg),
\end{aligned}$$

where $k = c_r(1-x_{or})$, c_r is the wing root chord, x_{or} is the position of the hinge point along x_w normalized by the root chord, and x_{h} is the distance from the vehicle center of mass to the root of the wing hinge line (i.e., the intersection of the hinge line with the x_b-axis). Also, ρ is the air density, C_{L_α} is the three-dimensional lift curve slope of the wing, $c(r)$ is the spanwise chord distribution, R is the wing radius, and $I_{mn} = 2\int_0^R r^m c^n(r)\,dr$.

Appendix D

The Linearized Dynamics of the Averaged Three DOF System

The linearized averaged version of the three-DOF system (4.10) at the trim condition can be written abstractly as [153]

$$\boldsymbol{A} = \left.\frac{\partial \bar{\boldsymbol{F}}}{\partial \bar{\boldsymbol{x}}}\right|_{\bar{\boldsymbol{x}}_0} = \begin{bmatrix} 0 & 0 & 0 & 1 & 0 & 0 \\ 0 & 0 & 0 & 0 & 1 & 0 \\ 0 & 0 & 0 & 0 & 0 & 1 \\ 0 & A_{42} & A_{43} & A_{44} & A_{45} & A_{46} \\ 0 & A_{52} & A_{53} & A_{54} & A_{55} & A_{56} \\ 0 & A_{62} & A_{63} & A_{64} & A_{65} & A_{66} \end{bmatrix}, \tag{D.1}$$

where the elements of the matrix $\boldsymbol{A}$ can be written as (some elements have quite lengthy expressions, hence, we only write their limits as the wing mass goes to zero)

$$\lim_{m_{\mathrm{w}}\to 0} A_{42} = 0$$

$$\begin{aligned}\lim_{m_{\mathrm{w}}\to 0} A_{43} = {} & \frac{0.25AI_{21}\rho U_1^2\sin^2\alpha_m + 0.74C_{L_\alpha}I_{21}\rho U_2^2\sin^2\alpha_m}{I_F^2 m_{\mathrm{v}}\omega^2} - \frac{98.86C_{L_\alpha}I_{21}\rho U_2\sin^2\alpha_m}{I_F m_{\mathrm{v}}\omega} + \\ & + \frac{3307C_{L_\alpha}I_{21}\rho\sin^2\alpha_m}{m_{\mathrm{v}}}\end{aligned}$$

$$\begin{aligned}A_{44} = {} & \frac{1}{I_F I_{y_b} m_{\mathrm{v}}\omega} C_{L_\alpha}\rho\cos\alpha_m\Bigg(\cos\alpha_m\Bigg(I_{11}\Bigg(\bar{c}\hat{d}km_{\mathrm{w}}(0.98U_2 - 41.88I_F\omega) + \\ & + I_{y_b}(0.5U_2 - 78.37I_F\omega)\Bigg) + \\ & + m_{\mathrm{w}}\left(\bar{c}\hat{d}I_{12}(31.4I_F\omega - 0.74U_2) + I_{21}r_{\mathrm{cg}}(2.4I_F\omega - 0.02U_2)\right) + \\ & + \bar{c}\hat{d}I_{21}m_{\mathrm{w}}\cos\alpha_m(0.12U_2 - 19.27I_F\omega)\Bigg) + \\ & + m_{\mathrm{w}}r_{\mathrm{cg}}\left(5.23I_{11}I_Fk\omega - 0.12I_{11}kU_2 - 3.92I_{12}I_F\omega + 0.09I_{12}U_2\right)\Bigg)\end{aligned}$$

$$\lim_{m_{\mathrm{w}}\to 0} A_{45} = \frac{C_{L_\alpha}I_{21}\rho U_2\sin\alpha_m\cos\alpha_m}{I_F m_{\mathrm{v}}\omega} - \frac{42.5C_{L_\alpha}I_{21}\rho\sin\alpha_m\cos\alpha_m}{m_{\mathrm{v}}}$$

$$\lim_{m_{\mathrm{w}}\to 0} A_{46} = \frac{1}{I_F m_{\mathrm{v}}\omega}\Bigg(I_{11}k\rho(1.56U_2 - 66.29I_F\omega) + I_{12}\rho(16.57I_F\omega - 0.39U_2)\Bigg)$$

$$\begin{aligned}A_{52} = {} & \frac{1}{I_F^3 I_{y_b}\omega^2} C_{L_\alpha}I_{y_{\mathrm{w}}}\rho\sin\alpha_m\sin 2\alpha_m\Bigg(I_{21}k\Bigg(-3230I_F^2\omega^2 + 96.6I_FU_2\omega + \\ & - 0.24U_1^2 - 0.73U_2^2\Bigg) + \\ & + I_{22}\left(2422I_F^2\omega^2 - 72.43I_FU_2\omega + 0.18U_1^2 + 0.55U_2^2\right) + \\ & + I_{31}\cos\alpha_m\left(-222I_F^2\omega^2 + 10.5I_FU_2\omega - 0.06U_1^2 - 0.18U_2^2\right)\Bigg)\end{aligned}$$

$$\lim_{m_{\mathrm{w}}\to 0} A_{53} = 0$$

$$\begin{aligned}
A_{54} = {} & \frac{1}{I_F^2 I_{y_b}\omega} C_{L_\alpha}\rho\cos\alpha_m \Bigg(I_{y_\mathrm{w}}\sin 2\alpha_m \Bigg(-2.6 I_{11} I_F k\omega + 0.06 I_{11} k U_2 + \\
& + 1.96 I_{12} I_F \omega - 0.05 I_{12} U_2 + I_{21}\cos\alpha_m (0.01 U_2 - 1.2 I_F \omega) \Bigg) + \\
& + I_{21} I_{y_b} \sin\alpha_m (U_2 - 42.5 I_F \omega) \Bigg)
\end{aligned}$$

$$\begin{aligned}
A_{55} = {} & \frac{1}{I_F^2 I_{y_b}\omega} C_{L_\alpha}\rho\sin\alpha_m \Bigg(I_{y_\mathrm{w}}\sin 2\alpha_m \Bigg(-12.25 I_{21} I_F k\omega + 0.12 I_{21} k U_2 + 9.19 I_{22} I_F \omega + \\
& - 0.09 I_{22} U_2 + I_{31}\cos\alpha_m (0.02 U_2 - 0.65 I_F \omega) \Bigg) - I_{21} I_F I_{y_b} \omega \sin\alpha_m \Bigg)
\end{aligned}$$

$$\begin{aligned}
A_{56} = {} & \frac{1}{I_F^2 I_{y_b}\omega} \rho\sin\alpha_m\cos\alpha_m \Bigg(C_{L_\alpha} I_{y_\mathrm{w}} \cos\alpha_m \Bigg(0.65 I_{21} I_F k\omega - 0.02 I_{21} k U_2 - 0.49 I_{22} I_F \omega + \\
& + 0.01 I_{22} U_2 \Bigg) + C_{L_\alpha} I_{31} \left(5.27 I_F I_{y_b}\omega + 0.15 I_F I_{y_\mathrm{w}}\omega - 0.12 I_{y_b} U_2 - 0.001 I_{y_\mathrm{w}} U_2 \right) + \\
& + C_{L_\alpha} I_{31} I_{y_\mathrm{w}} \cos 2\alpha_m (0.15 I_F \omega - 0.001 U_2) + I_{y_\mathrm{w}} \sin\alpha_m \Bigg(k(-30 I_{11} I_F k\omega + 0.19 I_{11} k U_2 + \\
& + 30 I_{12} I_F \omega - 0.19 I_{12} U_2) + I_{13}(0.04 U_2 - 5.6 I_F \omega) \Bigg) + \\
& + I_{y_\mathrm{w}} (-2 I_{21} I_F k\omega + 0.05 I_{21} k U_2 + 0.5 I_{22} I_F \omega - 0.01 I_{22} U_2) \Bigg)
\end{aligned}$$

$$\begin{aligned}
A_{62} = {} & \frac{1}{I_F^2 I_{y_b}\omega^2} C_{L_\alpha}\rho\sin\alpha_m \Bigg(I_{21} k \left(-826 I_F^2 \omega^2 + 24.7 I_F U_2 \omega - 0.06 U_1^2 - 0.19 U_2^2 \right) + \\
& + I_{22} \left(619.6 I_F^2 \omega^2 - 18.5 I_F U_2 \omega + 0.05 U_1^2 + 0.14 U_2^2 \right) + \\
& + I_{31} \cos\alpha_m \left(1795 I_F^2 \omega^2 - 84.4 I_F U_2 \omega + 0.5 U_1^2 + 1.49 U_2^2 \right) \Bigg)
\end{aligned}$$

$$\begin{aligned}
A_{63} = {} & \frac{1}{I_F^2 I_{y_b} m_\mathrm{v}\omega^2} C_{L_\alpha} m_\mathrm{w} \rho\cos\alpha_m \Bigg(\cos\alpha_m \Bigg(\bar{c}\hat{d} \Bigg(I_{11} k \left(-5.23 I_F U_2 \omega + 0.06 U_1^2 + 0.18 U_2^2 \right) + \\
& + I_{12} \left(3.9 I_F U_2 \omega - 0.05 U_1^2 - 0.14 U_2^2 \right) \Bigg) + \bar{c}\hat{d} I_{21} \cos\alpha_m \left(U_2 (0.02 U_2 - 2.4 I_F \omega) + 0.01 U_1^2 \right) + \\
& + I_{21} r_\mathrm{cg} \left(U_2 (0.18 U_2 - 19.27 I_F \omega) + 0.06 U_1^2 \right) \Bigg) + r_\mathrm{cg} \Bigg(I_{11} k \Bigg(U_2 (1.48 U_2 - 41.88 I_F \omega) + \\
& + 0.49 U_1^2 \Bigg) + I_{12} \left(U_2 (31.4 I_F \omega - 1.1 U_2) - 0.37 U_1^2 \right) \Bigg) \Bigg)
\end{aligned}$$

$$\begin{aligned}A_{64} = {} & \frac{1}{I_F I_{y_b} \omega} C_{L_\alpha} \rho \cos\alpha_m \Bigg(42.2 I_{11} I_F k\omega - I_{11} k U_2 - 31.7 I_{12} I_F \omega + \\ & + 0.74 I_{12} U_2 + I_{21} \cos\alpha_m (19.4 I_F \omega - 0.12 U_2) \Bigg)\end{aligned}$$

$$\begin{aligned}A_{65} = {} & \frac{1}{I_F I_{y_b} \omega} C_{L_\alpha} \rho \sin\alpha_m \Bigg(198 I_{21} I_F k\omega - 2 I_{21} k U_2 - 148 I_{22} I_F \omega + 1.5 I_{22} U_2 + \\ & + I_{31} \cos\alpha_m (10.5 I_F \omega - 0.25 U_2) \Bigg)\end{aligned}$$

$$\begin{aligned}A_{66} = {} & \frac{\rho}{I_F I_{y_b} \omega} \Bigg(C_{L_\alpha} \cos\alpha_m \left(-5.23 I_{21} I_F k\omega + 0.12 I_{21} k U_2 + 3.9 I_{22} I_F \omega - 0.09 I_{22} U_2 \right) + \\ & + C_{L_\alpha} I_{31} \cos 2\alpha_m (0.01 U_2 - 1.2 I_F \omega) - 1.2 C_{L_\alpha} I_{31} I_F \omega + 0.01 C_{L_\alpha} I_{31} U_2 + \\ & + \sin\alpha_m \Bigg(k (242 I_{11} I_F k\omega - 1.5 I_{11} k U_2 - 242 I_{12} I_F \omega + 1.5 I_{12} U_2) + \\ & + I_{13} (45.5 I_F \omega - 0.29 U_2) \Bigg) + \\ & + 16.43 I_{21} I_F k\omega - 0.39 I_{21} k U_2 - 4.1 I_{22} I_F \omega + 0.1 I_{22} U_2 \Bigg).\end{aligned}$$

Appendix E

Optimized Shooting Method

Periodic shooting methods have been used in the literature of FWMAVs/insects to capture the periodic orbits associated with different equilibrium configurations (e.g., hovering) [121, 41, 42]. The stability of these orbits are then analyzed using the Floquet theorem [149]. Dednam and Botha [148] provided an optimized shooting approach to capture a periodic solution of a nonlinear system. This optimized shooting approach adopts the Levenberg-Marquardt optimization algorithm to minimize the residual. This algorithm is based on two methods: the gradient descent method and the Gauss-Newton method. According to Gavin [154], when the parameters are far from the optimal values, the Levenberg-Marquardt algorithm operates in a way similar to gradient-descent. However, it operates similar to the Gauss-Newton method when approaching the optimal point.

Consider the following system of equations

$$\dot{\boldsymbol{x}}(t) = \boldsymbol{f}(\boldsymbol{x}(t), \boldsymbol{\alpha}, t), \tag{E.1}$$

where $\boldsymbol{x} \in \mathbb{R}^n$ and $\boldsymbol{f} \colon \mathbb{R}^n \times \mathbb{R}^k \times \mathbb{R}_{\geq 0} \to \mathbb{R}^n$, and $\boldsymbol{\alpha}$ are the system parameters. This system corresponds to a non-autonomous vector field. Thus, a solution $\boldsymbol{x}(t)$ to the system (E.1) is periodic if there exists a constant $T > 0$ such that

$$\boldsymbol{x}(t) = \boldsymbol{x}(t + T). \tag{E.2}$$

The optimized shooting method can be applied to any system that can be expressed in the form of (E.1), and, for convenience, a dimensionless time τ is introduced such that $t = \tau\, T$. Equation (E.1) is then written as

$$\frac{d\boldsymbol{x}}{d\tau} = T\boldsymbol{f}(\boldsymbol{x}(\tau T), \boldsymbol{\alpha}, \tau T). \tag{E.3}$$

Thus, this new variable τ allows the simplification of the boundary conditions in Eq. (E.2) so that $x(\tau = 0) = x(\tau = 1)$ and Eq. (E.3) can be integrated over one period (i.e., letting τ run from zero to one). Now, the residual can be written as

$$\mathbf{R} = T \int_0^1 \boldsymbol{f}(\boldsymbol{x}(\tau T), \boldsymbol{\alpha}, \tau T)\ d\tau. \tag{E.4}$$

According to Dednam and Botha [148], the residual depends on the number of quantities to be optimized and can be expressed as

$$\mathbf{R} = \Big(\boldsymbol{x}(1) - \boldsymbol{x}(0),\ \boldsymbol{x}(1 + \mathit{\Delta}\tau) - \boldsymbol{x}(\mathit{\Delta}\tau), \ldots,\ \boldsymbol{x}(1 + (p-1)\mathit{\Delta}\tau) - \boldsymbol{x}((p-1)\mathit{\Delta}\tau)\Big), \tag{E.5}$$

where $\mathit{\Delta}\tau$ is the integration step size and $p \in \mathbb{N}$. For solvability, the natural number p is chosen so that the number pn of components of the residual is greater than or equal to the number of unknowns (initial point on the periodic orbit and any unknown parameters such as the period in autonomous systems).

Appendix F

Hawkmoth Morphological Parameters

The morphological parameters and the wing planform for the hawkmoth, as given in [145] and [155], are

$$
\begin{aligned}
&R = 51.9\text{mm},\ \mathrm{S} = 947.8\text{mm}^2,\ \bar{\mathrm{c}} = 18.3\text{mm},\\
&\hat{r}_1 = 0.44,\ \hat{r}_2 = 0.525,\ f = 26.3\text{Hz},\ \Phi = 60.5°,\\
&\alpha_m = 30°,\ m_b = 1.648\text{gm},\ \text{and } \mathrm{I_{yb}} = 2080\text{mg.cm}^2,
\end{aligned}
$$

where R is the semi-span of the wing, S is the area of one wing, $\bar{c}$ is the mean chord, f is the flapping frequency, Φ is the flapping angle amplitude, m_b is the mass of the body, and I_{yb} is the body moment of inertia around the body y-axis. The moments of the wing chord distribution $\hat{r}_1$ and $\hat{r}_2$ are defined as

$$I_{k1} = 2\int_0^R r^k c(r)\, dr = 2SR^k \hat{r}_k^k.$$

As for the wing planform, the method of moments used by Ellington [155] is adopted here to obtain a chord distribution for the insect that matches the documented first two moments

$\hat{r}_1$ and $\hat{r}_2$; that is,

$$c(r) = \frac{\overline{c}}{\beta}\left(\frac{r}{R}\right)^{\lambda-1}\left(1-\frac{r}{R}\right)^{\gamma-1},$$

where

$$\lambda = \hat{r}_1\left[\tfrac{\hat{r}_1(1-\hat{r}_1)}{\hat{r}_2^2-\hat{r}_1^2}-1\right]\ ,\ \gamma = (1-\hat{r}_1)\left[\tfrac{\hat{r}_1(1-\hat{r}_1)}{\hat{r}_2^2-\hat{r}_1^2}-1\right],$$
$$\text{and}\ \ \beta = \textstyle\int_0^1 \hat{r}^{\lambda-1}(1-\hat{r})^{\gamma-1}\,d\hat{r}.$$

The mass of one wing is taken as 5.7% of the body mass according to Wu et al. [108] and is assumed uniform with an areal mass distribution m' The inertial properties of the wing are then estimated as

$$I_x = 2\textstyle\int_0^R m' r^2 c(r)\,dr\ ,\ I_y = 2\textstyle\int_0^R m'\hat{d}^2 c^3(r)\,dr$$
$$,I_z = I_x + I_y,\ \text{and}\ r_{\text{cg}} = \tfrac{2\int_0^R m' r c(r)\,dr}{m_{\text{w}}} = \tfrac{I_{11}}{2S},$$

where $\hat{d}$ is the chord-normalized distance from the wing hinge line to the center of gravity line.